$B^{\circ}(1235)$ PRODUCTION IN THE REACTION

$\pi^{-}p \rightarrow \omega\pi^{\circ}n$ AT 8.45 GEV/C

by

© Paul J. Brockman

A thesis submitted to the Faculty of Graduate Studies and Research in partial fulfillment of the requirements for the degree of Doctor of Philosophy (Physics).

Department of Physics
McGill University
Montréal, Québec
Canada

March 1981

ABSTRACT

We have performed a sequential decay analysis of the reaction

$$\pi^- p \rightarrow \omega\pi^o n$$

at 8.45 GeV/c in a counter - spark chamber experiment conducted at the Argonne National Laboratory Zero Gradient Synchrotron. The production and decay properties of the B^o meson are presented , along with the differential cross section for the reaction $\pi^- p \rightarrow B^o n$. We present evidence for the existence of the $\rho'(1250)$ meson ($IJ^{PC} = 11^{--}$). Our study of the B^o production indicates dominance of A_2 exchange (nucleon spin flip) . We have found significant amounts of D-wave in the $B^o \rightarrow \omega\pi^o$ decay. The production mechanisms for $\rho'(1250)$ are similar to those for $\rho(770)$ production and are dominated by π exchange.

RESUME

Nous avons accomplis une analyze de désintégration en séquence pour la réaction

$$\pi^- p \to \omega\pi^o n$$

à une impulsion incidente de 8.45 GeV/c dans une expérience exécutée au synchrotron du Argonne National Laboratory. Les propriétés de production et de désintégration du méson B^o sont présentées ainsi que la section efficace différentielle pour la réaction $\pi^- p \to B^o n$. Nous présentons de l'évidence sur la présence du méson $\rho'(1250)$ ($IJ^{PC} = 11^{--}$). Notre étude sur la production du B^o indique que l'échange de A_2 domine (changement d'orientation du spin de nucleon) . Nous avons trouvé de quantité significatif d'onde L = 2 dans la désintégration $B^o \to \omega\pi^o$. Les mécanismes de production pour le méson $\rho'(1250)$ sont semblable à ceux du $\rho(770)$ et ils sont dominés par l'échange de méson π.

ACKNOWLEDGEMENTS

I wish to express my thanks to my advisor, Dr. P. Patel, and to Dr. N.R. Stanton for the advice and assistance they provided on this experiment.

Special thanks go to Dr. J. A. Dankowych for his help and advice in both the analysis and data-taking stages of the experiment.

I particularly want to thank J. W. Heimaster for his assistance in the development of the analysis programs and for his help in the use of many of his software packages. My thanks also to J. M. Ludwig and Dr. J.F. Martin for sharing their expertise.

I would also like to thank other members of our collaboration who all contributed to the success of this experiment: Dr. H. Areti, Dr. A. J. Pawlicki, Dr. J. D. Prentice, Dr. T.S. Yoon, Dr. K.W. Edwards, D. Legacy, Dr. J. Gandsman, and E. Shabazian. In addition, I am grateful to the members of our earlier experiment who helped in constructing the Charged and Neutral Spectrometer: Dr. M. Shaevitz, C. Zanfino, Dr. R. Sidwell, Dr. N. W. Reay, Dr. K. Reibel, Dr. G. Luste, Dr. M. Abolins and Dr. G. Luxton.

I want to express my appreciation to the Argonne National Laboratory ZGS operations crew and H. Coombes, J. Fitch, A. Kiang and C. Rush for their technical support.

Finally, I thank P. Babecki for the outstanding job done on the computer formatting and typing of this thesis.

continued...

ACKNOWLEDGEMENTS (continued)

This research was supported in part by the United States Department of Energy and by the Natural Sciences and Engineering Research Council of Canada, through the Institute of Particle Physics. Financial assistance, in the form of two McConnell Fellowships and the Alexander McFee Scholarship, is very gratefully acknowledged.

TABLE OF CONTENTS

continued...

TABLE OF CONTENTS (continued)

continued...

TABLE OF CONTENTS (continued)

INTRODUCTION

The purpose of this experiment was to search for the neutral B(1235) and $\rho'(1250)$ mesons via the $\omega\pi^o$ system in the reaction

$$\pi^- p \rightarrow (\text{meson})n$$
$$\quad\quad \vert\!\rightarrow \omega\pi^o$$
$$\quad\quad\quad \pi^o \rightarrow \gamma\gamma$$
$$\quad\quad\quad \omega \rightarrow \pi^+\pi^-\pi^o$$
$$\quad\quad\quad\quad \pi^o \rightarrow \gamma\gamma \;.$$

We study the production and decay mechanisms of these mesons.

The data for this study were taken at the Argonne National Laboratory Zero Gradient Synchrotron in a high statistics (> 26 x 10^6 triggers) counter-spark chamber experiment (E420 - E428) [1], using incident pions of momentum 8.45 GeV/c.

Although it has become evident in recent years that a very successful classification of baryon states can be made by considering them to be 3 quark states, attempts to extend such analyses to the mesons, which are taken to be $q\bar{q}$ states, have not been as successful-partly because the number of observed resonances does not nearly account for the predicted states.

In the following figure we show a tabulation of all possible low-lying $q\bar{q}$ states. We adopt the conventional spectroscopic notation $N\,^{2S+1}L_J$, where N is the radial quantum number, $\vec{L}$ is the $q\bar{q}$ relative orbital angular momentum,

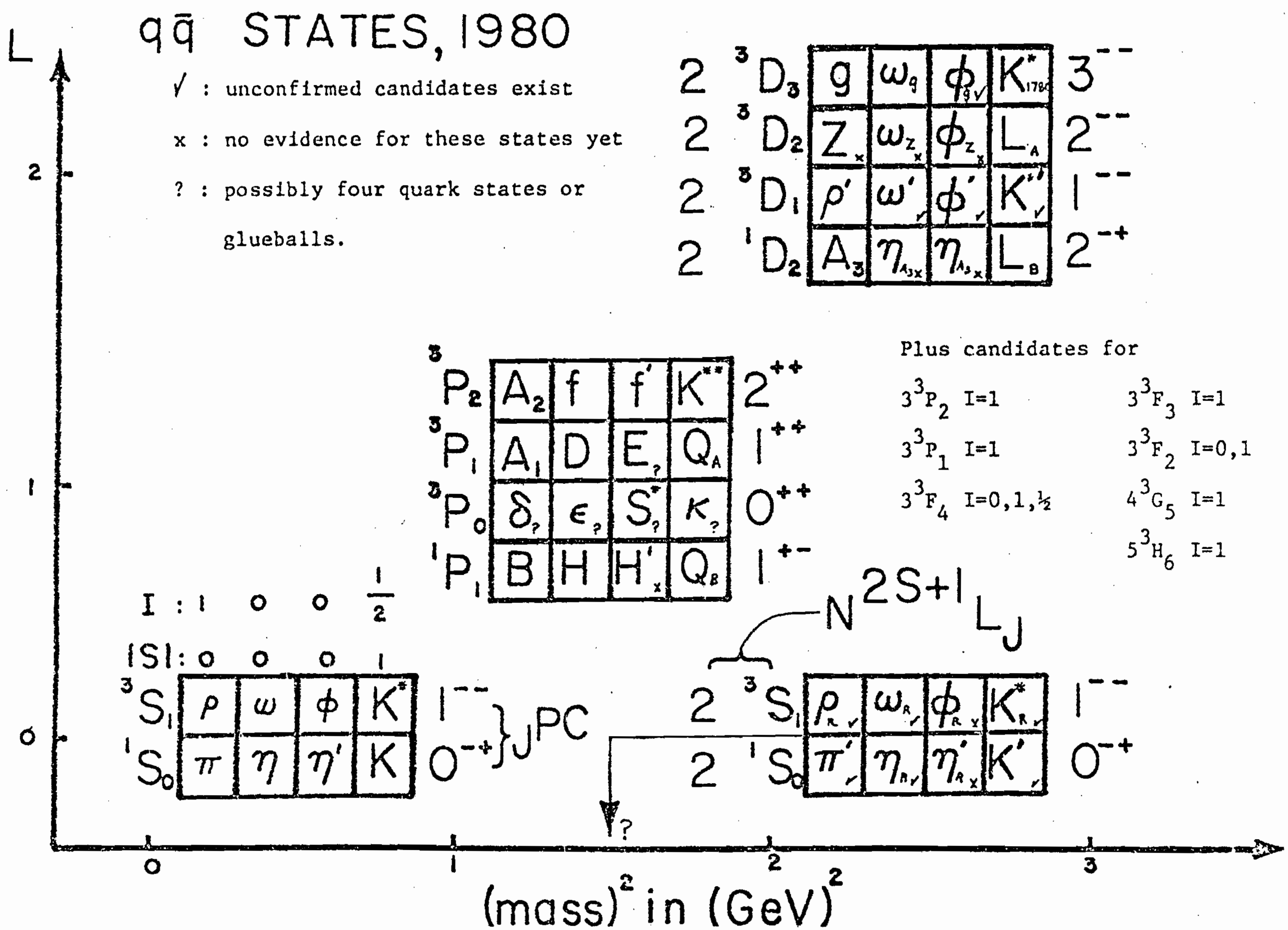

Well-established meson ($q\bar{q}$) states (1980). Notation is discussed in text.

$\vec{S} = \vec{S}_q + \vec{S}_{\bar{q}}$ is the total spin and $\vec{J} = \vec{L} + \vec{S}$ is the total angular momentum of the $q\bar{q}$ state.

Mesons marked with a check (√) mark such as the ρ_R are considered to be unconfirmed candidates for those states. Some states, marked with a question mark, although well established as resonances, may in fact be 4 quark states or possibly belong to multiplets other than those indicated. Many states need to be confirmed and many more have no observed candidates whatsoever.

The theoretical motivation for studying the $\omega\pi^o$ system lies in the fact that, in the quark model of mesons, only two resonances are expected in this region; the B^o ($L_{q\bar{q}} = 1$) $IJ^{PC} = 11^{+-}$ and the $\rho'(1250)$ (the first radial excitation of the $\rho(770)$, $L_{q\bar{q}} = 0$) $IJ^{PC} = 11^{--}$. The charged B has been observed and studied by several experiments [5,26,27], but the neutrally charged B has never been observed. The $\rho'(1250)$ has yet to receive a one star rating as a resonance by meson spectroscopists. It has never been studied in π^-p interactions. The observation of these resonances (B^o and $\rho'(1250)$) would be an important confirmation of the quark model.

The B meson may decay to the $\omega\pi$ system via S($l = 0$) or D($l = 2$) waves. The world average of the ratio $(D/S)^2$ measured for the charge B is .06 ± .03 [38]. In studies of the charged B, little consideration has been given to the problem of possible $J^P = 1^+$ Deck [46] background because the observed $B^{\pm}$ is relatively narrow and, therefore, presumably not seriously affected by such background effects. If such effects were present, they could alter the measured $(D/S)^2$ ratio from that expected for a two-quark B meson. We point out that the Deck-like backgrounds are expected to be significantly reduced in charge exchange processes because no Pomeron coupling is allowed by the baryon vertex. A measurement of the $(D/S)^2$ ratio for the B^o consistent with the ratio for $B^{\pm}$ would then suggest that the Deck-like processes are strongly suppressed in both the charged and neutral B experiments, and the B is a clear candidate for the expected $L_{q\bar{q}} = 1$, $IJ^{PC} = 11^{+-}$ quark model state.

Note that $\pi^- p \to (\omega\pi)^o n$ is a very favourable reaction with which to search for the $\rho'(1250)$. As is the case for $\pi^- p \to \rho n$, the ρ' is expected to be produced mainly through π - exchange. Compared with $\pi^- p \to (\omega\pi)^- p$, π - exchange production of the $\rho'(1250)$ in the process $\pi^- p \to (\omega\pi)^o n$ is increased by a factor of two and B production is reduced by a factor of two ($B^{\pm}$ can be produced by ω and A_2 exchange, whereas B^o can only be produced by A_2 exchange).

It should also be noted that, due to phase space considerations, the $\omega\pi^o$ decay mode of the $\rho'(1250)$ is heavily favoured. This can be seen in e^+e^- annihilation data [42], where mass plots of the decay products $\pi^+\pi^-\pi^+\pi^-$ show no evidence for a $\rho'(1250)$ resonance, whereas plots of $\pi^+\pi^-\pi^o\pi^o$ show a clear signal in the 1.2 - 1.3 GeV region.

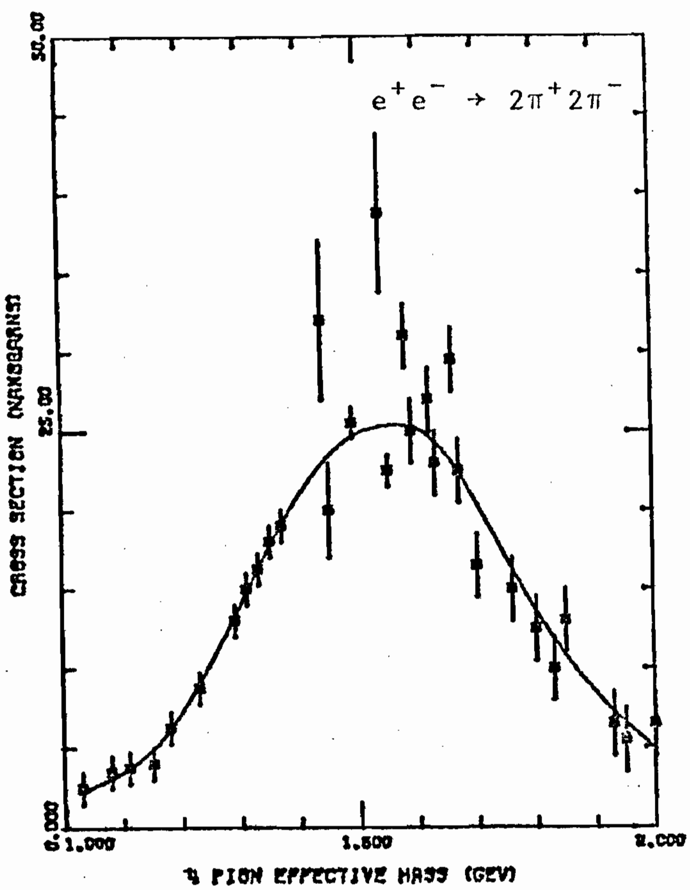

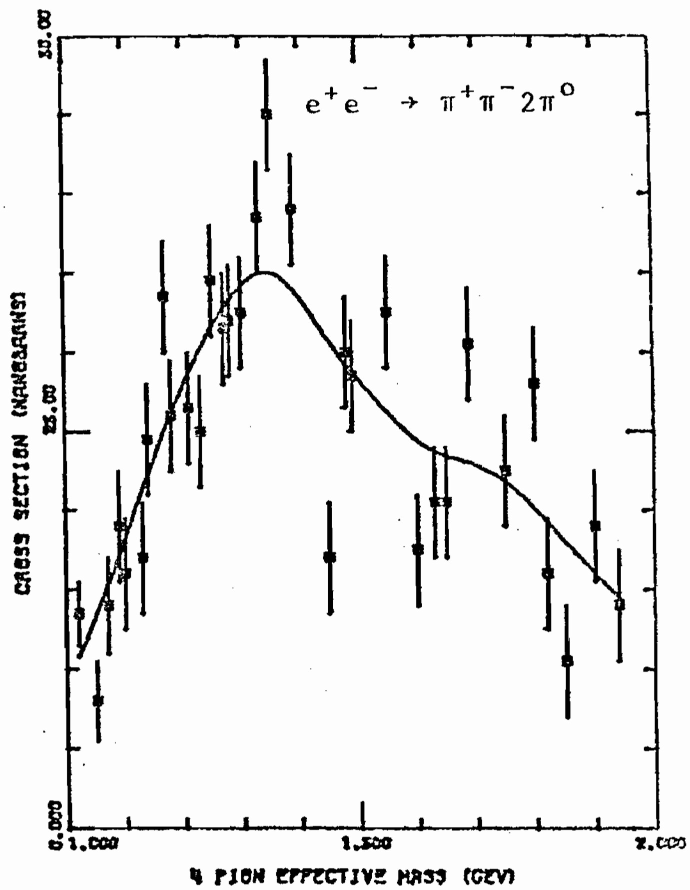

A description of the experiment will be given in Chapter 1. We discuss the details of the data collection and analysis in Chapters 2 and 3. Chapters 4 and 5 present our experimental resolution and the acceptance of our apparatus, respectively. The process to determine the final $\omega\pi^o$ sample is discussed in Chapter 6, inefficiency corrections are calculated in Chapter 7 and the differential cross section for the reaction $\pi^- p \rightarrow B^o n$ is given in Chapter 8. The theory and techniques used to determine the production and decay parameters of the B^o and $\rho'(1250)$ mesons are explained in Chapter 9. Finally, in Chapter 10, we present and discuss our results and conclusions.

CHAPTER 1

APPARATUS

The sample of events from the process

$$\begin{array}{l} \pi^- p \to \pi^+ \pi^- \pi^0 \pi^0 n \\ \qquad\qquad\qquad\quad\;\; \to \gamma\gamma \\ \qquad\qquad\qquad\;\; \to \gamma\gamma \end{array}$$

(hereafter referred to as 4γ events) was obtained simultaneously with the collection of data for study of the reactions

$$\begin{array}{l} \pi^- p \to \pi^+ \pi^- \pi^0 n \\ \qquad\qquad\qquad\;\; \to \gamma\gamma \end{array}$$

and

$$\begin{array}{l} \pi^- p \to \pi^+ \pi^- \eta n \\ \qquad\qquad\qquad\;\; \to \gamma\gamma \quad . \end{array}$$

In addition we had the 3 charged pion events

$$\begin{array}{l} \pi^- p \to \pi^+ \pi^- \pi^0 \pi^- p \\ \qquad\qquad\qquad\;\; \to \gamma\gamma \quad . \end{array}$$

An incident π^- beam of momentum 8.45 GeV/c was used at the

ZGS in January, March and June, 1977.

A subset of the 4γ events above is the process:

$$\begin{array}{llll}
\pi^- p \to B^o n & & & \\
\quad\ \ \lfloor\!\to \omega\pi^o & & & \\
\qquad\quad \lfloor\!\to \gamma\gamma & & & \\
\qquad \lfloor\!\to \pi^+\pi^-\pi^o & & & \\
\qquad\qquad\quad \lfloor\!\to \gamma\gamma\ . & & &
\end{array} \tag{1-1}$$

All the final B^o decay products were detected and measured: the charged particles, using a conventional dipole magnet forward spectrometer (ten spark chambers); and the gamma rays, by means of an array of 56 lead glass blocks preceded by three spark chambers. The neutron was not detected. The experimental layout is shown in Figure 1 and discussed in the following sections.

1.A. Beam

The pion beam (see Figure 2) was produced by directing the 12 GeV/c extracted proton beam on a beryllium target. Negative particles produced at 1.5 degrees were focused by a two-stage beam transport system onto horizontal and vertical beam veto scintillation counters, BV1 and BV2, situated 120 inches downstream of the liquid hydrogen target.

The first stage produced a momentum dispersed focus at

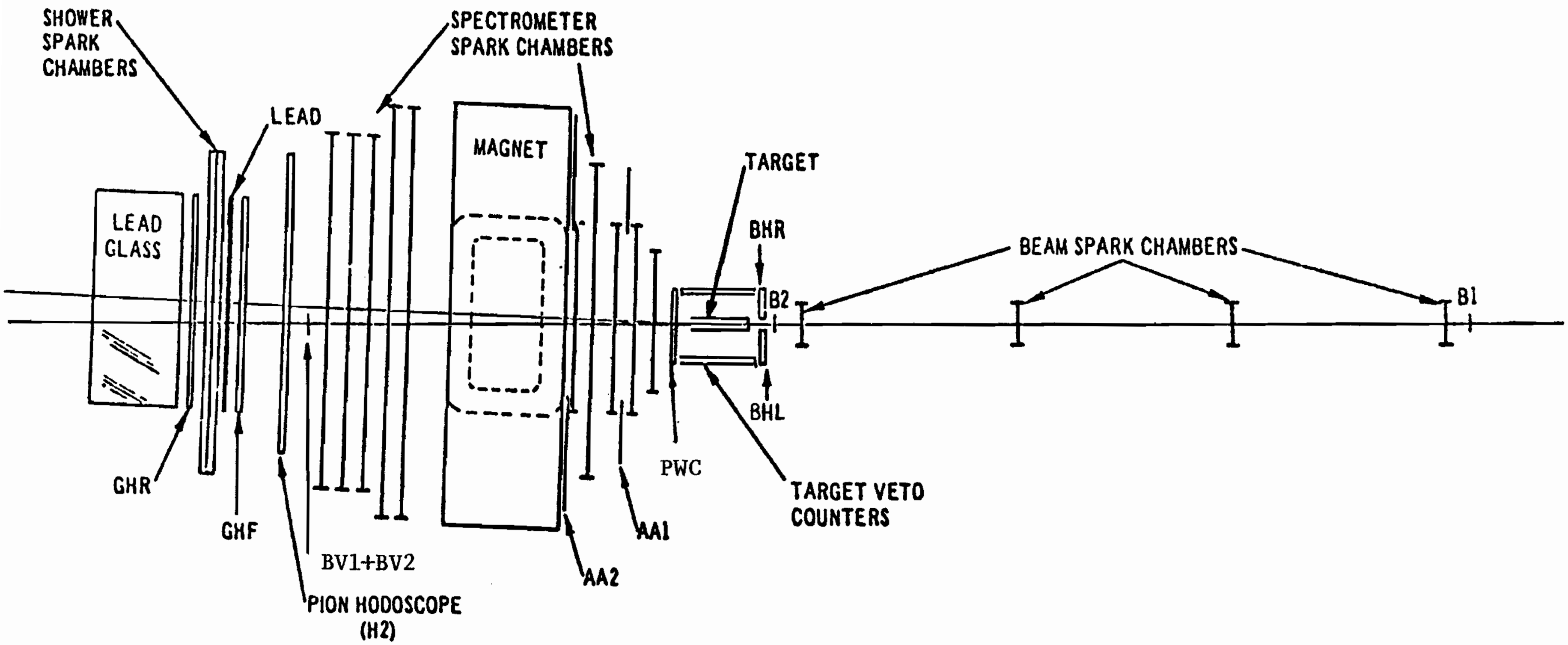

FIGURE 1 Experimental Layout

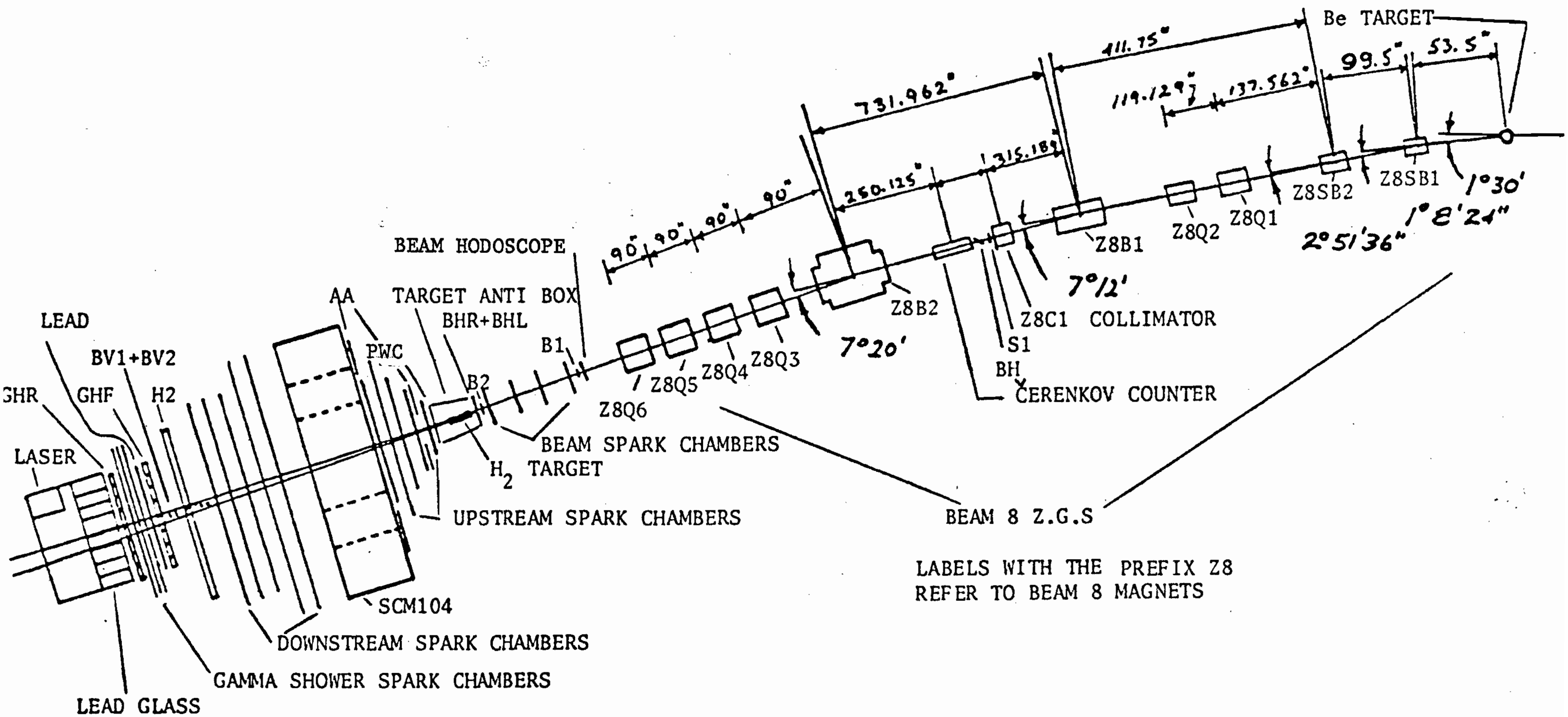

FIGURE 2 Beam Layout

the position of the beam counter hodoscope BH - a set of seven finger counters, each subtending a momentum bite of .5% FWB. The second stage recombined the momenta, focusing the beam onto the BV1 and BV2 counters, where all non-interacting beam events were rejected. Beam particles outside the one-inch radius hydrogen target were removed by the hole anti-counter BHR + BHL. We averaged 60,000 beam particles per pulse, of which 85% passed within the hole.

The beam particle direction was determined by means of four magnetostrictive readout spark chambers, spaced 36 inches apart upstream of the hydrogen target. Late beam particles were removed by means of a 10-finger hodoscope (BH10) located immediately in front of beam chamber 1 and rotated 45 degrees to the normal. The slope and intercept of each trajectory were measured to within ±.1 mrad and ±.015 inches (FWHM), respectively. A summary of the beam characteristics is given in Table 1.

1.B. Charged Particle Spectrometer

The momenta of the charged particles were measured by means of a spectrometer located immediately downstream of the hydrogen target. It consisted of a set of five magnetostrictive readout spark chambers on either side of a wide aperture magnet (SCM104), with a gap 40 inches high by 60 inches wide by 32 inches deep. The magnet current was set

TABLE 1

E-397 BEAM CHARACTERISTICS

Momentum -	8.45 GeV/c
Beam Spill -	600 msec (FWHM)
Final Focus Spot Size -	½" × ½"
Flux -	6×10^4 pions per pulse
Production Angle -	1.5°
Momentum Bite -	2½ %
$\Delta P/P$ -	.005
Beam Spark Chamber -	Spacing = 36" Position resolution Δx = .02" FWHM
Beam Direction Measurement -	$\Delta\theta = .0002$ $\Delta x_{intercept}$ = .030"
Focus -	120" downstream of hydrogen target
Hydrogen Target -	2" diameter × 16" length

to produce a central field of 5.9 kilogauss, with an integrated field of 240 kg-in. The thinness of the magnet, combined with the close positioning of the chambers to it, permitted a good acceptance for wide angle tracks.

Details of the charged particle detection equipment and spark chamber dimensions are listed in Table 2. A 5 KV pulse was applied to the chambers for each trigger. This was done using thyratron-capacitor bank units. A potential of 75 VDC was maintained on all chambers to help clear away the ionized debris from stray charged tracks. In addition to this, a 1 KV, 600 nsec pulse was applied after each trigger to remove residual ionization from the sparks.

The gas in the chambers was a mixture of 90% neon and 10% helium. Ethyl alcohol was added to the gas to quench the sparks. The entire gas system was recirculated and purified through a liquid nitrogen cooling system [2] .

To eliminate the ambiguities which arise when multiple sparks occur, two chambers upstream and two chambers downstream were rotated by 45 degrees and 15 degrees respectively. Spark positions in the chambers were obtained by magnetostrictive wire readouts, using a Science Accessories Corporation (SAC) scaler system interfaced to CAMAC. Each plane was instrumented to handle up to six sparks.

TABLE 2

SPECTROMETER CHARACTERISTICS

Spark Chambers -

		Rotation	Active Area	Distance from Target
Upstream	1	0°	24" × 16"	19.00"
	2	45°	28" × 18"	24.50"
	3	0°	40" × 30"	29.75"
	4	45°	42" × 36"	35.00"
	5	0°	40" × 40"	40.50"
Downstream	1	15°	5' × 7'	91.50"
	2	15°	5' × 7'	97.50"
	3	0°	5' × 7'	103.50"
	4	0°	5' × 7'	109.50"
	5	0°	5' × 7'	115.50"

Magnet -

Type	picture frame	SCM-104
Nominal $\int B \cdot dl$	240 kg-inches	
Central Field	5.9 kgauss	
Size	84" W × 40" H × 40" D	
Center	63" from LH_2 target	

continued...

TABLE 2

SPECTROMETER CHARACTERISTICS (continued)

Chamber High Voltage -	
Method	capacitor bank discharge
Capacitance	10 nfarads / 5' × 7' area
Pulse Height	6.8 KV
Risetime	150 nsec
Delay	550 nsec
Clearing Field	75 V DC
Pulsed Field	1 KV - 600 nsec
Readout -	
Method	magnetostrictive
System	SAC Midas, 6 scalers/plane
Resolution -	
Position	.05" (FWHM)
Momentum	4% (FWHM) at 2 GeV/c

1.C. Photon Detector

The gamma rays were detected, and their energies determined, using a system of lead glass Čerenkov counters and magnetostrictive readout spark chambers.

The part of the detector which measured the position of the shower origin consisted of alternate layers of converter and spark chamber; first, .5" (2.07 radiation lengths) of lead plus .1 radiation lengths of aluminium, followed by a spark chamber and then by another .25" (1.14 radiation lengths) of lead plus .07 radiation lengths of aluminium (this assembly implied a total conversion probability of 89%). This was followed by two more spark chambers. Two of the three chambers were rotated 12.5 degrees to resolve multi-track ambiguities. The whole arrangement was tightly packed, with gaps of .25" between converter and the next chamber. Thus, the tightly collimated showers (rms angle per stage is approximately .2 degrees for one GeV photons [3]) resulted in a single large spark in the following chamber. This spark was then taken as the shower conversion center. The position resolution was measured by following charged particles through the spectrometer down to the gamma spark chambers, with the result Δx = .35" (FWHM) holding for all energies from 400 MeV to 2.0 GeV. The second and third spark chambers supplied information for showers which were missed by the first spark chamber, and were also used to confirm and resolve shower positions. To ensure high efficiency for multi-spark events, each plane was instrumented to handle up to 12-16 sparks. For these chambers, the spark digitization was performed by Borer scalers interfaced to our CAMAC system.

The energies were measured using a 56-element lead glass array placed immediately downstream of the gamma chambers. The lead glass blocks were arranged in a symmetric array with a small beam hole (Figure 3). Each block measured 7.5 inches by 7.5 inches by 12 inches (10 radiation lengths) and was viewed by a 5-inch photomultiplier attached to the downstream face. The signal from each tube was digitized by an Analog to Digital Converter (ADC) and the information made available to the online computer via CAMAC. The ADC reading, corrected for small geometrical losses, was then proportional to the energy deposited in the block. The measured energy resolution for a 1 GeV gamma shower was 25% FWHM.

1.D. Anti-counter System

Events accompanied by charged particles or gamma rays that would go undetected by the apparatus were removed by an anti-counter system.

To reject gamma rays and charged particles recoiling at wide angles, the four lateral sides of the hydrogen target were covered by four alternate layers of .125-inch

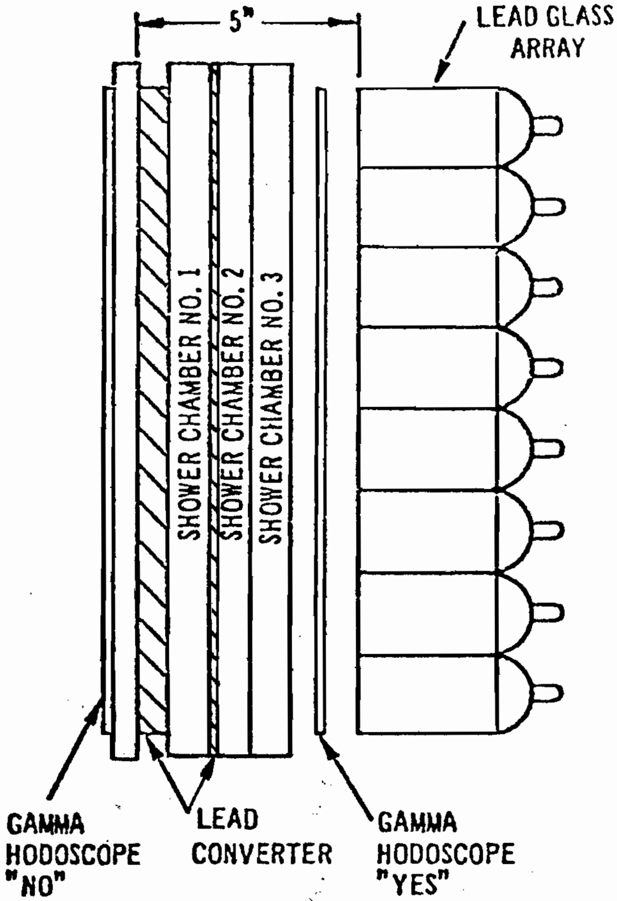

SHOWER SPARK CHAMBERS

ROTATED	ACTIVE AREA	DISTANCE FROM CONVERTER
NO. 1 - NO	5' x 5'	0.5"
NO. 2 - 12.5°	5' x 5'	1.5"
NO. 3 - 12.5°	5' x 5'	2.5"

LEAD CONVERTER

3.38 R.L. x 60" x 60"

POSITION:

140" DOWNSTREAM OF HYDROGEN TARGET

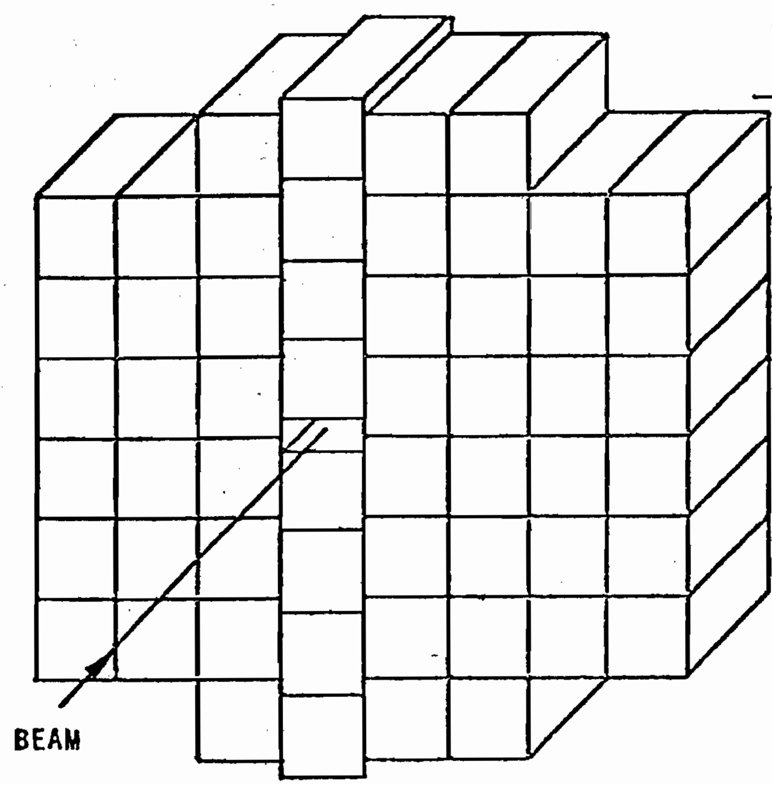

LEAD GLASS ČERENKOV COUNTER ARRAY

SIZE: 7-1/2" x 7-1/2" x 12"

TYPE OF GLASS BOURNS OPTICAL
PEM 62

PHOTOTUBE (5" D)
EMI

GLUED DIRECTLY TO BLOCK

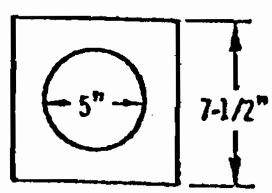

FIGURE 3 Lead Glass Gamma Detector

scintillator and .25-inch lead sheets. This target anti-counter (TA) setup is shown in detail in Figure 4. Events were rejected if one or more counters detected a particle. All target anti-counters were latched and recorded with each event to allow the offline investigation of the above TA veto constraint; in particular, to correct for the loss resulting from good events being vetoed by recoil neutrons.

In the forward direction, the two sets of counters, AA1 and AA2 (Figure 1), limited the allowed solid angle to that covered by the spark chambers and the gamma ray detector. Each set of counters was made sensitive to gamma rays by covering its upstream side with .25-inch lead sheets. Events were rejected if one of these counters detected a particle.

1.E. Fast Logic and Trigger System

A system of scintillation counters was set up to detect, and isolate from unwanted background, all events consisting of two or three charged pions, two or more gamma rays, and a slow recoil neutron. This triggering system consisted also of a Proportional Wire Chamber (PWC) whose wires were clustered into strips so that, in effect, it served as a 16-element hodoscope. Table 3 lists all counters. Signals from all counters concerned were combined

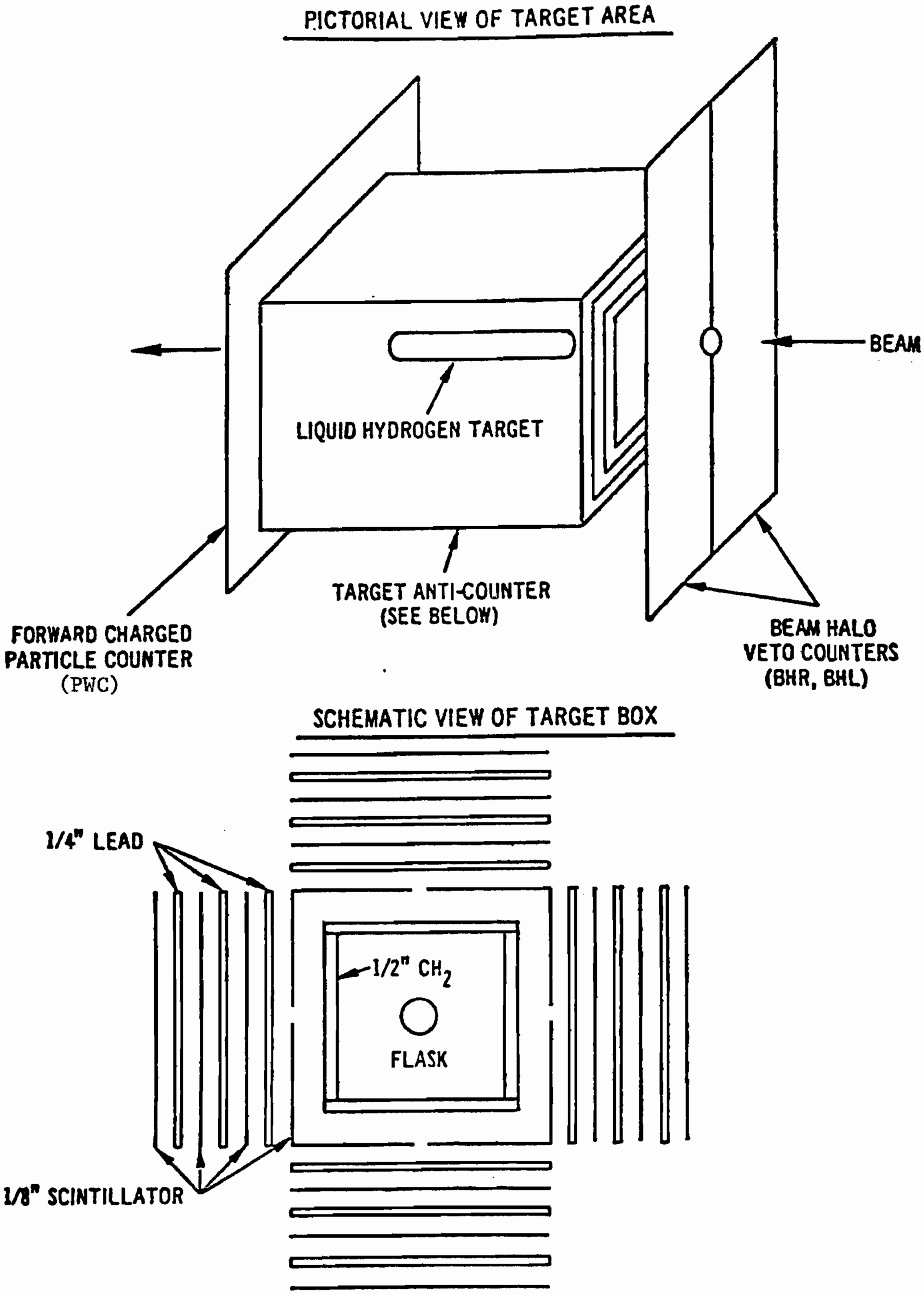

FIGURE 4 Target Anti-counter System

TABLE 3

SCINTILLATION COUNTERS

Name	Size	Position (Z downstream, Z=0 at LH_2 target)	Purpose
S1	1/16" × 2" × 1½"	-	
B1	1/8" × 3" × 3"	-170.0"	Detect beam
B2	1/16" × 2" × 2"	- 36.0"	
BHR BHL	¼" × 16" × 24", with 1" hole	- 25.0"	Anti beam halo
PWC	18" × 13.5" active area	+ 14.0"	Charged particle hodoscope
AA1	opening 26" × 16"	+ 23.0"	Anti particles outside fiducial volume
AA2	opening 40" × 40"	+ 42.0"	
H2	30 counters, each 1/8" × 4" × 42"	+122.8"	Charged particle hodoscope
BV1	¼" × 4" × 4"	+124.0"	Veto non-interacting beam
BV2		+129.0"	
GHF	16 counters, each ¼" × 7½" × 30"	+140.0"	No gamma hodoscope
GHR		+143.5"	Yes gamma hodoscope
Target anti-counters	4 alternate layers of 1/8" scintillator and ¼" lead sheets placed each side of target		Veto particles at wide angles from the target

in fast electronic logic modules to produce a trigger. The trigger was then used to initiate the firing of the spark chambers, the gating of the gamma shower ADC's, and the storing of the resulting CAMAC information.

The fast logic initiated an event trigger when a true condition resulted for the expression

$$\mathrm{BEAM} \cdot \mathrm{PWC} \cdot \mathrm{CHARGED} \cdot \mathrm{GAMMA} \cdot \mathrm{ANTI},$$

where each term is described below. A simplified trigger diagram is shown in Figure 5.

1) $\mathrm{BEAM} = \mathrm{S1} \cdot \mathrm{B1} \cdot \mathrm{B2} \cdot \overline{(\mathrm{BHR} + \mathrm{BHL})} \cdot \overline{(\mathrm{BV1} + \mathrm{BV2})}$

A beam particle, indicated by a count in each of the counters S1, B1 and B2 and none in the halo-counters BHR, BHL, must have interacted in the target because no counts occurred in the beam veto counters, BV1 and BV2.

2) PWC

The PWC, located immediately downstream of the target, demanded that only 2 or 3 charged particles be detected. In this way, it supplemented the H2 hodoscope and avoided false triggers caused by back-scatters from the lead converter. The PWC was hardwired into 16 independent strips, whose respective widths were chosen by Monte Carlo simulation to maximize the trigger rate. The PWC is described in detail in

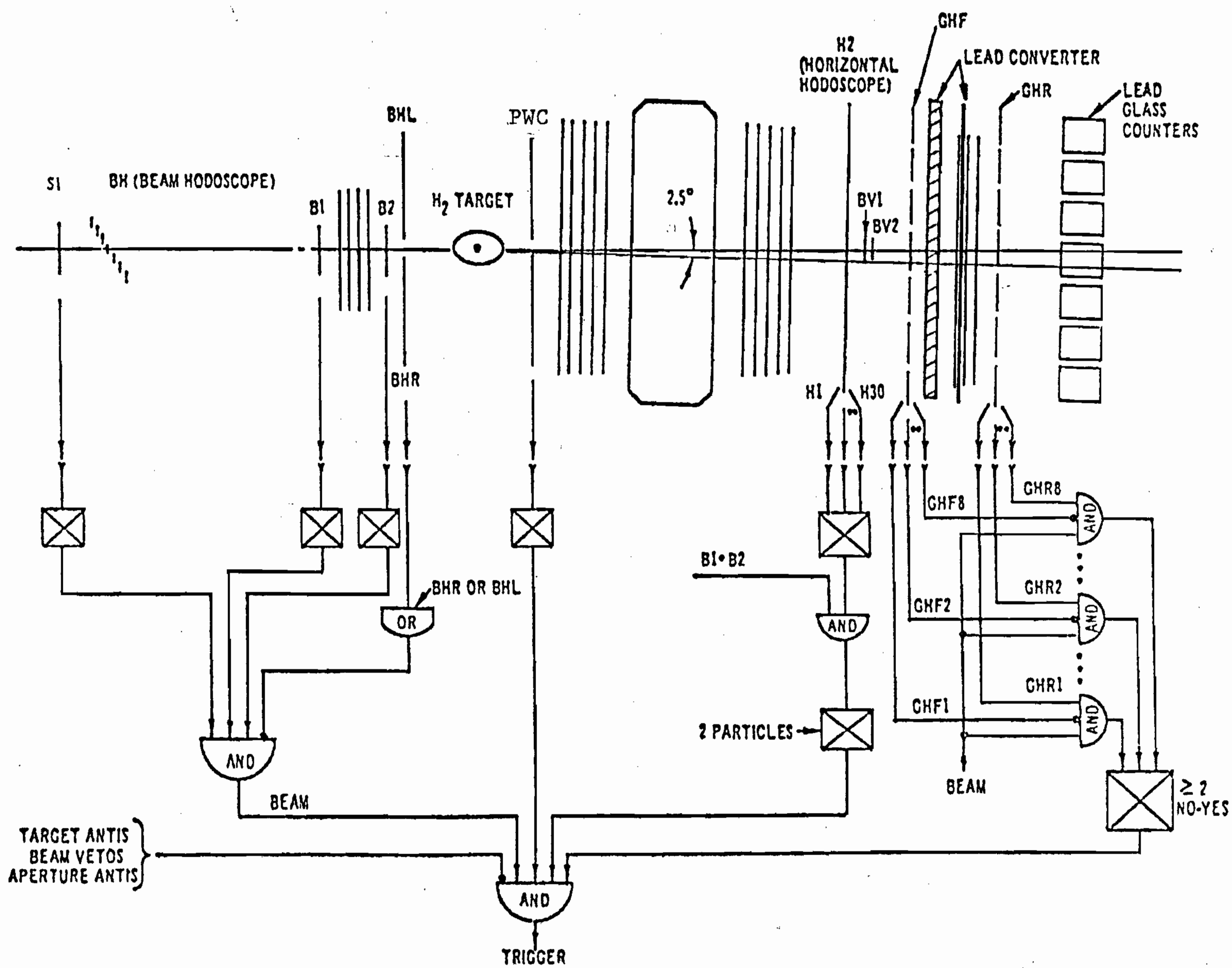

FIGURE 5 Trigger Schematic

Figure 6.

3) CHARGED = H2

We also demanded that only two or three elements of the 30-element scintillator hodoscope H2, located downstream of the last spectrometer chamber, be set off.

4) GAMMA = $\overline{\text{GHF}} \cdot \text{GHR}\ (\geq 2)$

The gamma trigger was supplied by two identical 16-element scintillator hodoscopes, GHF and GHR, on either side of the spark chamber-lead converter "sandwich". A shower was indicated by a count in an element of GHR with no count in the corresponding element of GHF. At least two such "no-yes" combinations were required to initiate a gamma trigger.

5) ANTI = $\overline{\text{AA1} + \text{AA2} + \text{TA}\ (\geq 1)}$

There were to be no counts in any of the anti-counters.

CHARACTERISTICS:

Cathode Readout

Operational Voltage: 5.1 - 5.8 kV

Spatial Resolution: 1 wire/mm, 16 strips (see below)

Maximum Frequency: 5 MHz

Magic Gas: 0.5% freon-13 B1 (CF_3Br)

24.5% isobutane (iso C_4H_{10})

75.0% argon

READOUT AND SUMMING CIRCUITRY:

TTL Logic

Input Voltage: 5 - 40 mV

Output Voltage: NIM

Clusters sizes @ 1 wire/mm

59 wires	40	35	30	25	20	15	10	10	15	20	25	30	35	40	59 wires

FIGURE 6 Proportional Wire Chamber

CHAPTER 2

DATA COLLECTION AND RECONSTRUCTION ANALYSIS

In this chapter, we present a detailed history of our analysis, from data collection to "Data Summary Tape". A brief schematic is presented in Figure 7.

2.A. Online Data Collection and Analysis

Data acquisition and online analysis were performed on a General Automation SPC 16/85 computer interfaced to the experiment through a standard CAMAC network. The raw data for each event was stored in an event buffer consisting of 328 16-bit words. The collection system was capable of recording up to forty events per 600 msec ZGS pulse. All raw data were recorded on magnetic tape for later offline analysis.

Approximately thirty percent of the recorded events were analyzed online during the 4-second intervals between ZGS pulses. This provided a valuable means of monitoring the performance of the apparatus. All spark chamber efficiencies, scintillation counter participation, and lead glass block participation were readily available for a continuous and rapid check of the equipment performance.

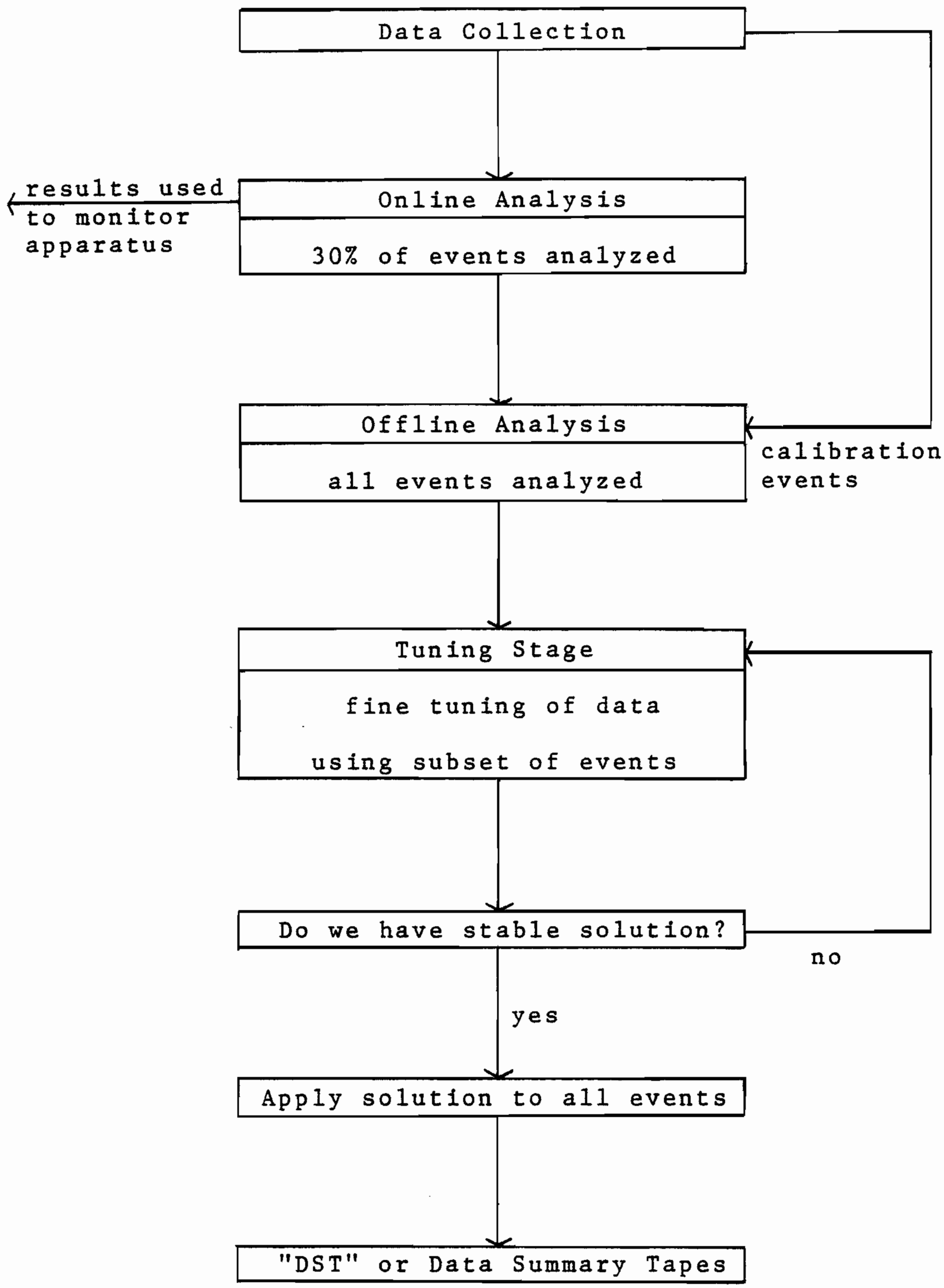

FIGURE 7 Analysis Schematic

2.B. Calibration Data

a) Spectrometer Data

To determine the exact spatial position of each chamber, the spectrometer chambers were fired and data recorded for a non-interacting beam event at the start of each ZGS pulse. This information was used in the offline analysis as a check on the surveyed positions of the spark chambers.

Also, the distance between the rear and front fiducials was monitored, thus allowing the distance per scaler count to be updated for each magnetostrictive ribbon. This updating corrected for the aging of the ribbons and any temperature effects.

b) Lead Glass Blocks

The energy deposited in each lead glass block was proportional to the ADC digitization readings. However, the proportionality constant varied due to changes in the photomultiplier tube gain caused largely by shifts in ambient temperature. To monitor the relative gain drifts between tubes, the light output from a nitrogen laser was piped to each block via fiber optics. Laser pulse height data were recorded at the start of each ZGS pulse, and then used by the offline analysis program to update the gains on a run-to-run basis. Twice daily, the laser pulse heights were recorded and utilized by the online analysis program to remove drifts.

An absolute calibration of each block was obtained by comparing the known π^o mass to the mass of all the π^o decays recorded during data-taking. The dominant contribution to the error in the π^o mass measurement came from the uncertainty in the shower energies. The gain of each tube was therefore corrected by the method outlined in Figure 8. Briefly, for all two-gamma shower events, a digamma mass distribution was formed for each block, with the histogram of each block being incremented whenever it was the center for one of the two showers. The ratio of the centroid of each block's histogram to the actual π^o mass was then calculated and used to correct the tube gains. This process was done at the end of the month's run.

2.C. Offline Analysis

All recorded events were analyzed offline on the Ohio State University Amdahl 470/V6 and on the University of Toronto IBM 370/165 computers using essentially the same software as the online program. However, the offline program made much greater use of the calibration data mentioned in section 2.B. A description of the software is given in the next section.

An analyzed event buffer for all events with two or

1) Formation of Histogram for Block #N

A) Calculate Di-Gamma Mass For All Block #N Events

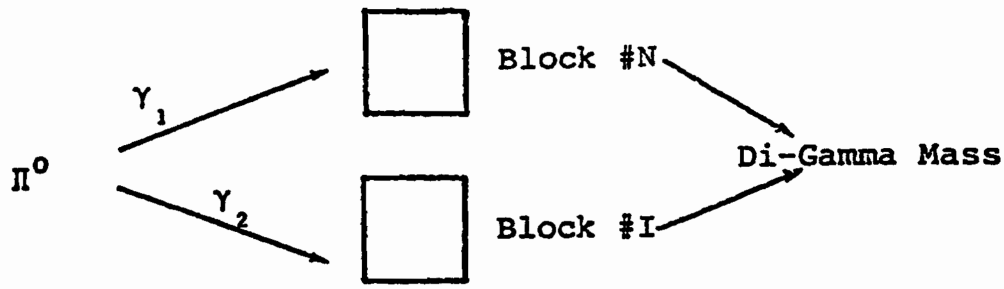

B) Sum Over All Blocks

$$\sum_{I=1}^{56}$$

C) Find Centroid Of Di-Gamma Mass Distribution And Compare With True π^o Mass

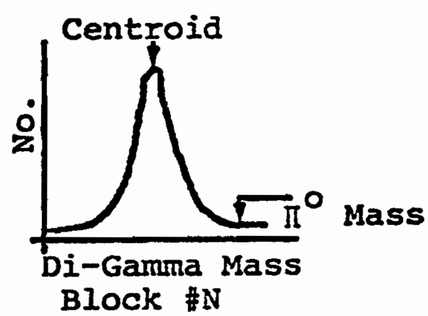

2) Correct Tube Gain For Block #N by Ratio

$$\left(\pi^o \text{ Mass} \,/\, \text{Centroid Mass}\right)^{1/2}$$

FIGURE 8 Method for Lead Glass Energy Calibration more charged particles was recorded on magnetic tape for further analysis of specific interactions. A breakdown of the recorded events is given in Table 4. About 41% had two oppositely charged pions; of these, about two thirds had two or more gamma showers.

2.D. Reconstruction Software

The reconstruction software, as mentioned above, was essentially the same for online and offline analysis. The sequence followed in the reconstruction of an event is outlined in Figure 9. The event reconstruction program was divided into three basic sections: the beam, the charged particles and the gamma rays.

a) Beam Reconstruction

The momentum, direction and position of the incident pion upstream of the target were determined using the information from the beam momentum hodoscope and the beam spark chambers. Multiple beam track ambiguities were resolved, if possible, with the use of the beam finger hodoscope BH10. Approximately 50% of such events were resolved; the rest were rejected and accounted for in the effective beam calculation. If a beam particle fired more than one beam hodoscope (BH) element, the event was taken as having one counter set at the average position.

TABLE 4

BREAKDOWN OF RECORDED EVENTS

Type	Percentage (%)	
Two charged events:	73.9%	
less than two gamma showers		40.9%
two gamma showers		37.5%
three gamma showers		16.6%
four gamma showers		4.3%
five gamma showers		.7%
Three charged events:	24.0%	
less than two gamma showers		50.3%
two gamma showers		32.3%
three gamma showers		13.6%
four gamma showers		3.3%
five gamma showers		.5%
Four charged events:	2.1%	
less than two gamma showers		46.6%
two gamma showers		34.6%
three gamma showers		14.6%
four gamma showers		3.6%
five gamma showers		.6%

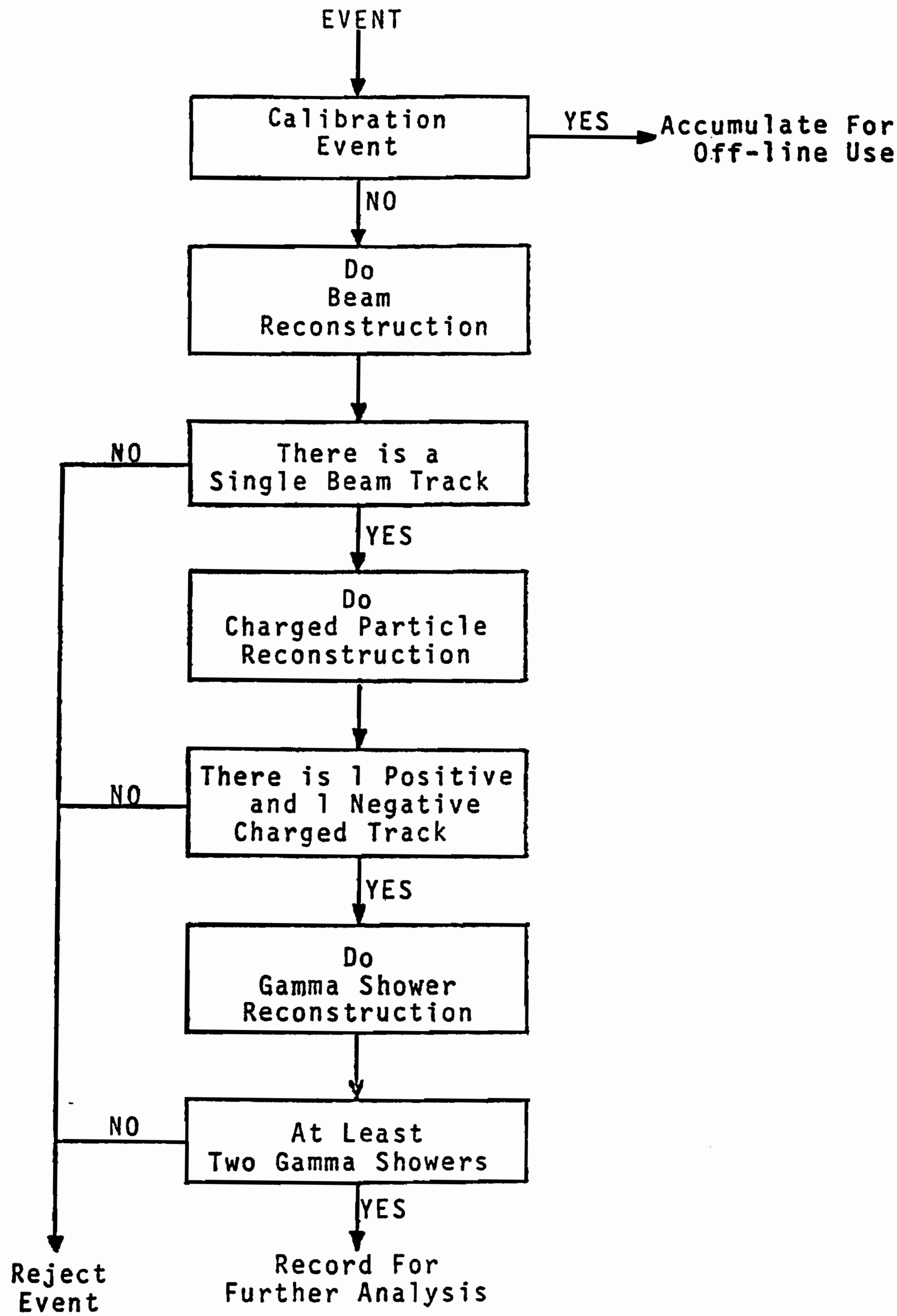

FIGURE 9 Software Reconstruction Analysis

b) Charged Particle Momentum Determination

The first step in determining the charged particle momenta is the calculation of the particle trajectories. A considerable amount of time was saved by demanding that in each view the sparks for a track candidate fall within a road defined by the charged particle hodoscope element dimensions, an imaginary grid similar to the charged particle hodoscope at the magnet center, and the hydrogen target dimensions. Tracks were first searched for in the downstream Y view and then in the downstream X view. For the rotated chambers, cross checks were done between the two views to further constrain the track candidates. The entire procedure was repeated for the upstream chambers. At this point, the track candidates having common sparks were pruned, and the tracks with the lowest chi-squared values were kept. The upstream and downstream tracks were next matched at the magnet center. A common intersection point of the two or more tracks with the beam track was also demanded. Analysis was aborted for events which did not have at least two such tracks. Before calculating the momentum of each charged particle, the tracks were corrected for bending outside the magnet, caused by the strong fringe field. Figure 10 shows the reconstructed trajectories for a three-pronged event.

The momenta of the surviving tracks were determined using the known corrected trajectories, in conjunction with

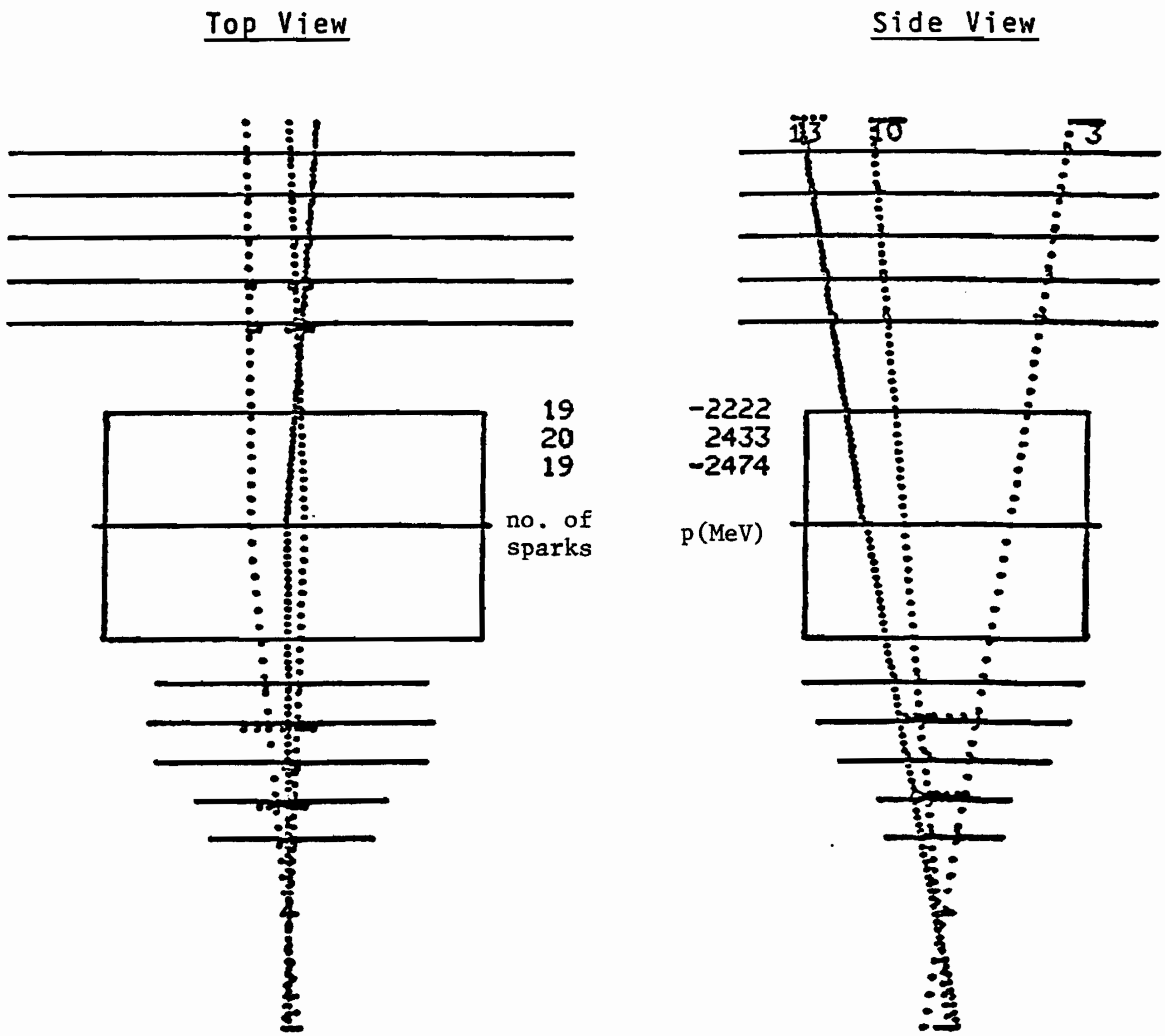

FIGURE 10 Example of a Reconstructed Three Prong Event

a momentum function consisting of a fourteen-term polynomial. This momentum function was developed [2] using numerical integration of Monte Carlo-generated tracks. A detailed magnetic field map was available for this purpose.

c) Gamma Shower Energy and Position Reconstruction

Events with one positive and one negative charged track were then checked for the presence of gamma showers. The reconstruction software was identical for all events, regardless of the number of gamma rays present. The procedure followed in determining the energy and position of each gamma ray shower is summarized in Figure 11. All candidates for showers were first required to have deposited an energy of at least 30 MeV in a single lead glass block. Then the gamma chambers were checked to see if, corresponding to that shower, there existed at least one X and one Y spark in either of the first two chambers, and at least one confirming spark in a subsequent chamber. The shower center was then taken to be the position of the leading X and Y sparks, or as the average position if more than one leading spark was found. Ambiguities resulting from the overlap of charged and gamma showers were eliminatd by rejecting an event if any gamma shower was found to be within 5.0 inches of an extrapolated charged particle trajectory.

The shower energy was determined by adding any energy deposited in surrounding blocks to that in the leading

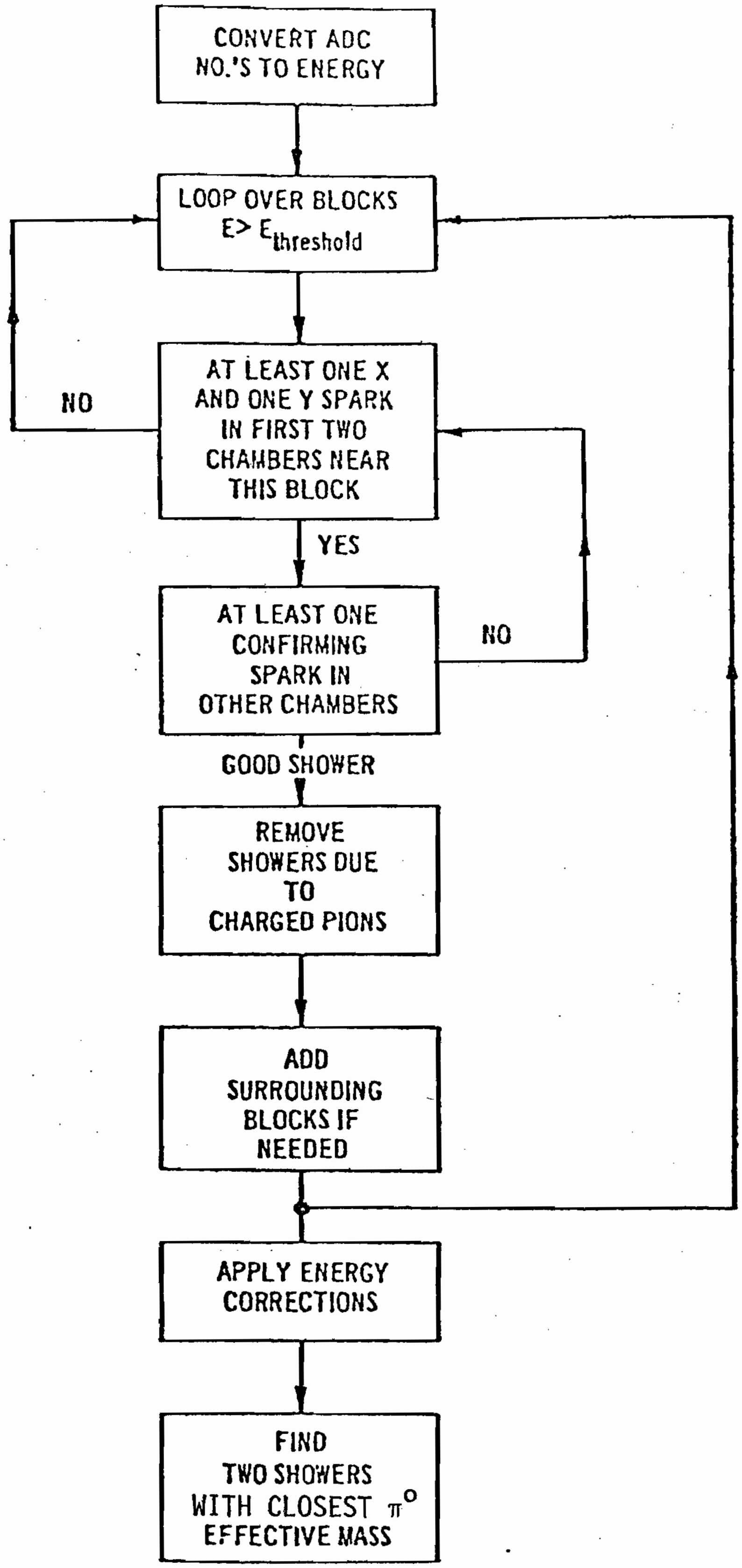

FIGURE 11 Gamma Shower Reconstruction Flowchart

block, and then correcting for energy losses in the lead converter, around the photomultiplier tube, and in the junction between blocks. For all events with two or more reconstructed showers (regardless of the actual number of showers), the two showers forming an effective mass closest to the π^0 mass were found and put first and second into the final analysed event buffer in decreasing order of energy. The rest of the gammas were buffered into subsequent positions in decreasing order of energy. In Figure 12, we present the reconstruction of a two gamma shower event.

2.E. Calibration or "Tuning" Software

In the "tuning" stage of the analysis, we fine-tuned the absolute positions of the spectrometer's spark chambers and the absolute and relative calibration of the gamma detector's lead glass blocks. Most of the software development was performed on the McGill University Amdahl 470/V7. The actual "crunching" was done on the Ohio State University Amdahl 470/V6.

The technique involved is described in detail in Appendix A. Briefly, the process was as follows: we parameterized the errors in charged particle positions as

$$\Delta x_i = \eta_i - y_i = p_{i1} + p_{i2}\frac{y_i}{z_i} + p_{i3}y_i + p_{i4}y_i^c + p_{i5}y_i y_i^c + p_{i6}y_i^2 + p_{i7}y_i^2 y_i^c + p_{i8}y_i^3 + p_{i9}y_i(y_i^c)^2 ,$$

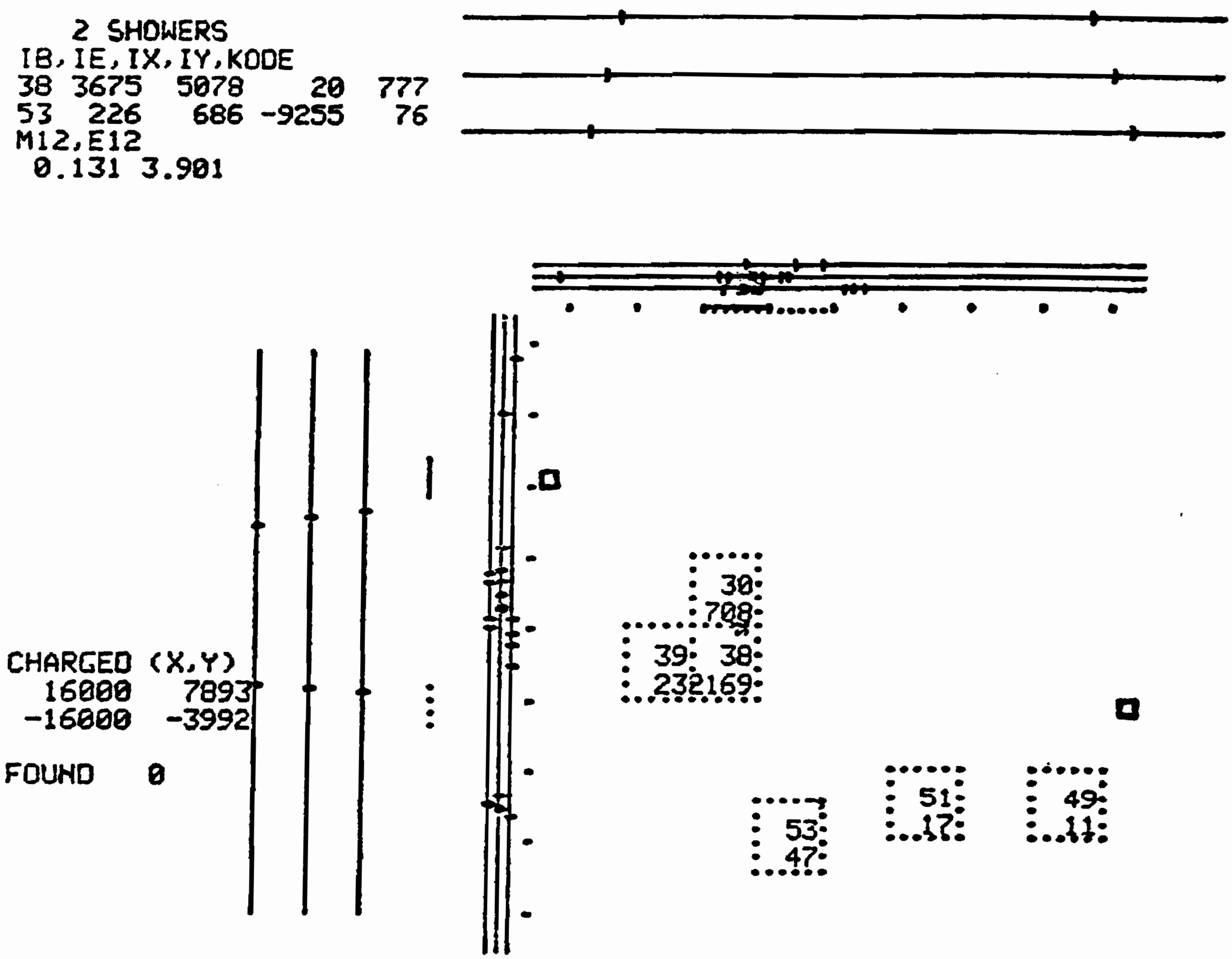

FIGURE 12 A Reconstructed 2γ Event

where y_i = coordinate being fitted,

y_i^c = coordinate conjugate to that being fitted,

z_i = z-coordinate of chamber plane

and η_i = fitted position, $i = 1,\ldots,20$ (=chamber plane),

and the error in gamma energies as

$$\Delta E_k = E_k^F - E_k^U = p_{k1} + p_{k2}E_k^U + p_{k3}(E_k^U)^{\frac{3}{2}} + p_{k4}(E_k^U)^{\frac{1}{2}} ,$$

where E_k^U = measured energy

and E_k^F = fitted energy, $k = 1,\ldots,56$ (=lead glass block).

We then analyzed a sub-sample of data and fitted for the parameters $p_{\cdot j}$ (the motivation for our choice of parameters is given in Appendix A). It was then possible to calculate new y_i and E_k^U and repeat the process until convergence was obtained. The final $p_{\cdot j}$ were then applied to the whole sample and the data re-analyzed.

In practice, a sample of 10,000

$$\pi^- p \to \omega N \qquad \omega \to \pi^+\pi^-\pi^o$$

events was used for this iterative process. The "tuning" of the charged spectrometer and of the gamma spectrometer were done independently. It was necessary to be very careful in the fitting, for, with such a large number of parameters, there were a large number of solutions, some better than others. In the spark chamber "tuning" alone, there were

$20 \times 9 = 180$ parameters to be found, and they could not all be determined at once. Some parameters were much more important than others (e.g., p_{i1}, the offset or surveyor's error, carried 100 times the weight of p_{i9}, the pincushion or "ballooning" parameter), and were solved for first.

Unlike the first stage of the analysis, where the charged particle trajectories were determined by Least Squares fitting and the momentum by a table lookup, in this final stage, we used a quintic spline fit to determine trajectories and momenta simultaneously. This improved the resolution by 20%. The spline fitting technique is explained in Appendix B.

CHAPTER 3

KINEMATIC ANALYSIS

3.A. Analysis of Four Gamma Events

All computer work in the "Data Summary Tape" stage of the analysis was performed at McGill University on an Amdahl 470/V7 high speed computer. Of the total number of events with two oppositely charged pions, 4.3% were found to have four gamma shower candidates. All such events were extracted and analyzed assuming the hypothesis (X = meson)

$$
\begin{array}{l}
\pi^- p \to Xn \\
\qquad \to \omega\pi^o(2) \\
\qquad\qquad \to \gamma\gamma \\
\qquad\quad \to \pi^+\pi^-\pi^o(1) \\
\qquad\qquad\qquad \to \gamma\gamma \quad .
\end{array}
\tag{3-1}
$$

We had 233,000 events, each with six possible combinations, as there are six ways to form two π^o's out of four gamma rays. Our convention for the numbering of these combinations is summarized in Table 5. For each combination we also present, in Table 5, the fraction of total events for which this particular combination was the "best" fit to the hypothesis (3-1) (the method for determining the "best" combination is discussed in Chapter 6). Examining Table 5,

TABLE 5

COMBINATION NUMBERING CONVENTION

Combination	$\pi^o(1)$	$\pi^o(2)$	"Best" Fraction
1	$\gamma_1\gamma_2$	$\gamma_3\gamma_4$	.446
2	$\gamma_1\gamma_3$	$\gamma_2\gamma_4$	.016
3	$\gamma_1\gamma_4$	$\gamma_2\gamma_3$	.033
4	$\gamma_2\gamma_3$	$\gamma_1\gamma_4$	.016
5	$\gamma_2\gamma_4$	$\gamma_1\gamma_3$	.018
6	$\gamma_3\gamma_4$	$\gamma_1\gamma_2$	.471

NOTE: The subscript on the γ refers to its position in the event buffer.

one notices that 92% of the "best" combinations are either combination 1 or 6. This is due to the internal ordering introduced by the reconstruction program. The gamma ray pair forming an effective mass closest to the π^o mass was stored in the first two buffer positions. For this reason, in the following we often plot effective masses using combination 1 only, or the sum of combinations 1 and 6. This is done simply for convenience and does not seriously bias the plots as the contribution from the other combinations is small.

Our initial $\pi^+\pi^-\gamma\gamma\gamma\gamma(4\gamma)$ data sample is presented in Figure 13. This is the starting point of our analysis and the only cuts applied on the data were done to avoid reconstruction problems for low momentum particles and inefficiencies of the detectors near their edges. These are cuts 1, 2, 5 and 6 of Table 6. There is no indication of a signal around the B(1.230) mass. Also given, in Figure 14, is the $\gamma\gamma$ effective mass from the same initial sample. This plot represents the sum of combinations 1 and 6 of $\pi^o(1)$ (or, equivalently, the sum of combinations 6 and 1 of $\pi^o(2)$).

This data sample was then subjected to the analysis described in Figure 15, using the rest of the cuts given in Table 6. Briefly, for a combination with both gamma pair effective masses within 40 MeV of the π^o mass, a "2C" fit was applied. Both pairs were constrained to yield the π^o effective mass. Then the missing mass squared was calculated and combinations satisfying a cut of .0 - 1.2 GeV were "3C"

TABLE 6

GEOMETRIC AND KINEMATIC CUTS

Energy and Momentum Cuts

1) Charged particle momenta: > .4 GeV/c

2) Gamma ray energies: > .2 GeV/c

3) Two gamma rays forming $\pi^o(1)$:

$$\text{ratio } \frac{\text{slow gamma energy}}{\text{fast gamma energy}} > .11$$

4) Two gamma rays forming $\pi^o(2)$:

$$\text{ratio } \frac{\text{slow gamma energy}}{\text{fast gamma energy}} > .085$$

Geometry Cuts

5) All charged and gamma ray trajectories within the detectors by 1".

6) Gamma ray to charged particle distance at lead converter > 5".

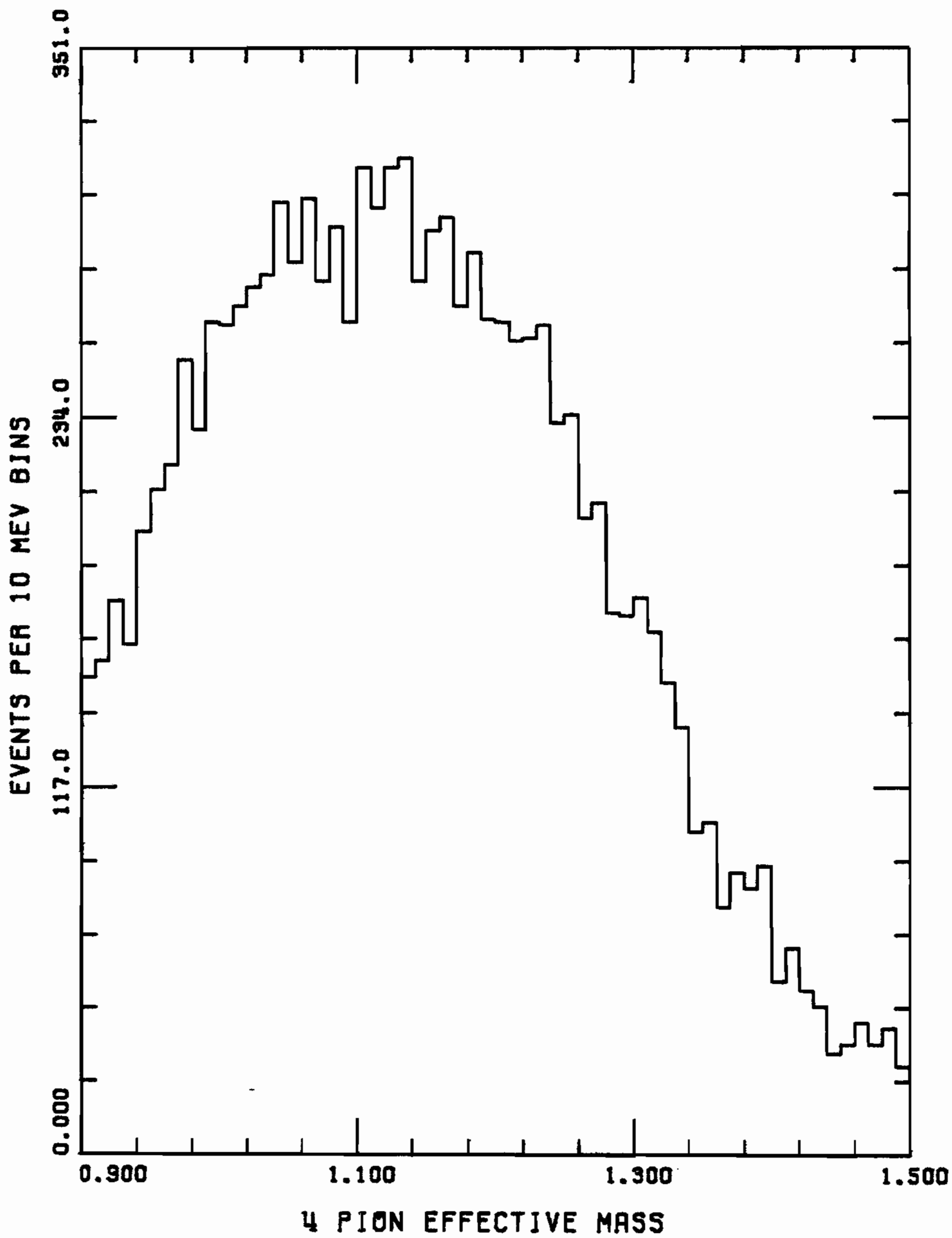

FIGURE 13 Initial 4π Sample

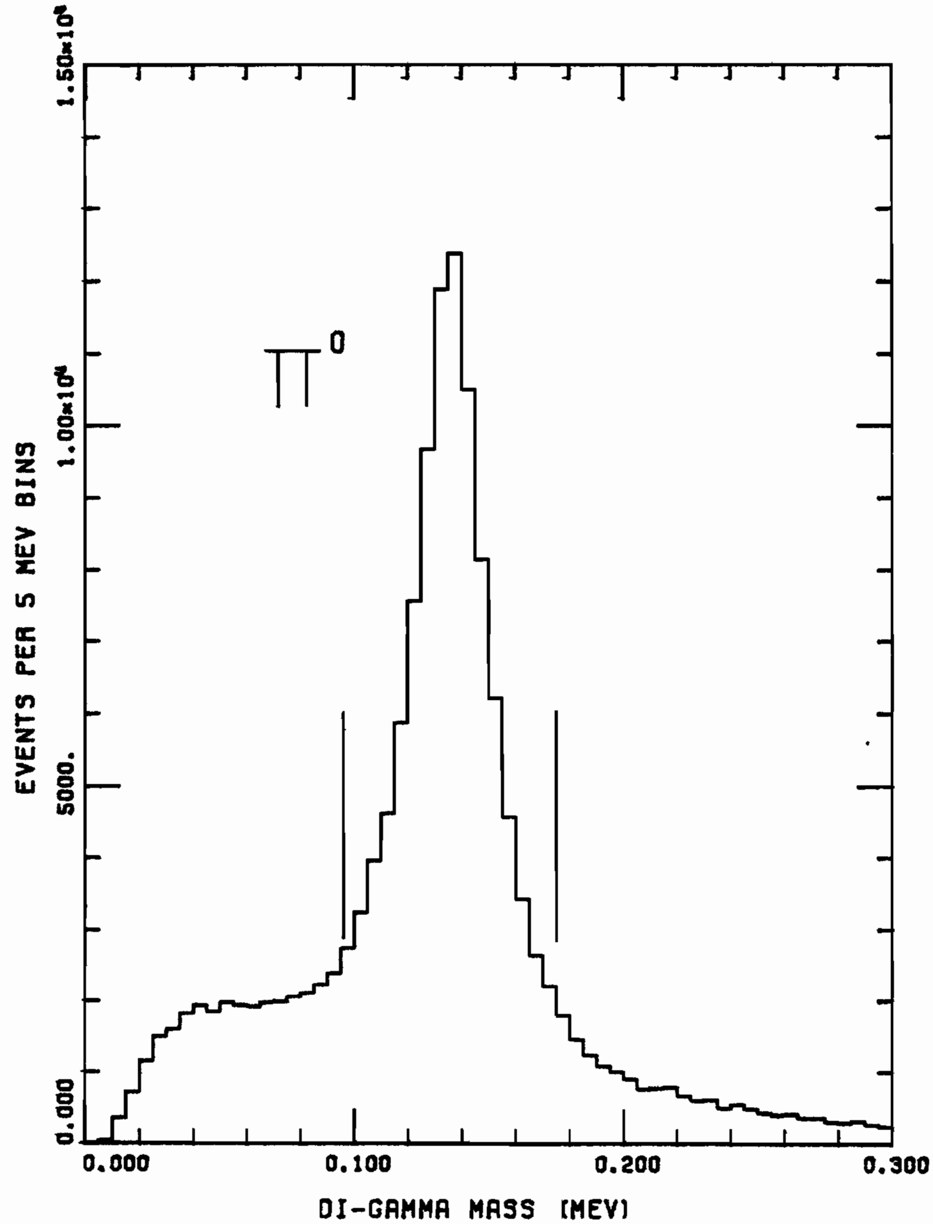

FIGURE 14 π^o Effective Mass

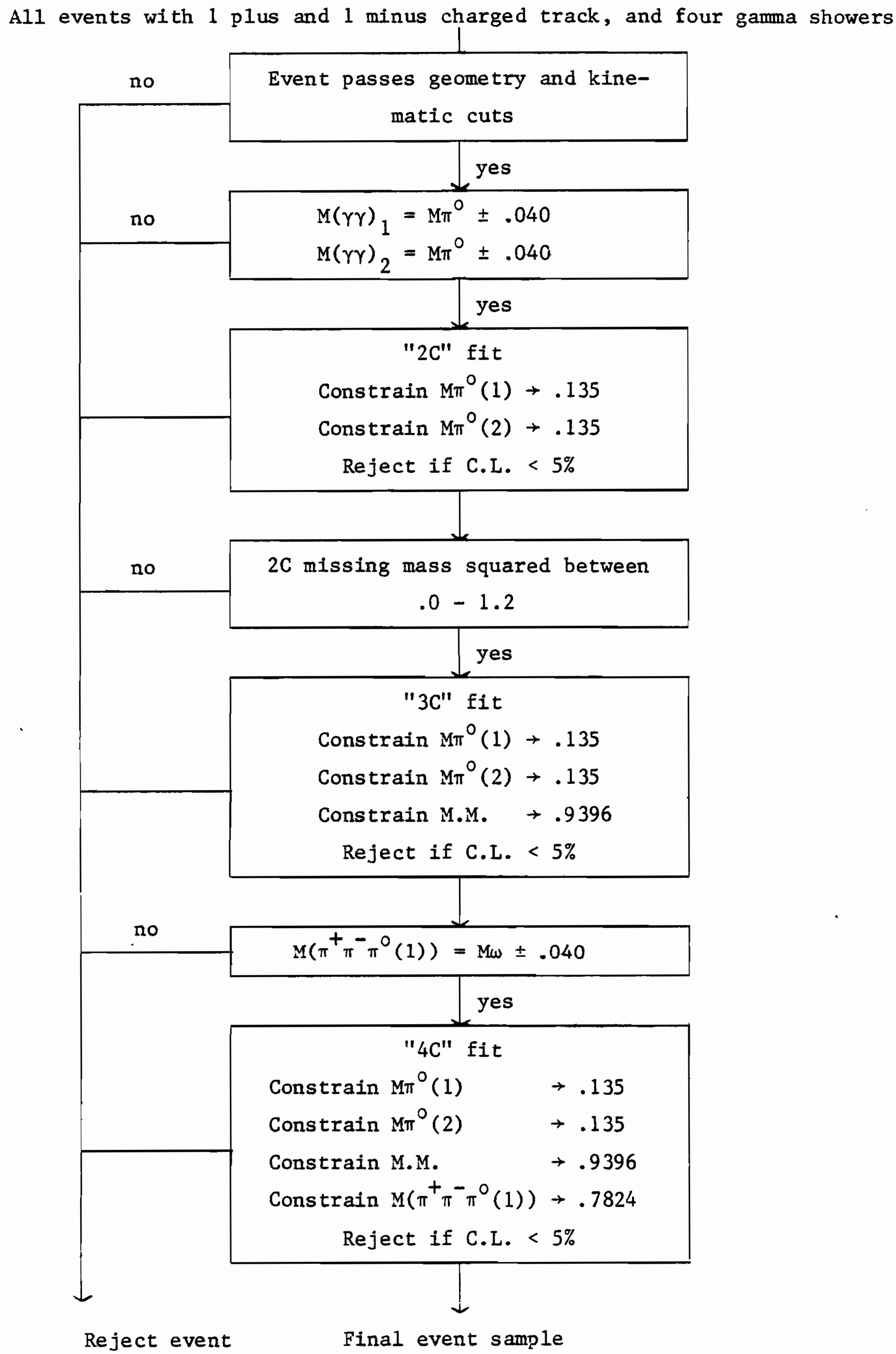

FIGURE 15 Kinematic Analysis Flowchart

fitted. The "2C" missing mass squared is plotted in Figure 16. The "3C" fit again constrained the gamma pairs to yield the π^o mass, and additionally imposed the constraint of forcing the missing mass to the neutron mass. The three pion ($\pi^+\pi^-\pi^o(1)$) effective mass was then calculated and the combination tested for the cut .740 ≥ "3C" ω ≥ .820. The "3C" ω effective mass is plotted in Figure 17. Again only combinations 1 and 6 are used. Surviving combinations are then "4C" fitted to hypothesis (3-1), yielding our final $\omega\pi^o$ sample. After each fit (2C, 3C and 4C), events in the lowest 5% confidence level region were rejected.

It is important to point out that often (approximately 50% of events) more than one combination of an event passed the above cuts. As already mentioned, the method of determining the best combination will be presented in Chapter 6. We have a total of 3123 events with at least one combination surviving all cuts; their effective mass spectrum is shown in Figure 18.

Detailed analysis of the cuts applied in our kinematic analysis, and of our final $\omega\pi^o$ sample, will be deferred to Chapter 6.

3.B. Analysis of Five Gamma Events

Our sample of events with two oppositely charged pions and two or more gamma showers also contained some 38,000

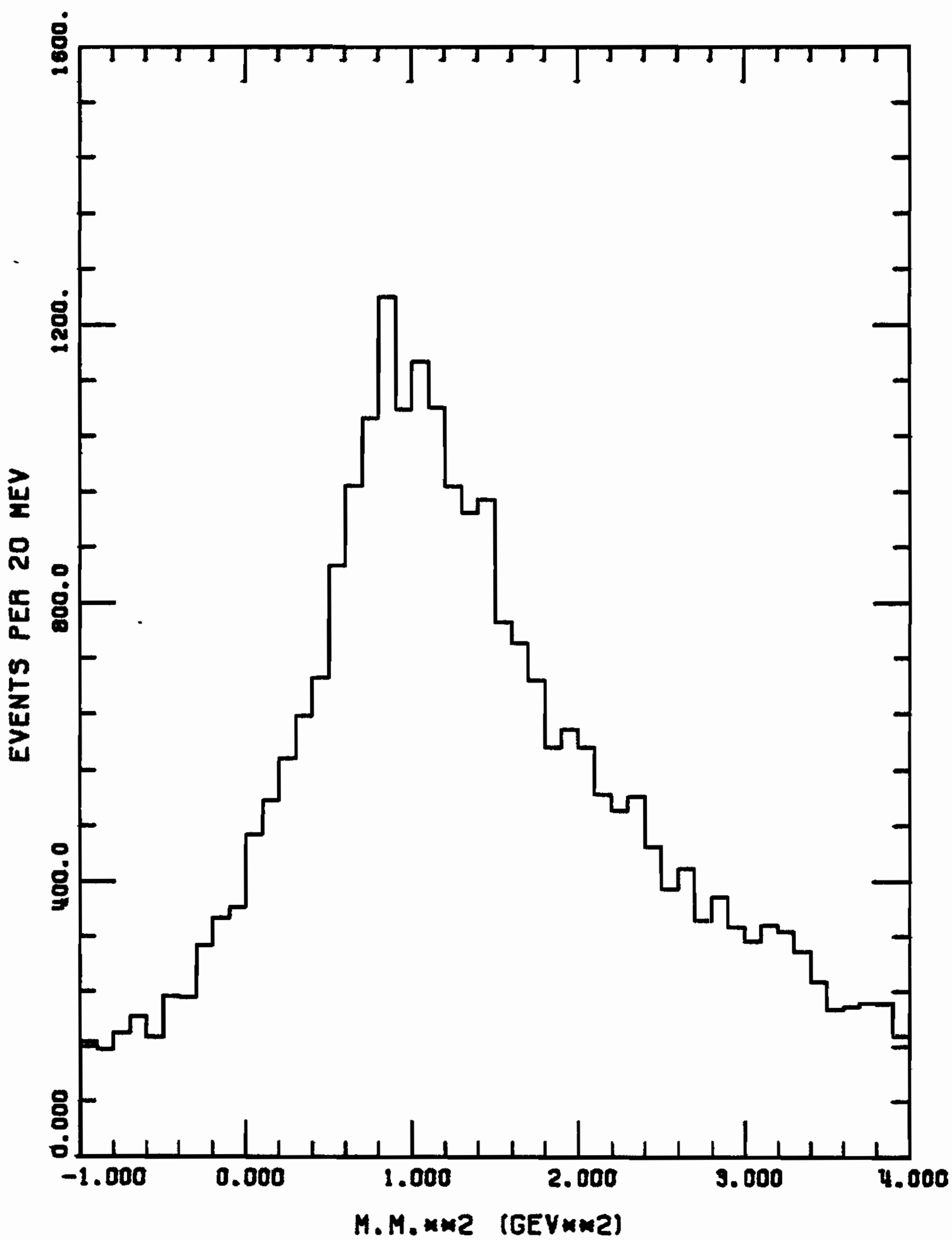

FIGURE 16 "2C" Missing Mass Squared

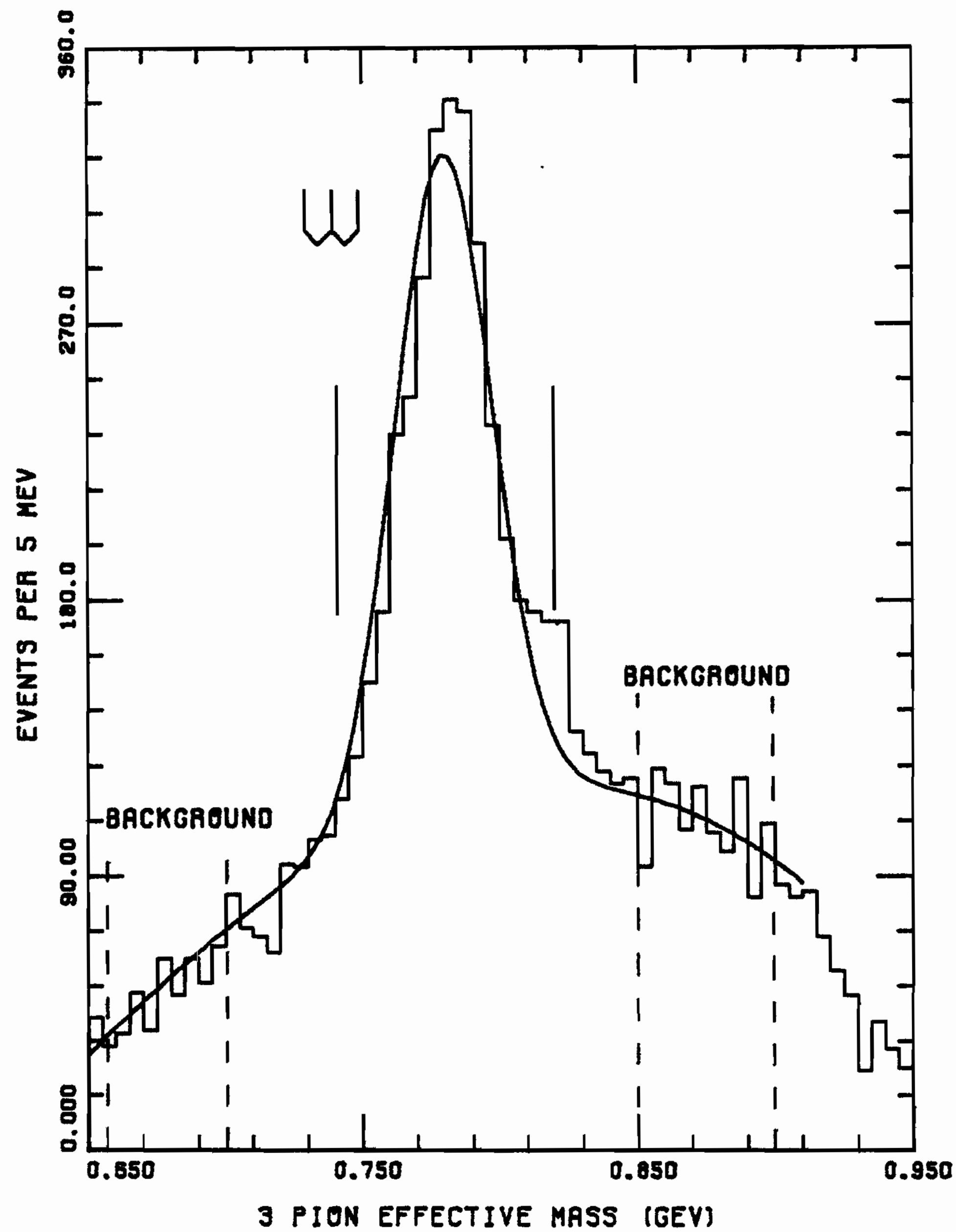

FIGURE 17 "3C" $\pi^+\pi^-\pi^0$ Effective Mass

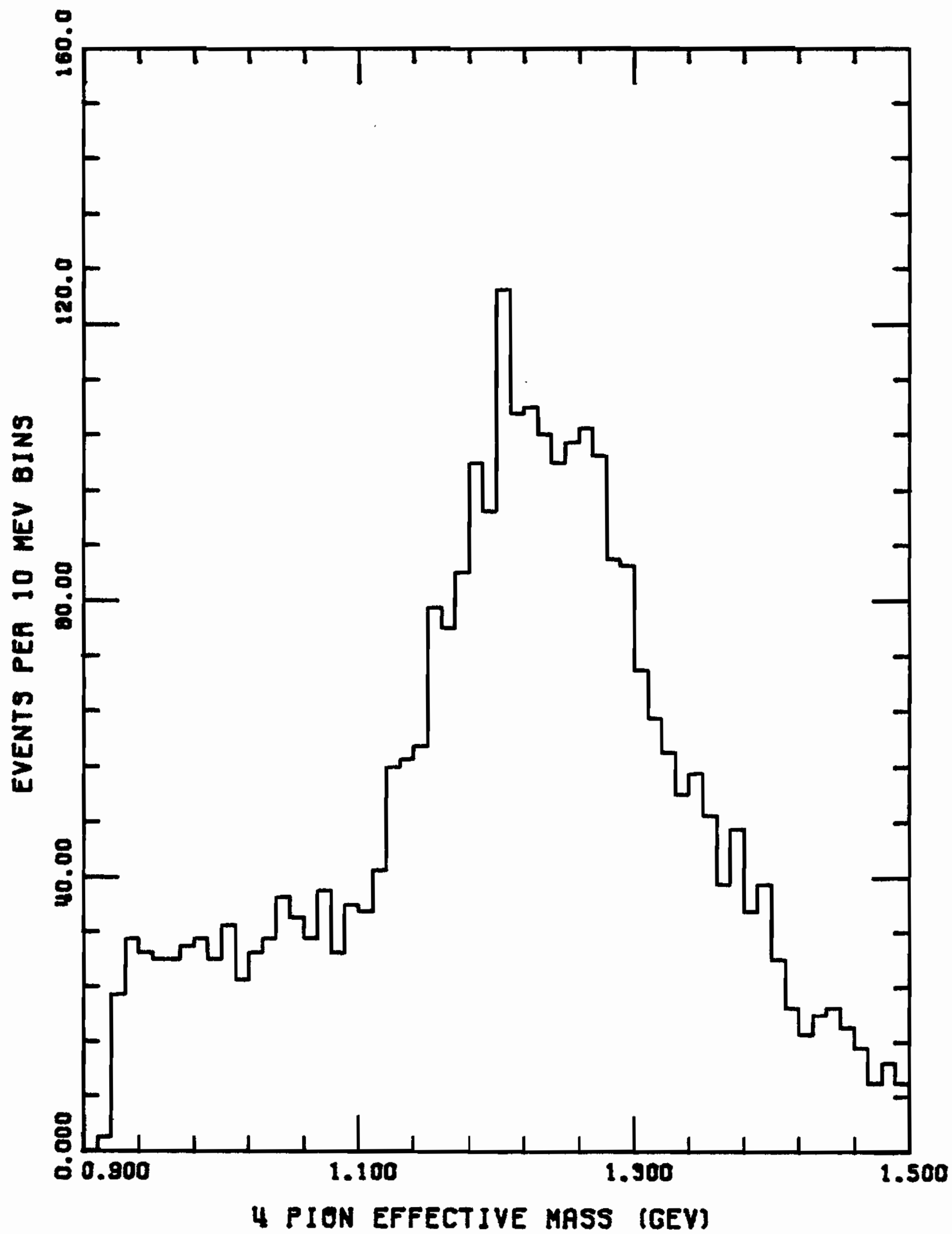

FIGURE 18 "4C" $\omega\pi^{o}$ Effective Mass events (.7%) with five gamma rays. We suspected that a large part of these events might actually be four gamma events with the addition of an accidental gamma ray, which was either due to the presence of an actual uncorrelated shower or, more likely, "created" by the reconstruction software. The four gamma rays giving the best π^o pairs were kept and analysis proceeded exactly as explained above in 3.A.

Again detailed analysis will be deferred to Chapter 6.

CHAPTER 4

EXPERIMENTAL RESOLUTION

Detailed studies of the measurement errors were made by a previous experiment [2] using the same apparatus. These results, with minor modifications due to higher average momenta, were also valid for this experiment. However, since the gamma shower detector was modified (additional lead converter was added), the parameterization of the error in the digamma mass was recalculated.

4.A. Beam

From Table 1, the beam momentum error was

$$\frac{\Delta p}{p} = .005 \quad \text{(FWB)} \ . \qquad (4\text{-}1)$$

The beam slope errors were very small with

$$\Delta\theta(\text{FWHM}) = ((1.3 \times 10^{-4})^2 + (.015/p)^2 t)^{\frac{1}{2}} \ , \qquad (4\text{-}2)$$

where the first term represents the angle error due to position measurement, and the second term is due to the multiple scattering of the beam in the target (t = number of radiation lengths of hydrogen seen by the beam and p is given in GeV).

4.B. Charged Particles

The charged particle momentum error was given by

$$\frac{\Delta p}{p}(\text{FWHM}) = ((.028)^2 + (.013p)^2)^{\frac{1}{2}} \quad . \qquad (4\text{-}3)$$

The first term is due to multiple scattering of the particles in traversing the spectrometer. The second term was found by using non-interacting beam events. A momentum error of 9% (FWHM) was calculated for beam particles, corresponding to a position error of .04 inches (FWHM) for each spark. Since typical two track events had an average position error of .05 inches, the measurement error at other momenta was then approximated by extrapolating the beam measurements.

The error in the charged particle angle measurement was

$$\Delta\theta(\text{FWHM}) = ((.0014)^2 + (.036/p)^2 t)^{\frac{1}{2}} \quad . \qquad (4\text{-}4)$$

The second term dominates the calculated error. It represents the multiple scattering in the hydrogen target. The first term was an estimate of the angle error in the position measurement.

4.C. Gamma Showers

The fractional error in the digamma effective mass is directly proportional to that of the measured gamma energies:

$$M_{12}^2 = 2(1 - \cos\theta)E_1E_2 = f(E_1,E_2) \quad . \qquad (4\text{-}5)$$

Therefore, we can write

$$(\partial M_{12})^2 = \frac{1}{4f}\,(\frac{\partial f}{\partial E_1})^2\partial E_1{}^2 + (\frac{\partial f}{\partial E_2})^2\partial E_2{}^2 \qquad (4\text{-}6)$$

and

$$\frac{\Delta M}{M} = \{\ \tfrac{1}{4}(\frac{\partial E_1}{E_1})^2 + \tfrac{1}{4}(\frac{\partial E_2}{E_2})^2\ \}^{\frac{1}{2}} \quad . \qquad (4\text{-}7)$$

Parameterizing our uncertainty in the gamma energy as

$$(\frac{\Delta E}{E})^2 = a^2 + 2b^2/E \quad ,$$

we obtain

$$(\frac{\Delta M}{M})^2 = a^2 + b^2(\frac{1}{E_1} + \frac{1}{E_2}) \quad . \qquad (4\text{-}8)$$

Plots were made of the digamma mass spectrum as a function of total energy of the two gamma rays. For each energy, the width of the peaks yielded the uncertainty in the energy. A fit to the correlation between the energy and its uncertainty gave

$$\frac{\Delta E}{E}(\text{FWHM}) = \left\{ (.130)^2 + \frac{(.217)^2}{E} \right\}^{\frac{1}{2}} \quad . \tag{4-9}$$

The shower position error was found by considering electrons transported through the apparatus. The positions determined by the spectrometer were compared with the positions found at the converter. The result was

$$\Delta x(\text{FWHM}) = .35'' \tag{4-10}$$

for all energies between 400 MeV and 2.0 GeV.

4.D. Resolution Functions

An estimate of the error in the various derived quantities of a B^o meson event is then obtained using the formulae (4-1) - (4-10) to smear the appropriate variables in conjunction with a Monte Carlo simulation program. The predicted experimental mass resolution functions for the π^o, ω, B^o and neutron squared are given in Figure 19. The events were simulated with a momentum transfer squared (t)

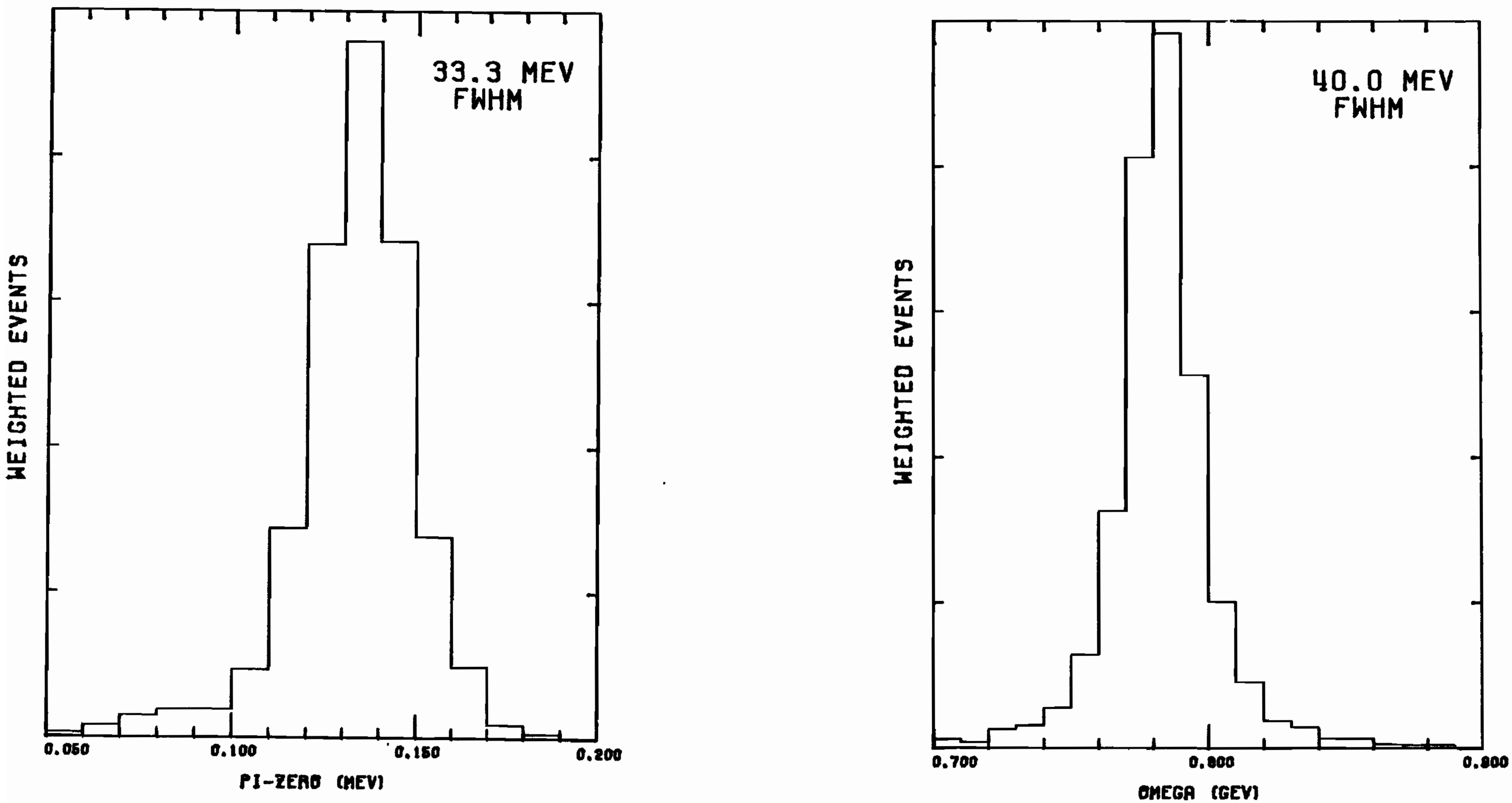

FIGURE 19 Resolution Functions

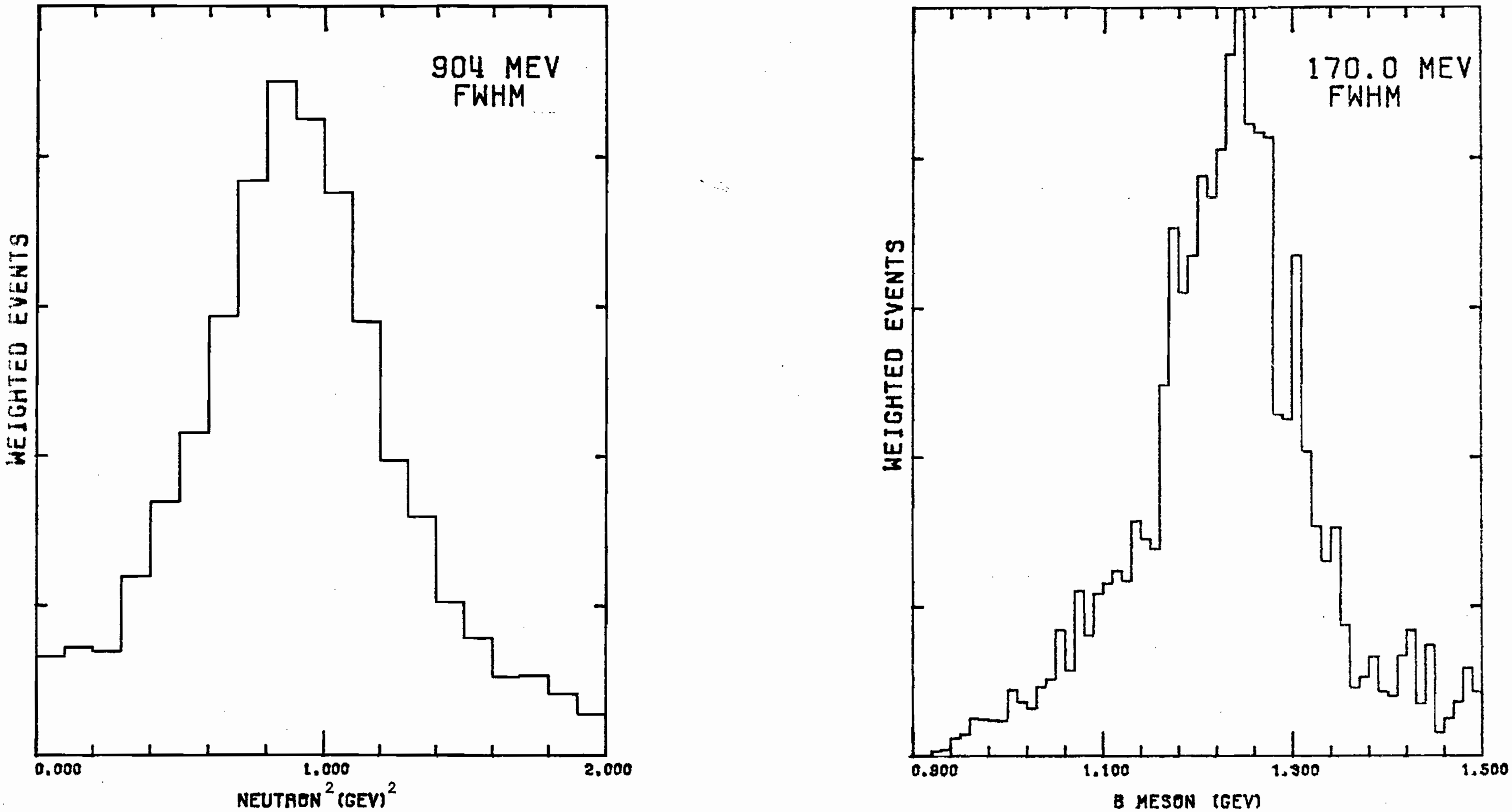

FIGURE 19 Resolution Functions (continued)

distribution as predicted by the data and with Breit-Wigner mass distribution widths of 10 and 128 MeV (FWHM), respectively, for the ω and B^{o}.

CHAPTER 5

EXPERIMENTAL ACCEPTANCE

To find the acceptance of the apparatus for the $\omega\pi^o$ reaction, we used a Monte Carlo simulation program described in Appendix C. Randomly generated events were deleted if they failed the geometric and kinematic cuts of Table 6. The program also included the statistical removal of events due to the charged pions decaying in flight, and the interactions of the pions and gamma rays in the hydrogen target. The whole process was performed for seven t-bins, with an average of 200,000 events generated for each bin. The final acceptance curve for a $J^P = 1^+ \rightarrow \omega\pi^o$ decay is plotted in Figure 20, and the acceptance for each t-bin is listed in Table 7.

It is important to note that the acceptance does not include an extra t-dependent correction due to our "tight" trigger mode of data collection. The stringent demands of the "tight" trigger caused losses of good events due to the rejection of an event because of a single recoiling neutron setting a TA counter. This correction is calculated in Chapter 7.

The average acceptance for our reaction is

$$.042 \pm .002 \quad .$$

The major error contribution is not statistical (<.001).

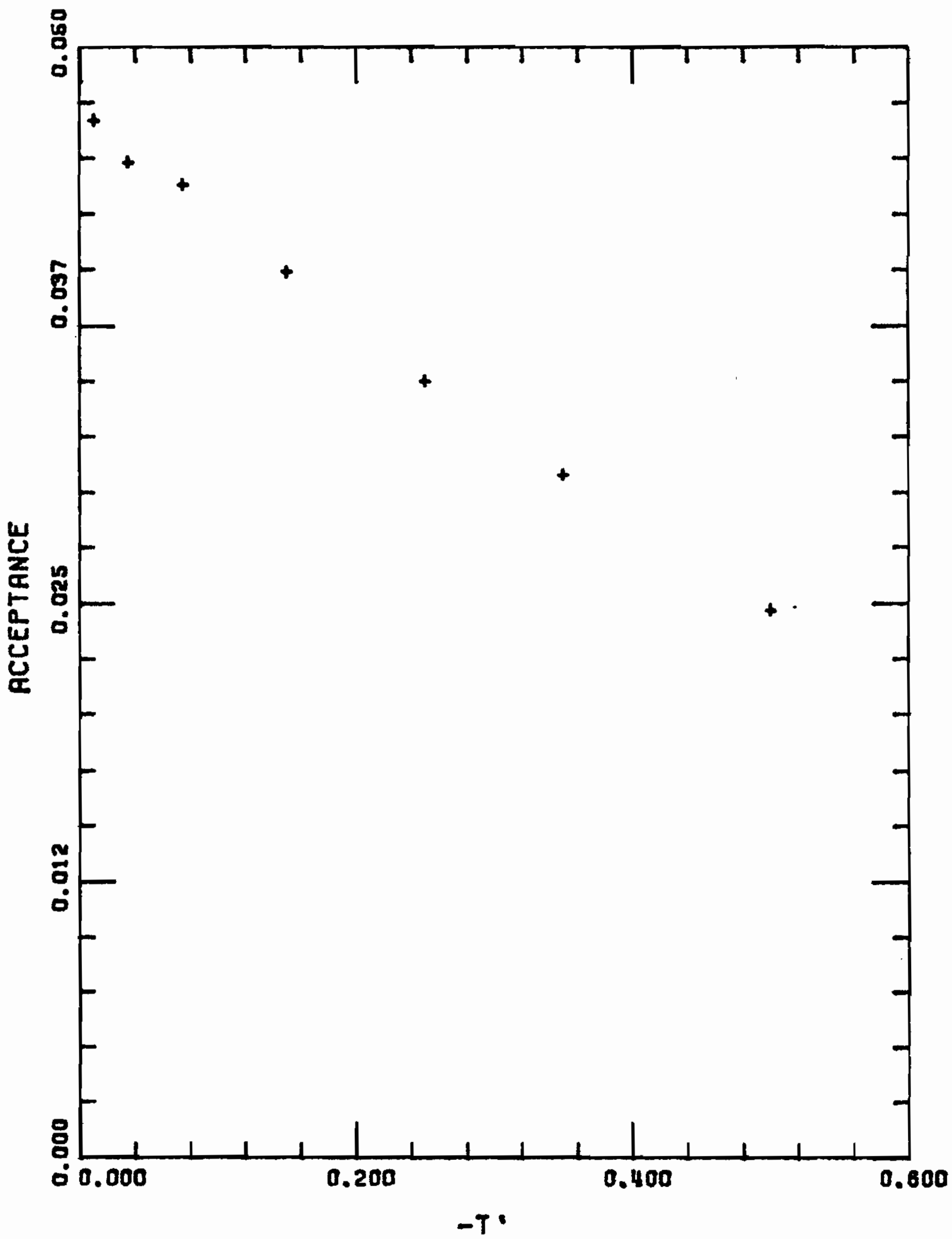

FIGURE 20 $\omega\pi^{o}$ Acceptance

TABLE 7

EXPERIMENTAL ACCEPTANCE ($J^P = 1^+ \rightarrow \omega\pi^o$)

-t'	Acceptance
.00 - .02	.047
.02 - .05	.045
.05 - .10	.044
.10 - .20	.040
.20 - .30	.035
.30 - .40	.031
.40 - .60	.025

Rather, the error bound is a measure of how well we understand our acceptance. Various tests of the Monte Carlo program (see Appendix C) lead us to believe that the relative error in the acceptance is 5%. This is a conservative estimate.

CHAPTER 6

SELECTION OF FINAL EVENT SAMPLE

In this chapter we will first discuss the reasons for our various cuts and the loss of good events resulting from those cuts on our data. We will then discuss the background and how we contend with it.

6.A. Kinematic and Geometric Cuts

These cuts are summarized in Table 6. Briefly, cut 5 removed the possibility of biases due to the inefficiencies of the detectors near their edges. Cut 6 removed events in which the measured energy of a gamma shower might have been augmented by the energy of a charged pion due to the proximity of that charged pion to the gamma shower. Cuts 1, 2, 3 and 4 were applied on the data to avoid reconstruction problems for low momentum particles. These cuts were determined by gradually loosening their values until the signal to noise ratio of π^0, ω and B^0 effective mass plots grew significantly worse.

The losses due to the aforementioned cuts are corrected for in the Monte Carlo acceptance calculation presented in Chapter 5.

6.B. Neutral Pion Mass Cut

To isolate combinations with two π^o's in the final state, a cut of 95 MeV to 175 MeV was made on both $(\gamma\gamma)$ effective masses if they survived the previous cuts. The effective mass spectrum for the sum of combinations 1 and 6 is given in Figure 14 with lines indicating the cutoff region. The data was fitted to a gaussian plus a fourth order polynomial representing background [9]. We obtained a width of 33.5 ± .65 MeV (FWHM) for the π^o peak. This is in excellent agreement with the resolution function of Figure 19. The fractional loss of good events due to the π^o mass cuts is thus < .5% whether one uses the resolution function or the fit to the data. These fairly loose mass cuts were used as slightly tighter cuts did not significantly improve the signal to background ratio of the B^o in the final $\omega\pi^o$ sample. Since we are dealing with low statistics we opted for the larger data sample.

6.C. Missing Mass Cut

The "2C" missing mass squared for events with two π^o's is given in Figure 16. There is a clear neutron signal on a large background. We feel that some of the background comes from the contamination of our $(B^0 n)$ data by Δ^0's; e.g.,

$$\pi^- p \rightarrow B^0 \Delta^0(1234) \quad \left.\right|\!\rightarrow n\pi^0 \qquad (6\text{-}1)$$

Results from various fits to the missing mass squared data lend support to our claim. The data were first fitted to a mass resolution function shape (for the neutron) plus a fourth order polynomial and then to neutron and Δ^0 mass shapes plus background (represented again by a fourth order polynomial). The latter was a 40% better fit, and produced the following results:

$$M(\text{neutron})^2 = .85 \pm .05 \ \text{GeV}^2$$
$$\Gamma(\text{neutron}) = 950 \pm 15 \ \text{MeV (FWHM)}$$
$$M(\Delta^0)^2 = 1.51 \pm .05 \ \text{GeV}^2$$
$$\Gamma(\Delta^0) = 954 \pm 15 \ \text{MeV (FWHM)} \ .$$

We discuss the background further in 6.F.

In order to remove most of the above contamination and other sources of background, we make a .0 - 1.2 GeV^2 cut on the "2C" missing mass squared for all events. The fractional loss of good events is estimated to be (21.0 ± 1.3)% and the fraction of Δ^0 contamination is (22.8 ± 1.5)%.

6.D. Omega Mass Cut

The "3C" three pion effective mass for those combinations with two neutral pions and a "2C" recoil mass satisfying the appropriate cuts is plotted in Figure 17. There is a clear $\omega(780)$ signal sitting on substantial background (the background is approximately 40% in the region defined as ω). A mass cut of 740 - 820 MeV was made to isolate combinations with an ω in their final state. As was the case for the neutral pions, we chose these limits to improve statistics. Tighter cuts did not significantly improve the final B^o signal.

The calculation of the good event losses was done by choosing the background regions shown in Figure 17 and assuming a fourth order polynomial fit to the background between the two areas. The result was a 41.5 ± 3.3 MeV (FWHM) signal, implying a fractional loss of events of $(2.5 \pm .2)\%$. To account for the experimental mass resolution in the ω mass region, the resonance shape was described by a Breit-Wigner function with the mass resolution folded in; the resulting fit is shown in Figure 17. The fitted values for mass and width of the ω are

$$M(\omega) = 780 \pm 4 \text{ MeV}$$

$$\Gamma(\omega) = 12.5 \pm 3.0 \text{ MeV}$$

in close agreement with the world average values [4] .

The decay matrix element squared or Dalitz plot density

$$\lambda = \frac{\left|\bar{p}_{\pi^+} \times \bar{p}_{\pi^o}\right|^2}{\frac{3}{4}(m^2_{3\pi}/9 - m^2_{\pi})^2}$$

for the three pion events within the mass cut is shown in Figure 21. The distribution is consistent with that of a $J^P = 1^-$ particle. Also plotted (Figure 22) are the dipion effective mass ($M_{\pi^+\pi^-}$) and $\mu = \hat{p} \cdot \hat{q}$, where $\hat{p}$ and $\hat{q}$ are as follows: the omega decay is analyzed in terms of a single pion plus a dipion. Each pion of the dipion is assigned a momentum $\bar{q}$ (in the dipion rest frame), and the remaining pion is assigned a momentum $\bar{p}$ in the ω rest frame. The results are consistent with those expected for the ω [7] .

6.E. Summary of Good Event Losses

Since we are calculating the cross section for

$$\begin{array}{l} \pi^- p \to B^o n \\ \quad\quad\;\; \lfloor\!\to \omega\pi^o \\ \quad\quad\quad\;\; \lfloor\!\to \text{all} \end{array} , \tag{6-2}$$

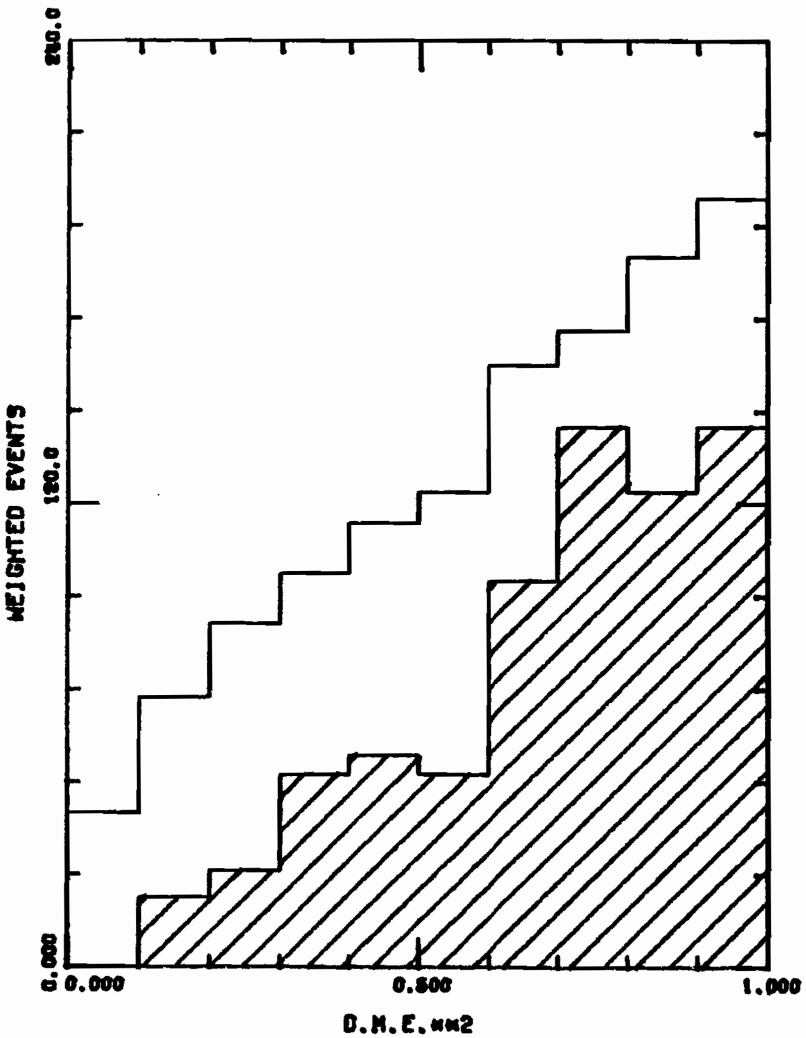

FIGURE 21 λ

The top histogram includes all events in signal region .740 - .820 GeV; shaded histogram includes all events, corrected for background with weight as per Breit - Wigner plus fourth order polynomial . It can be seen that the λ distribution after background subtraction is proportional to the distribution before subtraction , as expected for a pure ω sample.

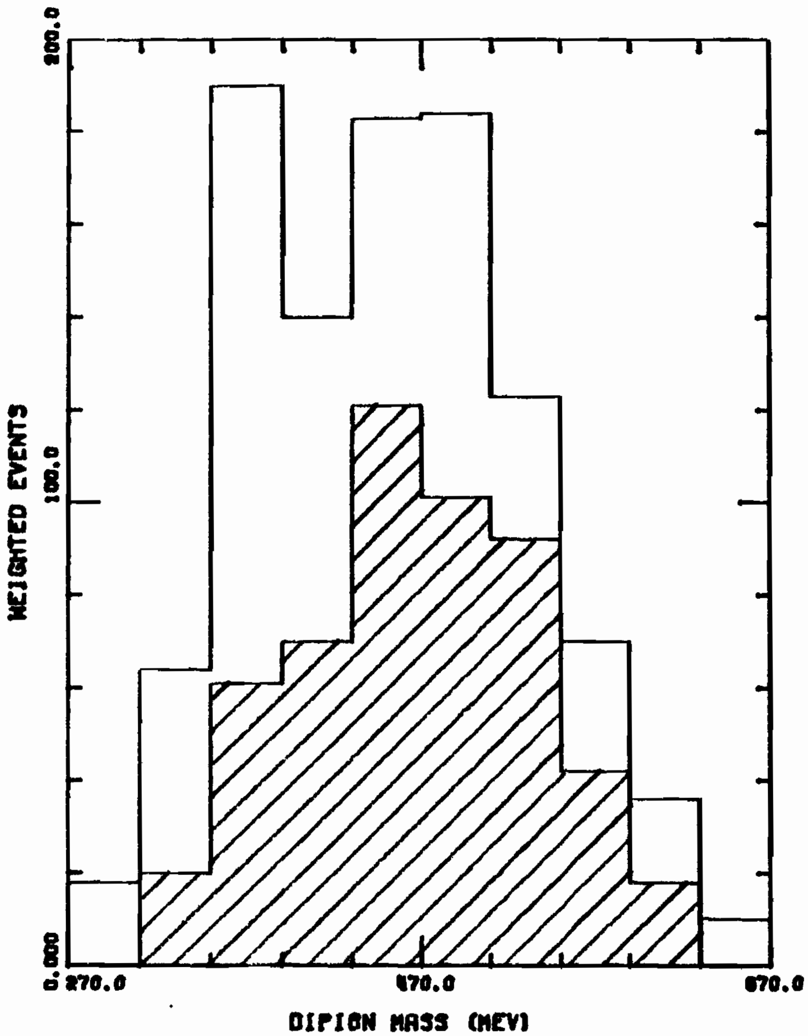

FIGURE 22a $M_{\pi^+\pi^-}$ (MeV)

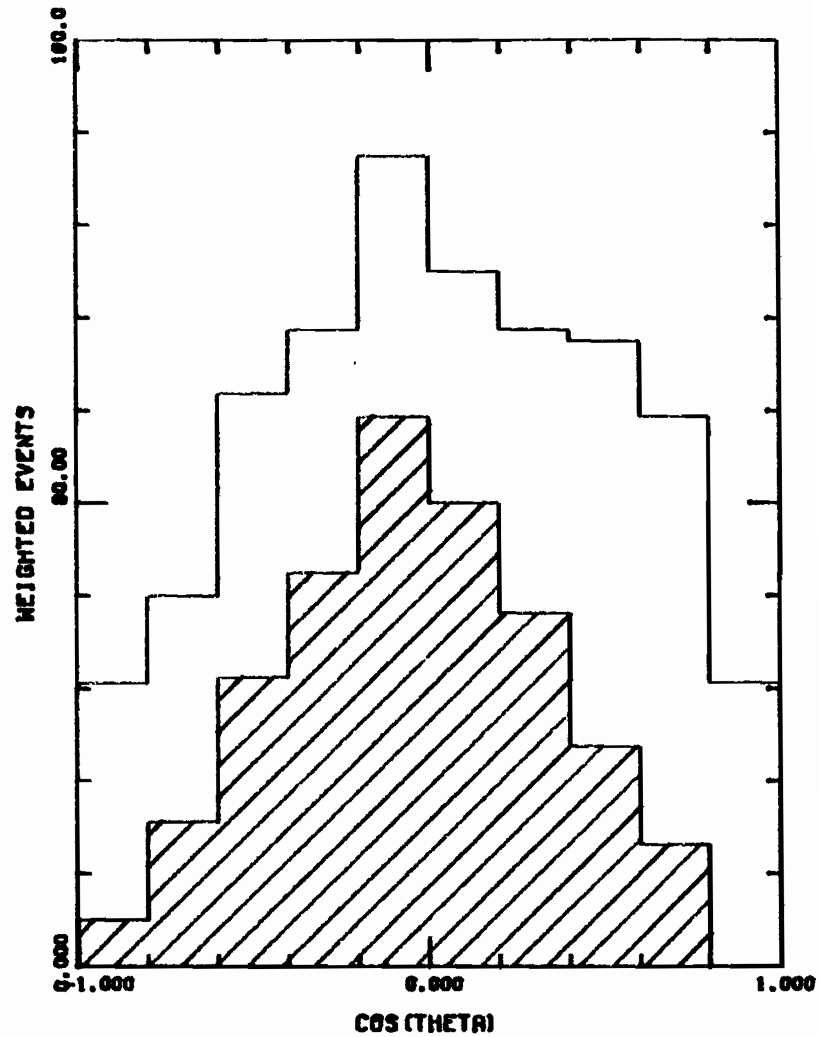

FIGURE 22b $u = \hat{p} \cdot \hat{q}$

we must correct for ω decay modes not detected by our apparatus. This correction factor is simply .898 ± .005 [4].

The above factor and all mass cuts are listed in Table 8 along with the calculated event loss fractions. The net correction factor was calculated to be .43 ± .04. This factor will be used in the differential cross section calculations.

6.F. Background

As already mentioned earlier, we feel that some of our $(B^o n)$ data is actually

$$\begin{array}{l} \pi^- p \rightarrow B^o \Delta^o \\ \qquad\quad\ \ |\quad \lfloor\!\rightarrow n\gamma\gamma \\ \qquad\quad\ \ \lfloor\!\rightarrow \pi^+\pi^-\gamma\gamma\gamma\gamma \quad . \end{array} \tag{6-3}$$

The contamination is expected to be small because the Δ^o through its decay products $p\pi^-$ and $n\pi^o$ should be detected by our target anti-counters and the trigger vetoed. Contamination is possible as Monte Carlo simulations show that the acceptance for $\pi^- p \rightarrow B^o \Delta^o$ is approximately the same as that for $\pi^- p \rightarrow B^o n$, if we assume that the Δ^o is not detected by the target anti-counters. The likelihood of this occuring is not minimal as the Δ^o is generally very low in energy and its decay products, $n\pi^o$, could avoid

TABLE 8

MASS CUT CORRECTIONS

Correction	Fraction Loss
Mass of $(\gamma\gamma)_1$ = 135 ± 40 MeV	.005
Mass of $(\gamma\gamma)_2$ = 135 ± 40 MeV	.005
Mass of $(\pi^+\pi^-\pi^o(1))$ = 780 ± 40 MeV	.025 ± .002
Mass of $(\omega\pi^o(2))$ = 1.230 ± .135 GeV	.370 ± .060
Mass $(\text{recoil})^2$ between .0 and 1.2 GeV^2	.210 ± .013
ω unseen decays	.102 ± .005

CORRECTION FACTOR = .43 ± .04

detection. A cut of 1.2 GeV^2 on the missing mass squared removes some of this background but a Δ^o fit to the missing mass shows that 22% remains under the neutron peak, which amounts to only 8% of the total signal. This is taken into account by using a $B^o\Delta^o$ type reflection as part of the background of the "4C" $\omega\pi^o$ sample. That is, events were simulated with a Δ^o mass distribution ($mass^2 < 1.2\ GeV^2$) and then "4C" fitted to give the required $\omega\pi^o$ distribution.

Another source of background could be the reaction

$$
\begin{array}{l}
\pi^- p \rightarrow \omega^o \Delta^o \\
\qquad\qquad\quad \Delta^o \rightarrow n\pi^o \\
\qquad\qquad\qquad\qquad \pi^o \rightarrow \gamma\gamma \\
\qquad\qquad \omega^o \rightarrow \pi^+\pi^-\pi^o \\
\qquad\qquad\qquad\qquad \pi^o \rightarrow \gamma\gamma \quad .
\end{array}
\qquad (6\text{-}4)
$$

However, our apparatus has no acceptance for this reaction, the neutral pion (from the Δ^o decay) being too "soft". Our data confirms this, as effective mass plots of $n\pi^o$ combinations show no signal at the Δ^o mass.

We also considered the 38,000 5γ events and the possibility that these events, or some part thereof, might actually be 4γ events with the addition of a fictitious gamma ray. Therefore, the 5γ data was analyzed as detailed in Chapter 3 and the results were as follows: only 196 events survived all cuts and their $\omega\pi^o$ effective mass plot had no significant enhancement anywhere. Moreover, very few of these events had a missing mass within 100 MeV of the neutron mass, implying a very poor fit to the hypothesis

$$\pi^- p \rightarrow B^o n \quad + 1\gamma \text{ (fictitious)} \qquad (6\text{-}5)$$
$$\quad\ \ \ \lfloor\!\rightarrow \pi^+\pi^-\gamma\gamma\gamma\gamma \quad .$$

We believe, therefore, that almost none of the 5γ events were of the type (6-5).

6.G. The Final $\omega\pi^o$ Sample

In Figure 23, the acceptance-corrected mass distribution $M(\omega\pi^o)$ is given for the 3123 events with $M(\pi^+\pi^-\pi^o(1))$ in the ω region and both $M(\gamma\gamma)$ in the π^o region. As explained in Chapter 3, there are six possible B^o combinations for each event. Whenever two or more combinations survived all cuts, the "best" B^o combination was chosen to be the one with the largest ω decay matrix element. It is the effective mass of these B^o's that has been plotted in Figure 23. The predominant feature is the strong B^o signal. We have some 2000 events in the B^o region, defined as

$$M(\omega\pi^o) = 1.095 - 1.365 \text{ GeV} .$$

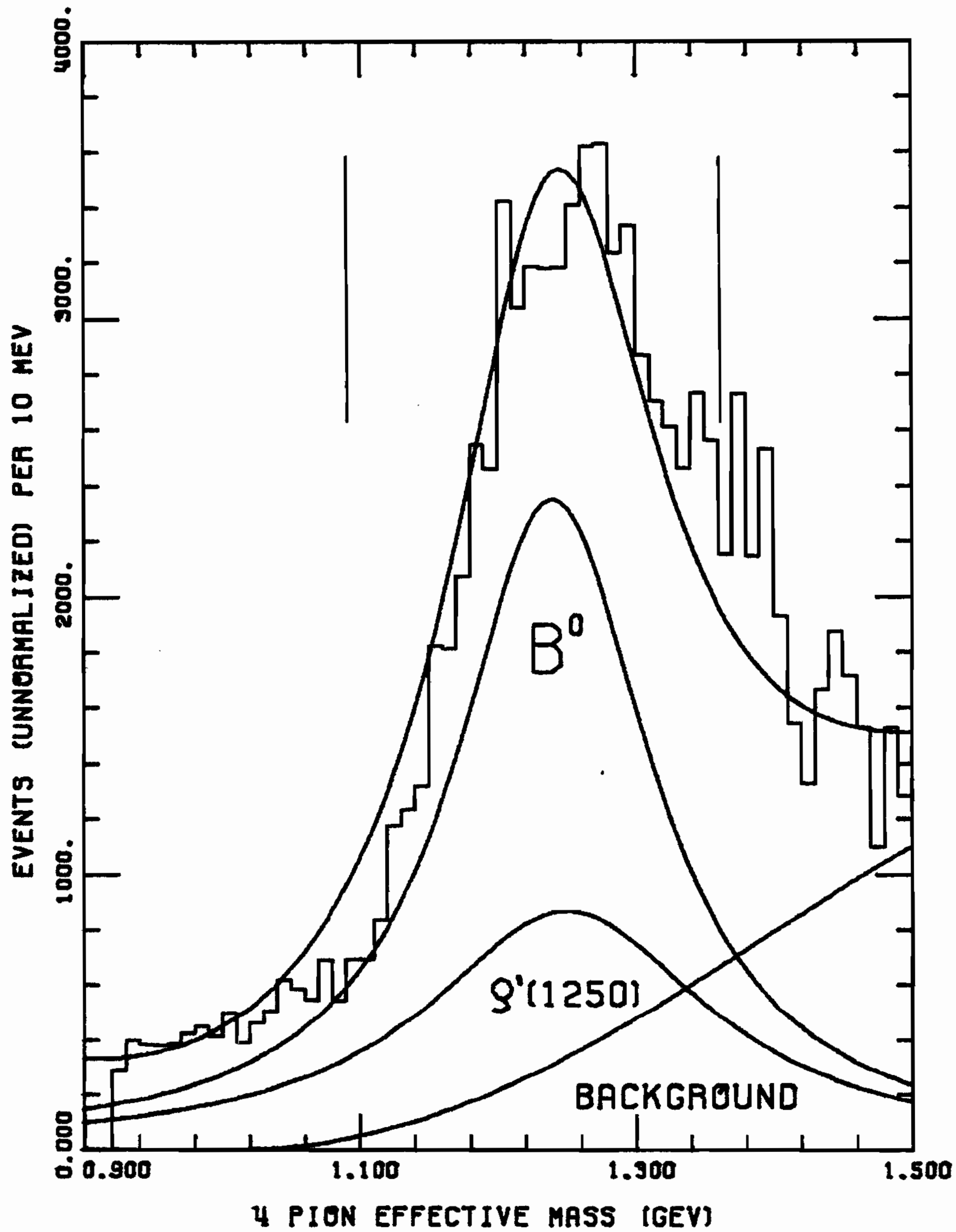

FIGURE 23 Acceptance-corrected "4C" $\omega\pi^0$ Effective Mass

No anomaly in the ω Dalitz plot is found [10] and the B^{o} signal appears strongly with ω's located at the center as well as at the periphery of the Dalitz plot.

As discussed in Chapter 10, where we present a sequential decay analysis of $B^{o} \rightarrow \omega\pi^{o}$ and $\omega \rightarrow \pi^{+}\pi^{-}\pi^{o}$, we have also observed a $J^{P} = 1^{-}$ signal under the B^{o} . 24% of non-background events in the full mass, full t' analysis were found to be 1^{-} . We feel that this is the $\rho'(1250)$ resonance (i.e., radial excitation of $\rho(770)$). A good fit is obtained by assuming a linear combination of Breit-Wigner resonance shapes for the B and ρ' mesons (with resolution at the B mass folded in), reflection from the state $B^{o}\Delta^{o}$, and the Monte Carlo generated phase space for $\omega\pi^{o}n$. The ρ' was fixed with a center of 1.250 Gev and a width of 250 MeV (FWHM) [11] . The resulting fit is shown in Figure 23. We obtained

$$M(B^{o}) = 1.236 \pm .010 \text{ GeV}$$

$$\Gamma(B^{o}) = 140 \pm 20 \text{ MeV}$$

and $$\chi^{2} \text{ (57 degrees of freedom)} = 64 \quad .$$

The fraction of ρ' was found to be .30 ± .05, while the fraction of good events lost due to the mass cuts was .37 ± .06.

CHAPTER 7

INEFFICIENCY CORRECTIONS

In calculating our cross section we must correct for inefficiencies of the apparatus and of the reconstruction software. We discuss these corrections below and summarize the information in Table 9.

7.A. Gamma Ray Conversions Upstream of the Lead Converter

The loss of events due to gamma rays converting inside the hydrogen target was included in the acceptance calculation. That loss due to conversion along the trajectories towards the converter was calculated independently. The loss was determined by calculating the amount of material traversed by the gamma rays. The greatest contributors to this effect are the spectrometer chambers (aluminum and mylar sheets). From their known collision lengths, the probability of conversion for 2γ events was calculated to be $(9.8 \pm .9)\%$ [2]. Therefore, for 4γ events, it is simply $(18.7 \pm 1.1)\%$.

7.B. Event Rejections by Gamma Hodoscope Trigger

In Chapter 1, we saw that an event trigger occurred

TABLE 9

INEFFICIENCY CORRECTIONS

Correction	Fraction Loss
Gamma ray conversion upstream of lead converter	.187 ± .011
Gamma hodoscope rejection of good event	no losses
Conversion inefficiency of lead converter	.381 ± .063
Gamma software reconstruction failure	.040 ± .028
Digitization scaler runout	no losses
Gamma partial chamber inefficiency	.070 ± .018
Beam contamination	.026 ± .006
Charged pion interaction in detector	.040 ± .014
Counter inefficiency	.032 ± .008
Tight trigger losses	.224 ± .014

CORRECTION FACTOR .316 ± .035

only if at least two "no-yes" combinations were found in the paired gamma hodoscope. This requirement was a potential source of bias because charged particles from the ω decay and backscatters from the lead glass were also seen by GHR. We expected this effect to be quite small as we require four "no-yes" combinations. We investigated this problem in a previous experiment [12] where the same apparatus was used. 25% of the data was then taken with a weaker gamma trigger requiring only one "no-yes" pair. We tightened the trigger with a software cut and found that there were no losses whatsoever.

7.C. Conversion Efficiency of Lead Converter

The gamma conversion efficiency is highly dependent on the effective cutoff energy for observed secondary electrons. However, this cutoff energy is very difficult to measure since it is dependent on the position of the conversion in the lead, and the energy and emission angle of the electron. Therefore, the value for the single gamma efficiency was taken as the average between an upper limit based on pair production predictions, and a lower limit from published Monte Carlo results.

The upper limit was obtained by using the theoretical pair production cross section limiting value [13] of the attenuation coefficient

$$\mu_0 = \frac{7}{9} - \frac{b}{3} \quad ,$$

where b $= [18 \ln(183Z^{-\frac{1}{3}})]^{-1}$ and is equal to -.0069 for lead and -.0224 for aluminium. The factor of b/3 can be ignored as it is negligible in both cases and the conversion efficiency is given by

$$1 - e^{-\mu_0(RL)} = 1 - e^{-\frac{7}{9}(3.38)} = 92.8\% \quad .$$

The lower limit was obtained from published Monte Carlo results for photon showers by Messel and Crawford [14]. The secondary cutoff energy for our detector lies somewhere below 10 MeV [2] . From the shower tables an average value of 84.6% is predicted for our energy range. We believe the parameters of our system lie between the two extremes. Therefore the average was taken, (88.7 ± 4.5)%, with a systematic error covering the two limits. By raising this result to the fourth power, we obtain the 4γ efficiency, (.619 ± .063).

7.D. Gamma Software Reconstruction Failure

The software reconstruction inefficiency was measured by hand-scanning 1000 2γ events on a CRT display by means of an interactive program that permitted operator determination of gamma showers. The result for the 2γ events was an inefficiency of $(2 \pm 2)\%$. For 4γ events, the inefficiency is simply $(4.0 \pm 2.8)\%$.

7.E. Digitization Scaler Runout

We studied the possibility of losing a real gamma shower due to an insufficient number of scalers. We did not expect the effect to be substantial as the first X and Y planes were instrumented with 12 scalers and all other planes with 16 scalers. The method employed is quite simple. The spark positions for each X and Y plane were read, starting at the positive X and positive Y ends, respectively. Therefore, a scaler runout would result in a depletion of the negative X and Y positions, in contrast to the expected symmetry about the origin in the normal 100% efficient case. We studied only the Y plane, as the X plane is not expected to be symmetric due to the 2.5 degree angle between the spectrometer Z-axis and the target Z-axis. We plotted the Y position of 100,000 showers and determined that there was no depletion of showers in the negative Y region. Therefore, as expected, the correction for this effect is negligible.

7.F. Partial Gamma Detector Inefficiency

This is a time dependent correction that was handled by the reconstruction software. The participation of each gamma chamber plane in each event was continuously monitored and recorded. At the end of a run, the efficiency of each chamber and the single gamma efficiency were calculated from the individual participation ratios using the procedure described in Appendix D. However, these figures were calculated for 2γ events only, since the largest fraction of our data was 2γ events.

For 4γ events, the efficiency is expected to be lower because the same charge is distributed among more sparks. Separate single gamma efficiencies for events with three or more gammas were not calculated by the software. We studied this problem and determined the efficiency for the final $\omega\pi^{o}$ event sample of Figure 18 using the same method described in Appendix D. The single gamma efficiency for these events was $.974 \pm .010$. Therefore, the net efficiency for the $\omega\pi^{o}$ events was $.900 \pm .018$. The single gamma efficiency for all 2γ events ($.986 \pm .002$) is already taken into account in the effective beam flux (a factor of $.972 \pm .004$ for two gammas), and thus, the effective correction factor to be used is $.930 \pm .018$.

7.G. Partial Charged Spectrometer Inefficiency

Again this is a time dependent correction which was handled by the reconstruction software. This factor was taken into account by the "offline" software in the calculation of the effective beam.

7.H. Beam Contamination

The muon content in the beam was found to be (2.0 ± .6)% at 8.45 GeV/c by measuring the amount of beam that traversed three feet of steel. Kaon contamination was estimated at .6% (published yield curves [16]) and electron contamination should be negligible (severe phase space restrictions).

7.I. Charged Pion Interaction in Detector

From the known cross sections of mylar, aluminum, etc., an attenuation of (2 ± 1)% is determined for an incident pion. Thus, the probability of losing one or both pions is (4.0 ± 1.4)%.

7.J. Event Rejections by Trigger

As mentioned in Chapter 1, our trigger demanded that two or three H2 scintillator elements be hit and no TA elements be set. To permit offline investigation of the effects of these constraints, we collected, in a previous experiment [12] using the same apparatus, aproximately 20% of the data under a "loose" trigger which demanded H2 > 1 and allowed one TA to be set. Subsequent investigations with software showed that our tight H2 constraints caused an (8.1 ± .5)% loss, and tightening our TA requirements caused a further (15.6 ± 1.4)% loss. Investigation of other reactions by members of our collaboration have shown the TA loss to be t-dependent [17] . However, owing to our poor statistics, we use a constant correction with systematic error covering all t-dependent fluctuations.

The product of these two factors gives a correction of .776 ± .014.

7.K. Miscellaneous Corrections

Losses due to scintillation counter inefficiencies (cracks, etc.) were calculated to be (3.2 ± .8)%. This was determined by interactive scanning of 1000 events on a CRT. The target was surrounded by a half-inch layer of polyethylene to stop low energy particles. Therefore, we can ignore losses due to δ ray creation inside the target.

7.L. Summary

The event loss fractions caused by the inefficiencies described in this chapter are listed in Table 9. The final overall correction factor is $.316 \pm .035$.

CHAPTER 8

THE $B^o \rightarrow \omega\pi^o$ DIFFERENTIAL CROSS SECTION

As already mentioned, Chapter 10 presents the results of a sequential decay analysis in which we found that 24% of our data consists of a $J^P = 1^-$ state. We feel that this is the $\rho'(1250)$ resonance. Since this analysis was performed in only 2 t' bins (owing to poor statistics), we cannot separate the 1^- component from the 1^+ component in a calculation of the differential cross section in finer bins. Therefore, what we present here is the differential cross section of $B^o \rightarrow \omega\pi^o$ with the $J^P = 1^-$ state treated as background, and accordingly removed. Spin projected cross sections, $\rho_{ij}\, d\sigma/dt$, for each t' bin and both J^P states are given in Chapter 10 for the s-channel helicity frame.

The differential cross section was calculated using the following expression:

$$\frac{d\sigma}{dt'} = \frac{Y(t') \times 10^{30}}{\beta \times N \times \varepsilon \times \Delta t' \times A(t')}\ \mu b/(GeV/c)^2 \qquad (8\text{-}1)$$

where $Y(t')$ = yield of good events in each t' bin,

β = total effective beam flux,

N = number of protons in hydrogen target / cm^2,

ε = constant correction factor,

$\Delta t'$ = t' interval ($t' = t - t_{min}$, where the average t_{min} at our energy is ~.009 GeV^2)

and $A(t')$ = acceptance in each t' bin.

The constant correction factor (ε) is the product of the correction factor due to mass cuts (Table 8) and that due to inefficiency corrections (Table 9). We correct the total beam flux for spectrometer and gamma chamber inefficiencies, and for losses due to the presence of dual beam tracks in certain events. The result is the effective beam flux, and it is this number (β) we use in the $d\sigma/dt'$ calculations.

The differential cross section for reaction (6-2) is presented in Figure 24 and listed in Table 10. The error bars are only statistical errors and do not include an overall normalization (systematic) error of 15%. The integrated cross section is 7.7 ± 1.2 μb . The differential distribution was obtained by fitting the $\omega\pi^o$ mass plots at various t' slices. However mass and width for both the B^o and $\rho'(1250)$ were fixed to the values obtained from the total fit. The background subtractions for the smaller t bins used for the differential cross section were obtained by interpolating between these fitted points. The fractions of good events per t' bin, as determined by the above fits, are summarized in Table 11. The 1^- fraction is corrected for as determined in the 2 t' bin fit in Chapter 10 (i.e., 38% for $t' < .13$ and 8% for $.13 < t' < .57$).

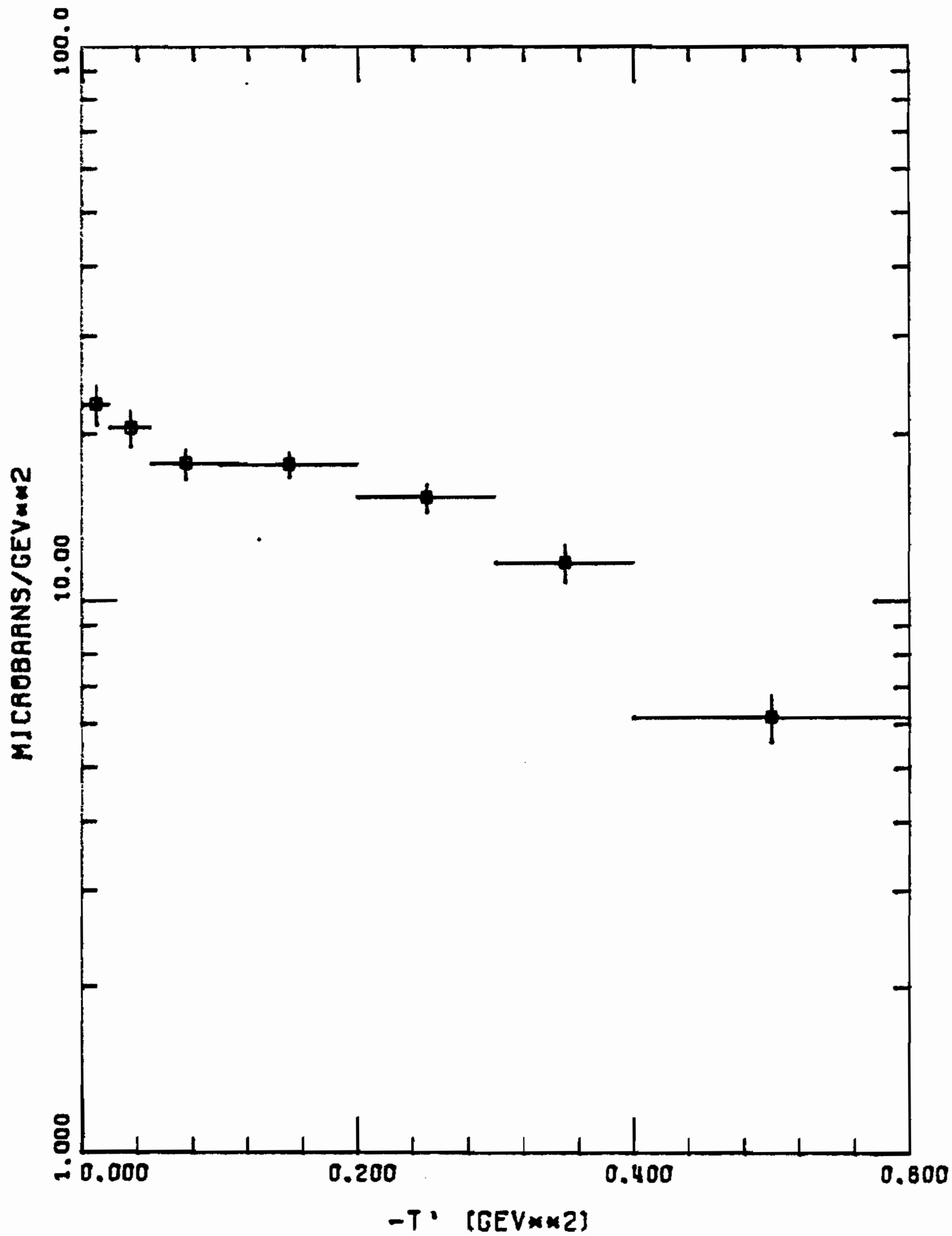

FIGURE 24 Differential Cross Section

TABLE 10

$B^o \rightarrow \omega\pi^o$ DIFFERENTIAL CROSS SECTION

t' Bin	Δt'	Y(t')	A(t')	dσ/dt (μb/GeV²)	Statistical Error
.00-.02	.02	95.3	.047	22.6	1.6
.02-.05	.03	124.5	.045	20.5	1.3
.05-.10	.05	174.9	.044	17.7	.9
.10-.20	.10	317.9	.040	17.6	.8
.20-.30	.10	243.2	.035	15.4	.8
.30-.40	.10	162.8	.031	11.7	.8
.40-.60	.20	137.7	.025	6.2	.5

TABLE 11

GOOD EVENT PERCENTAGES

t' Range	Fraction of Good Events
.00-.05	.098 ± .050
.05-.10	.163 ± .050
.10-.20	.152 ± .050
.20-.30	.102 ± .050
.30-.60	.135 ± .050

CHAPTER 9

DETERMINATION OF THE PRODUCTION AND DECAY PARAMETERS OF THE $\omega\pi$ SYSTEM

This chapter describes the technique used in the determination of the Density Matrix Elements (D.M.E.'s) of the $(\omega\pi)$ system and of the D/S ratio for the B^o decay. We adopt the sequential decay method used by Chung [5] in a spin and parity analysis of charged B data. The formalism is described in Appendix E and is summarized here.

9.A. Angular Distributions

The decay amplitude of an $\omega\pi$ resonance of spin J and helicity Λ can be parameterized in terms of the ω helicity amplitudes $F_\lambda(\lambda=0,\pm1)$ as

$$M \propto \sum_\lambda F^*_\lambda D^{J*}_{\Lambda\lambda}(\Phi,\Theta,0)\, D^{1*}_{\lambda 0}(\phi,\theta,0) \qquad (9\text{-}1)$$

with normalization

$$\sum_\lambda |F_\lambda|^2 = 1 \quad . \qquad (9\text{-}2)$$

The polar and azimuthal angles of the ω in the B^o rest frame are Θ and Φ, respectively (see Figure 25). For the z-axis,

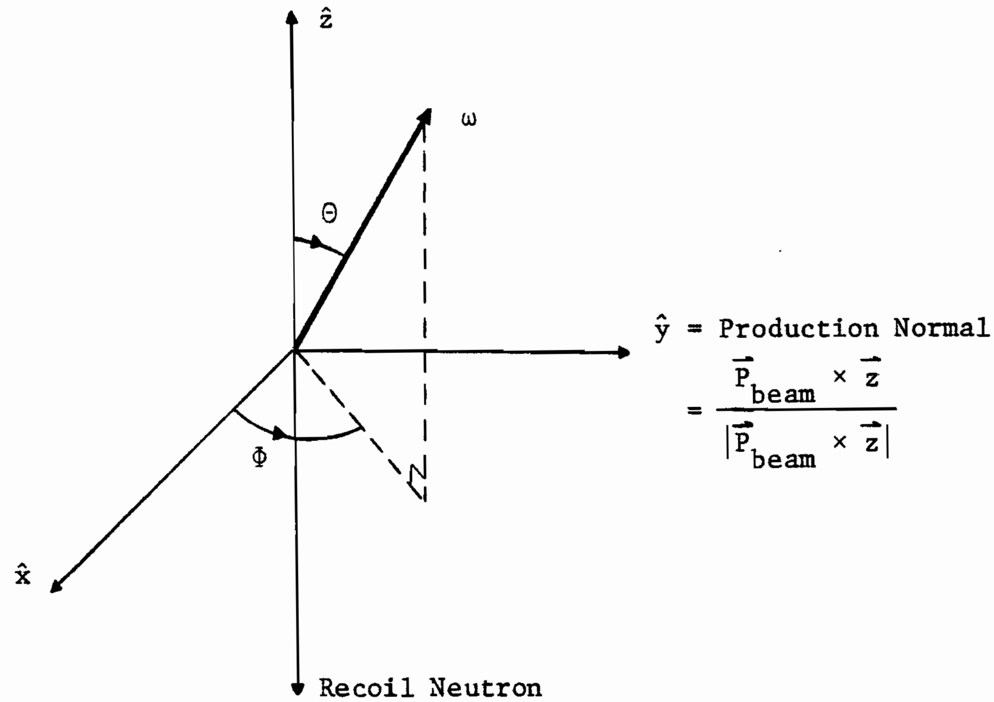

FIGURE 25a B^{o} Helicity Rest Frame

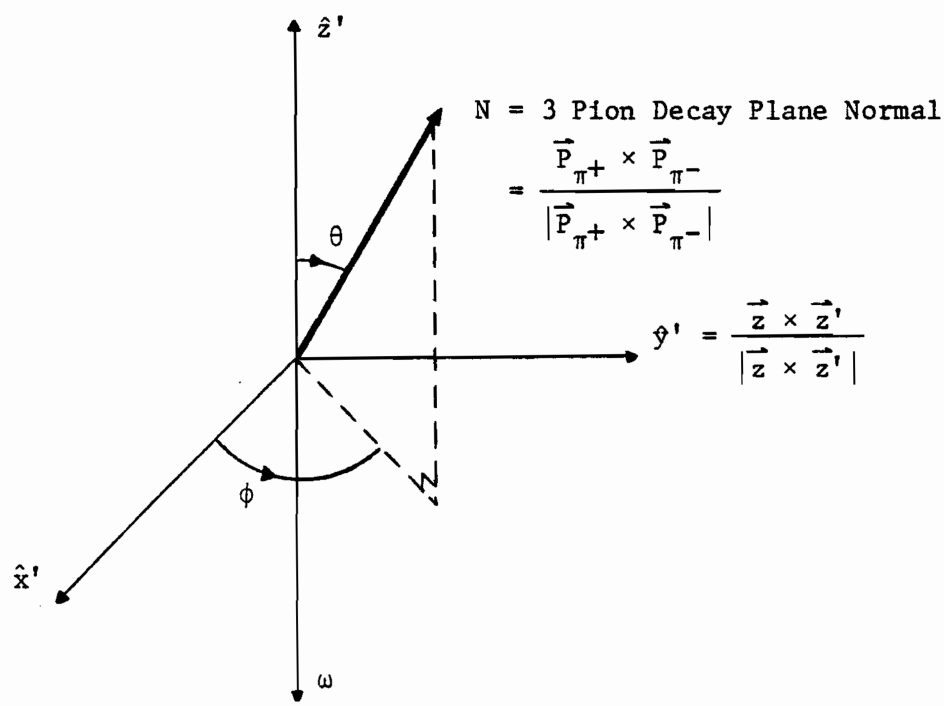

FIGURE 25b ω Helicity Rest Frame

we choose the momentum of the resonance (i.e., in our case, the B^o) in the overall C.M. system (i.e., s-channel helicity frame). The y-axis is normal to the production plane, defined as $(\bar{p}_{in} \times \bar{B}^o)$. The angles θ and ϕ define the direction of the normal to the ω decay plane and are measured in the coordinate system obtained from the system (x,y,z) in the B^o rest frame by a rotation with Euler angles $\alpha = \Phi$, $\beta = \Theta$ and $\gamma = 0$, and a boost to the ω rest frame.

From (9-1), the decay probability

$$\frac{d^4N}{d\cos\Theta d\cos\theta d\Phi d\phi}$$

follows directly (see Appendix E). We then obtain

$$\frac{d^4N}{d\cos\Theta d\cos\theta d\Phi d\phi} = \frac{3(2J+1)}{16\pi^2} \sum_{\substack{L\Lambda\Lambda' \\ \lambda\lambda'}} (-1)^{\Lambda} \rho^{J}_{\Lambda\Lambda'} F^J_{\lambda} F^{J*}_{\lambda'} \tag{9-3}$$

$$(J,-\Lambda,J,\Lambda'|L,\Lambda'-\Lambda)(J,-\lambda,J,\lambda'|L,\lambda'-\lambda)$$

$$D^L_{\Lambda'-\Lambda,\lambda'-\lambda}(\Phi,\Theta,\phi)\, d^1_{-\lambda 0}(\theta)\, d^1_{\lambda' 0}(\theta) \quad ,$$

where $L = 0,\ldots,2J$,

$\Lambda = \pm J, \pm(J-1),\ldots,0$

and $\lambda = \pm 1, 0$.

All other symbols are defined in Appendix E.

The ω width is neglected in (9-2); the $\rho^J_{\Lambda\Lambda'}$ are the density matrix elements of the resonance with spin J. Parity conservation in the decay $J \to \omega\pi$ implies $F_\lambda = \varepsilon F_{-\lambda}$, where $\varepsilon = -\eta(-1)^J$ and η is parity of the resonance. Together with the F_λ normalization condition (9-2), this yields the following results:

a) $J^P = 1^+$

$$F_\lambda = F_{-\lambda} \; .$$

b) $J^P = 1^-$ (9-4)

$$F_\lambda = -F_{-\lambda}$$

and therefore, $F_1 = -F_{-1}$ and $|F_1|^2 = |F_{-1}|^2 = \frac{1}{2}$

and $F_0 = 0$.

The relative amounts of D-wave (l=2) and S-wave (l=0) in the $B^o \to \omega\pi$ decay can easily be related to the values of the ω helicity amplitudes, F_λ, by use of the relation

$$F_\lambda = \sum_l \left(\frac{2l + 1}{2J + 1}\right)^{\frac{1}{2}} \langle J\lambda|l0s\lambda\rangle \; K_l \quad ,$$

where s = 1, where $K_0 \equiv$ S-wave and $K_2 \equiv$ D-wave. Therefore, we get the following amplitudes:

$$D = \sqrt{2/3}\;(-F_0 + F_1)$$

and

$$S = \sqrt{1/3}\;(F_0 + 2F_1) \quad .$$

The absence of any D-wave signal implies

$$F_1 = F_0 = 1/\sqrt{3} \quad . \tag{9-5}$$

The angular distribution of the products of the sequential decay $J^P \to \omega\pi$, $\omega \to \pi^+\pi^-\pi^o$ is given by (9-3). We have evaluated this expression for $J^P = 1^+$ (E-10) and $J^P = 1^-$ (E-12) in Appendix E.

For $J^P = 1^+$, we have five free parameters to be determined. Due to hermiticity, normalization, conservation of parity and the choice of the helicity frame, we have only three independent D.M.E. parameters (see Appendix E). They are ρ_{00}, ρ_{1-1} and $Re[\rho_{10}]$. Equations (9-2) and (9-4) imply that we need only one ω helicity amplitude, F_0 (except for the interference term $Re[F_0F_1^*]$). We have found that it is not necessary to include a phase between F_0 and F_1 ; no significant improvement in the fit results from varying the phase. Therefore, $Re[F_0F_1^*]$ is set equal to $F_0\{(1-F_0^2)/2\}^{\frac{1}{2}}$. The fifth and final parameter is $N(1^+)$, a normalizing factor (which is in fact the unnormalized cross section for the 1^+ wave).

In the case of the 1^- wave, there are only four parameters since

$$F_1 = F_{-1} = 1/\sqrt{2} \ . \tag{9-4}$$

These parameters are $N(1^-)$, ρ_{00}, ρ_{1-1} and $Re[\rho_{10}]$.

9.B. Acceptance Corrections to the Angular Distributions

Since our detector did not have 100% acceptance, we must correct the theoretical angular distributions before we can fit them to the data. This was done as follows: rather than fitting expression (9-3), we actually fitted the angular distributions of a single angle (i.e., $dN/d\cos\Theta$, $dN/d\Phi$, etc.). These were determined by numerically integrating (9-3) with respect to three of the four angles. By folding our acceptance into the integral, we obtained the acceptance-corrected distributions, $dN/d\cos\Theta$, $dN/d\cos\theta$, etc.

Given that

$$\left(\frac{d^4N}{d\cos\Theta d\cos\theta d\Phi d\phi}\right)_{100\%\ \text{acceptance}} = f(\Theta,\Phi,\theta,\phi) \ ,$$

we have

$$\left(\frac{dN}{d\cos\Theta}\right)_{\substack{\text{corrected}\\ \text{for acceptance}}} = \int_0^{2\pi}\int_0^{2\pi}\int_{-1}^{1} A_\Theta(\Phi,\theta,\phi) \, f(\Theta,\Phi,\theta,\phi)\, d\cos\theta\, d\phi\, d\Phi \quad . \tag{9-6}$$

where $A_\Theta(\Phi,\theta,\phi)$ is the function denoting our acceptance for a particular Θ bin as a function of the other three angles. It is assumed that the $\cos\Theta$ bins are small, so that $A_\Theta(\Phi,\theta,\phi)$ is not a function of Θ.

The numerical integrals were calculated by Monte Carlo integration [25,31]. The technique is quite simple and is summarized here.

Consider the integral of a function f(x)

$$I = \int_b^a f(x)dx \quad . \tag{9-7}$$

The mean value of f(x) in the interval [a,b] is

$$\frac{I}{b - a} \quad . \tag{9-8}$$

If we choose n points, x_i, $i = 1,\ldots,n$, at random in [a,b] and then sample the value of $f(x_i)$ at these points, the average value is

$$\hat{f}_n = \frac{1}{n} \sum_{i=1}^{n} f(x_i) \quad .$$

From (9-8), we expect

$$\hat{f}_n \simeq I/(b - a)$$

and therefore, using (9-7),

$$I \simeq \frac{b - a}{n} \sum_{i=1}^{n} f(x_i) \quad .$$

The $\cos\Theta$ distribution (9-6) can now be rewritten as

$$\frac{dN}{d\cos\Theta} = \frac{8\pi^2}{n} \sum_{i=1}^{n} f(\Theta, \Phi_i, \theta_i, \phi_i) \quad .$$

The points Φ_i, θ_i and ϕ_i are generated by our Monte Carlo program for a fixed $\cos\Theta$ bin. The event is only summed if it passes our geometric acceptance. In this way, we can fold our acceptance into the angular distributions.

The variance in the error of the calculation of the integral I of the function f(x) in the interval [a,b] is given by

$$\sigma^2 = \frac{1}{b - a} \int_a^b f^2(x)\,dx - \left[\frac{1}{b - a} \int_a^b f(x)\,dx \right]^2 \quad .$$

The Central Limit Theorem implies that the probability of the error being less than $\lambda\sigma/\sqrt{n}$ is

$$\text{prob}\left[\left| \underbrace{\frac{b - a}{n} \sum_{i=1}^{n} f(x_i)}_{\text{experimental}} - \underbrace{I}_{\text{true}} \right| \le \frac{\lambda\sigma}{\sqrt{n}} \right] = \frac{1}{2\pi} \int_{-\lambda}^{\lambda} e^{-x^2/2\sigma^2}\,dx \quad .$$

For one standard deviation ($\lambda = 1$), there is a 68.3% probability that the error is less than $\sigma/\sqrt{n}$. Note that for a fixed level of confidence, one must quadruple the sample in order to halve the error. We found that all integrals converged to 2 or 3 decimal points after 10^6 events were generated (this corresponds to an average of 40,000 events passing our acceptance cuts).

9.C. Fitting the Data

Acceptance-corrected expressions for $dN/d\cos\Theta$, $dN/d\cos\theta$, $dN/d\Phi$ and $dN/d\phi$ were calculated for both $J^P = 1^+$ and $J^P = 1^-$. The 1^+, 1^- and a background wave were then incoherently added and fitted to the experimental distributions. The background was simply a flat distribution "modulated" by acceptance to account for incorrect combinations. All four angular distributions were fit simultaneously.

To summarize, we fitted the acceptance-corrected theoretical distributions

$$\sum_{1^+1^-\mathrm{BKGD}} \frac{dN}{d\cos\Theta}, \quad \sum_{1^+1^-\mathrm{BKGD}} \frac{dN}{d\cos\theta}, \quad \sum_{1^+1^-\mathrm{BKGD}} \frac{dN}{d\phi}, \quad \sum_{1^+1^-\mathrm{BKGD}} \frac{dN}{d\Phi}$$

to the experimental distributions

$$\frac{dN_{expt}}{d\cos\Theta}, \quad \frac{dN_{expt}}{d\cos\theta}, \quad \frac{dN_{expt}}{d\phi}, \quad \frac{dN_{expt}}{d\Phi}$$

to determine the parameters $N(1^+)$, $\rho_{00}^{1^+}$, $\rho_{1-1}^{1^+}$, $Re[\rho_{10}^{1^+}]$, F_0, $N(1^-)$, $\rho_{00}^{1^-}$, $\rho_{1-1}^{1^-}$, $Re[\rho_{10}^{1^-}]$ and N(BKGD). Each one of the distributions is divided into 12 bins. Note that the density matrix must be positive definite. Accordingly, we must apply the constraints

$$a) \qquad 0 < \rho_{mn} < 1$$

and

$$b) \qquad |\rho_{mn}| \leq \sqrt{\rho_{mm}\rho_{nn}}$$

to the density matrix elements.

All fitting was done by means of the CERN/MINUIT [9] program and the constraints were applied by constructing a so-called barrier function which "penalizes" the fitting algorithm by drastically increasing the value of the function to be optimized as the constraint boundaries are approached.

The data was alternately divided into 2 mass and 2 t' bins. The fitting procedure described above was applied to each bin. The resulting fits are given in Figures 26 to 29. The results are given and discussed in Chapter 10.

The use of wide mass and t' bins should cause large incoherence effects. This, plus the fact that the angular distributions (corrected for acceptance) do not exhibit significant asymmetric effects, justifies the use of an incoherent model.

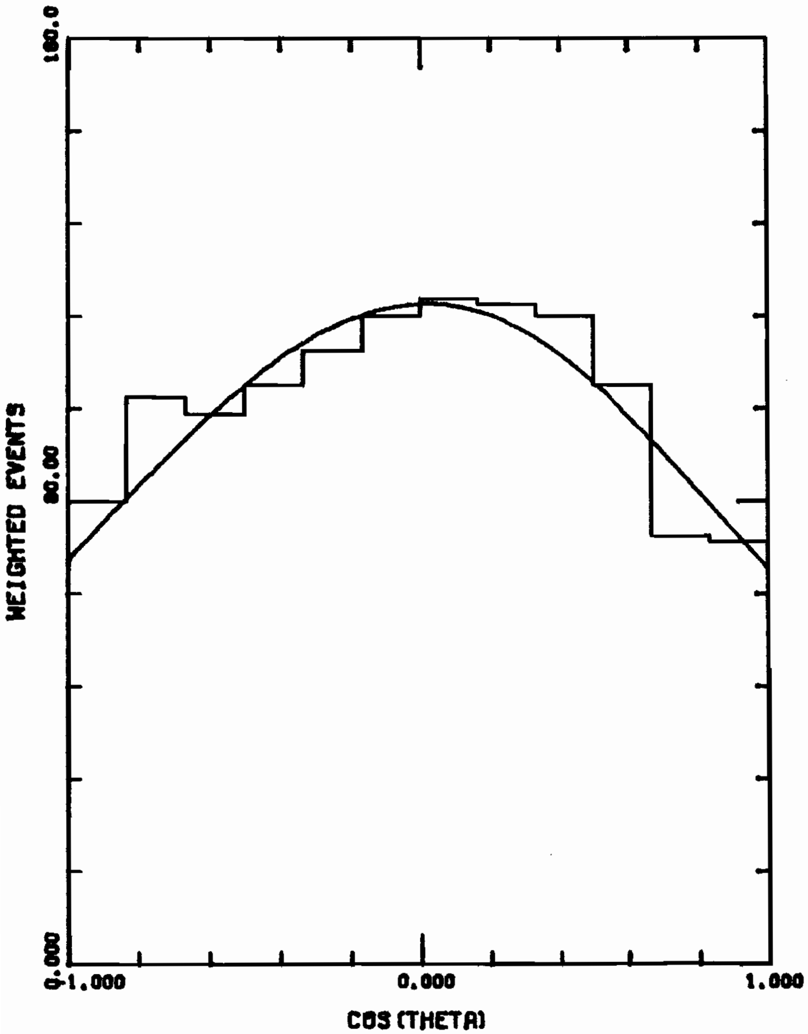

FIGURE 26a t'-bin Analysis (.00-.13)GeV^2 cosθ

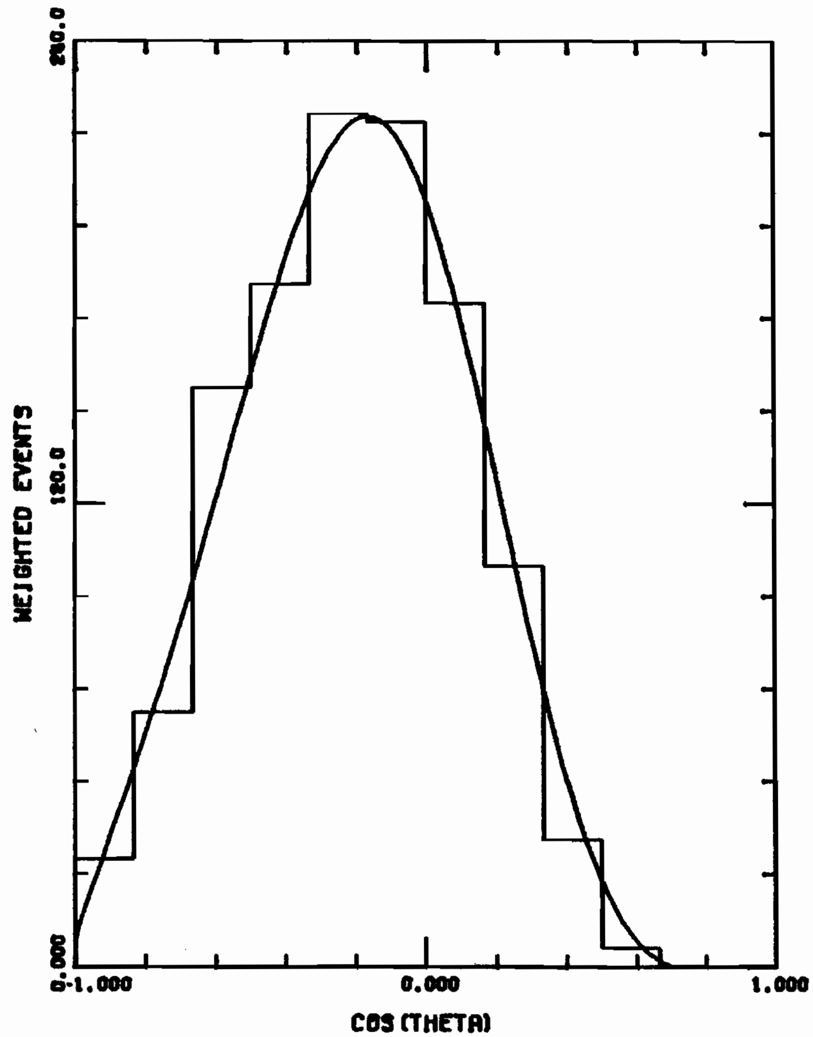

FIGURE 26b t'-bin Analysis (.00-.13)GeV^2 cosΘ

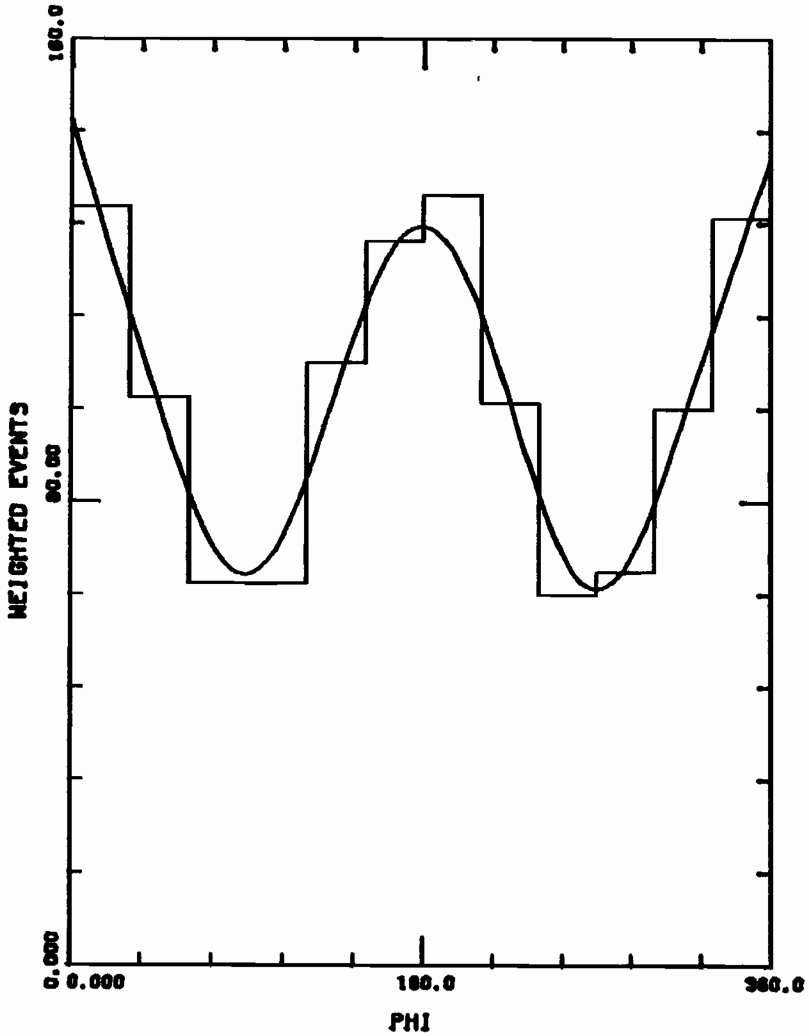

FIGURE 26c t'-bin Analysis (.00-.13)GeV^2 ϕ

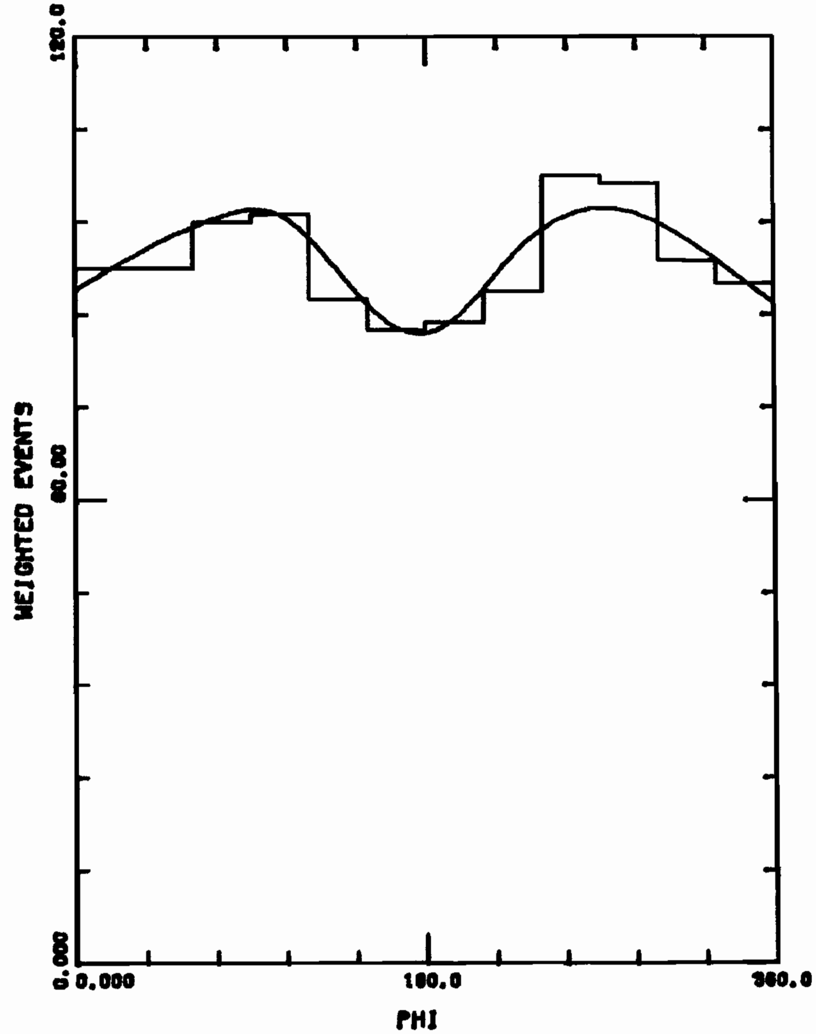

FIGURE 26d t'bin Analysis (.00-.13)GeV^2 Φ

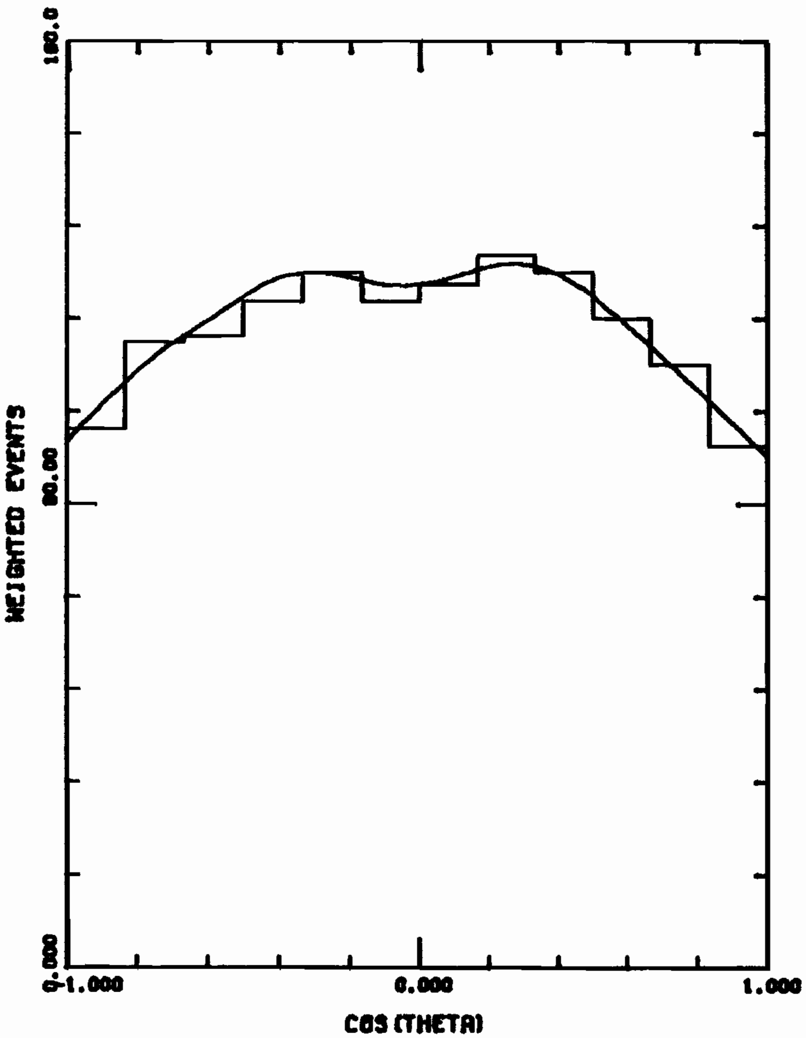

FIGURE 27a t'-bin Analysis (.13-.57)GeV^2 cosθ

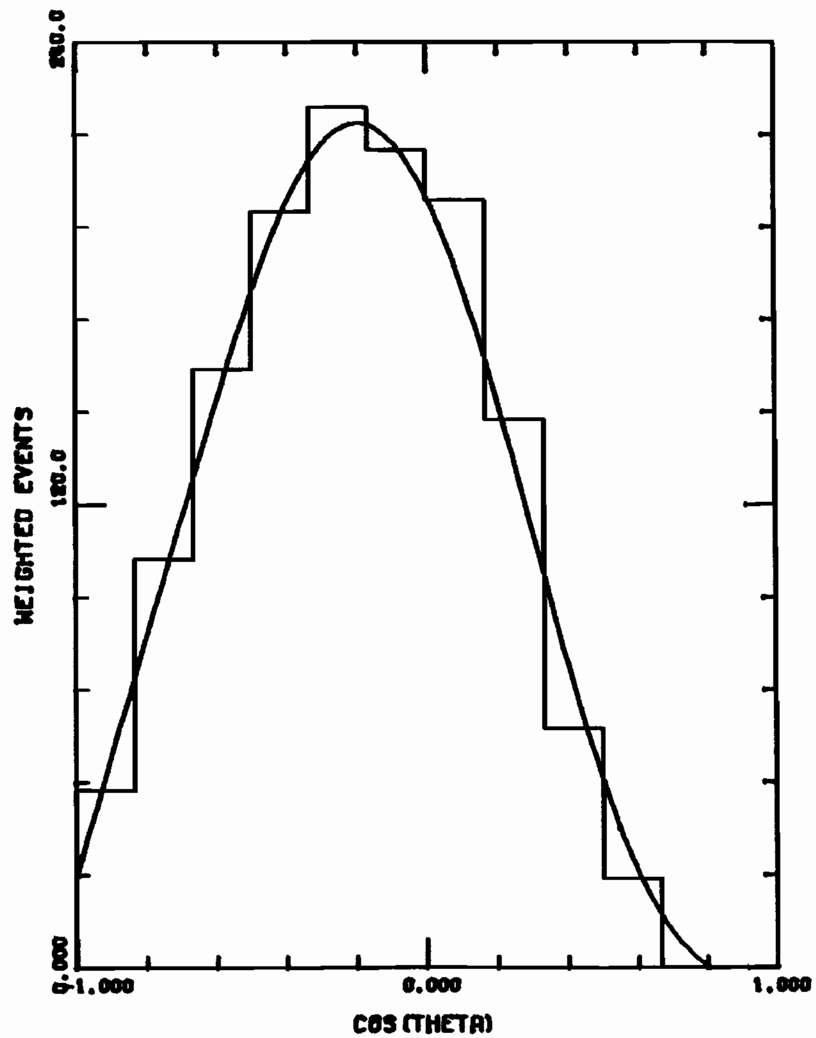

FIGURE 27b t'-bin Analysis (.13-.57)GeV^2 cosθ

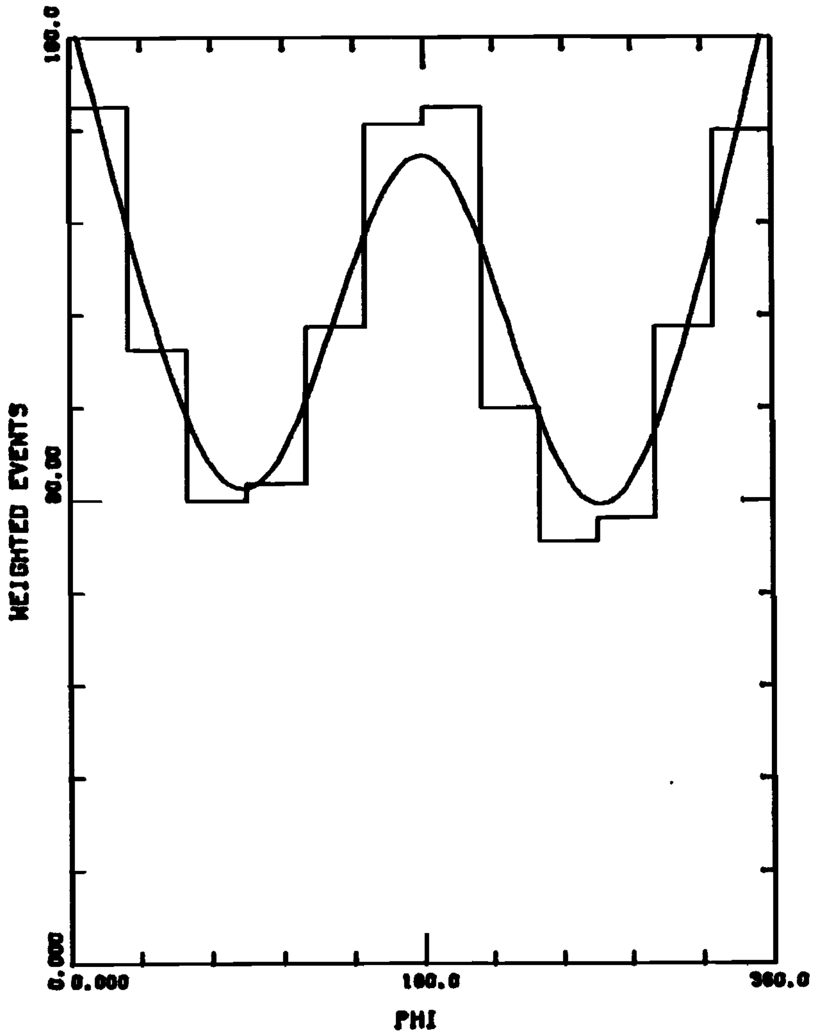

FIGURE 27c t'-bin Analysis (.13-.57)GeV^2 ϕ

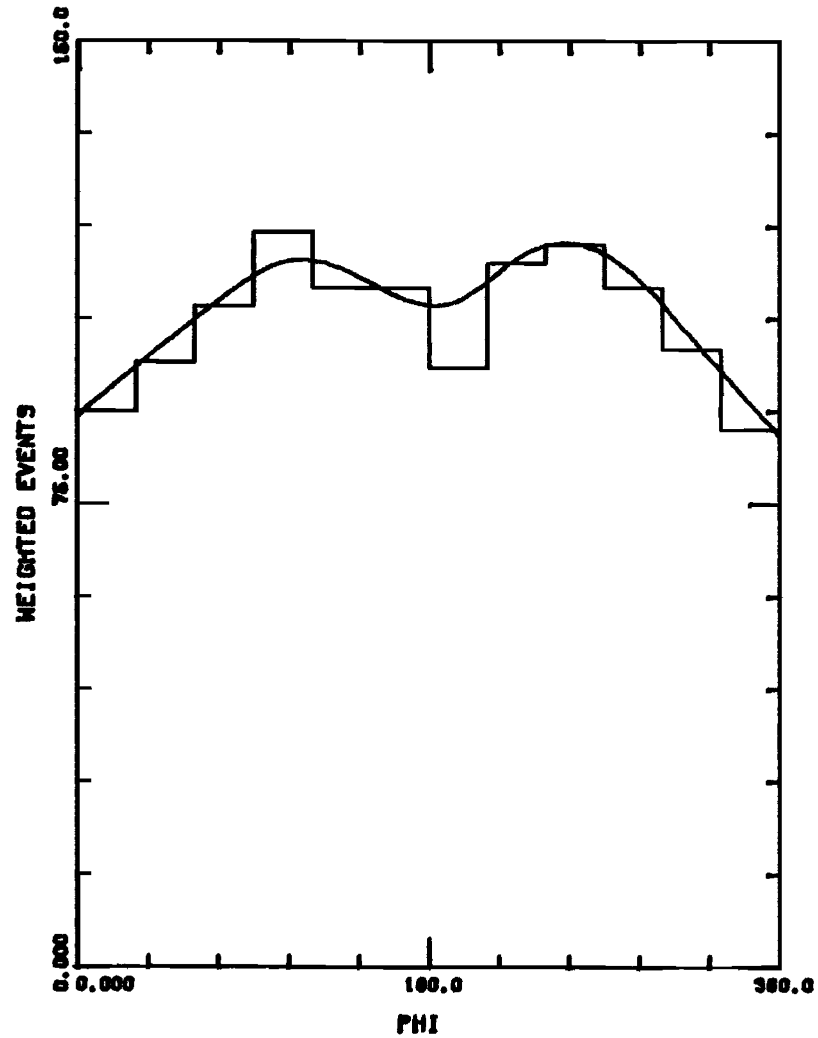

FIGURE 27d t'-bin Analysis (.13-.57)GeV^2 Φ

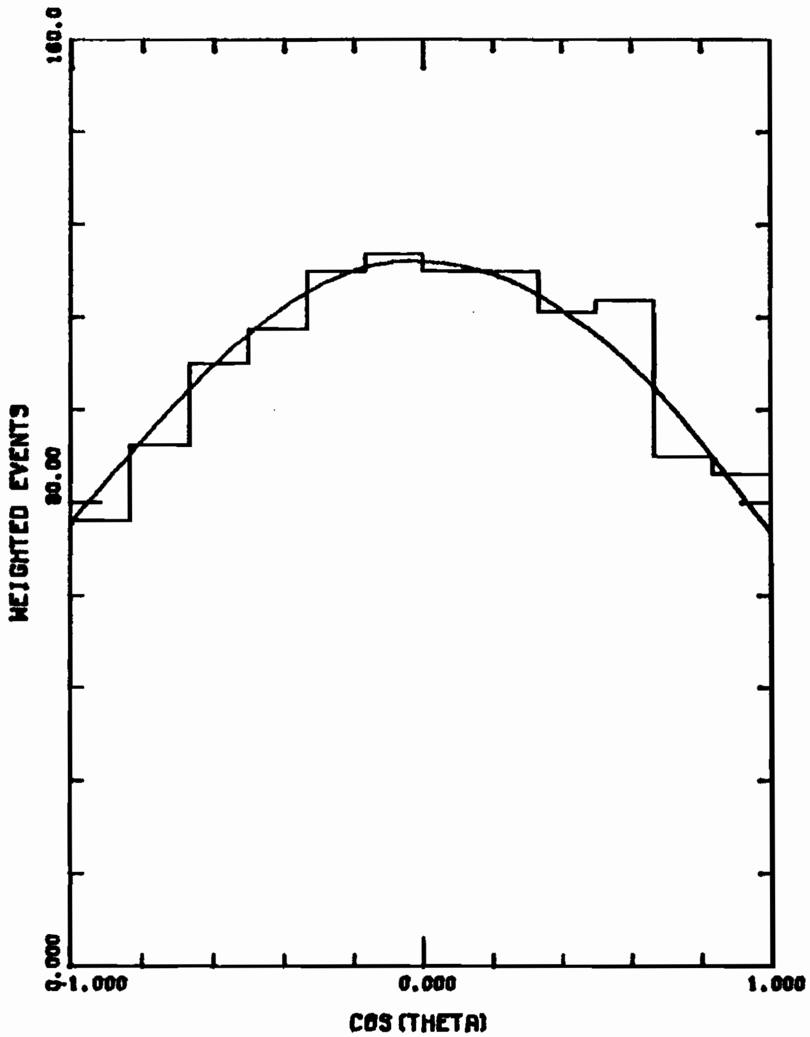

FIGURE 28a Mass Bin Analysis (1.08-1.23)GeV cosθ

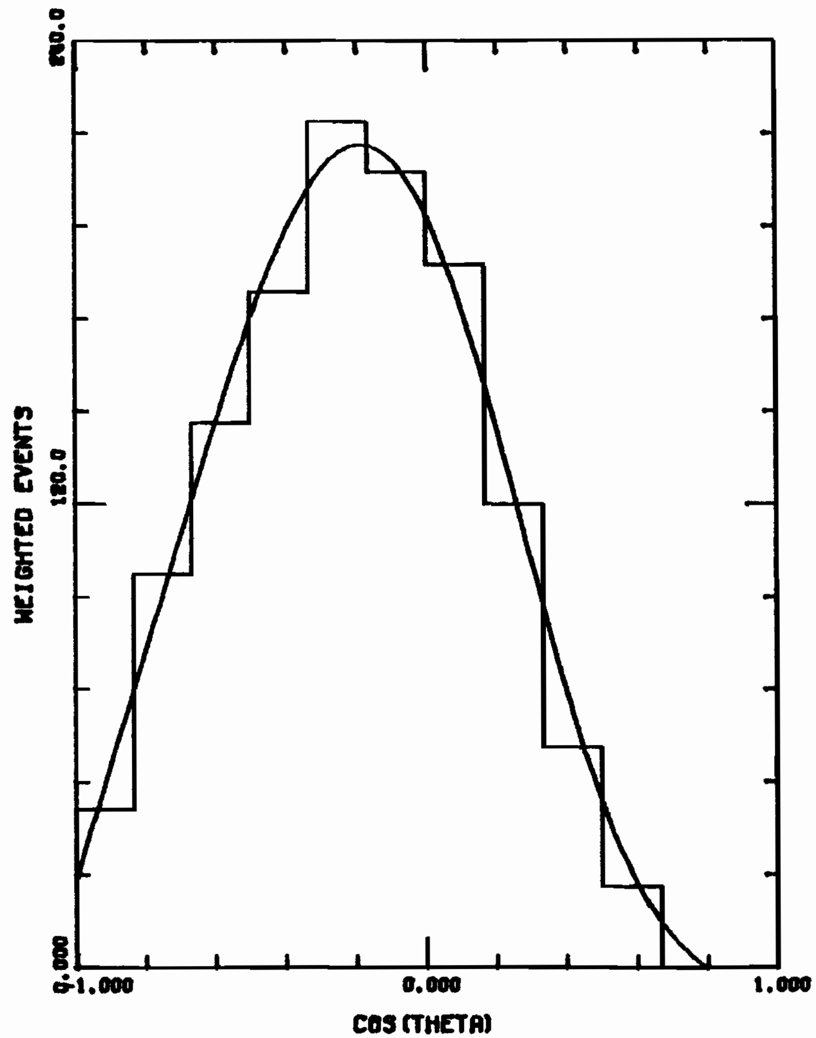

FIGURE 28b Mass Bin Analysis (1.08-1.23)GeV cosΘ

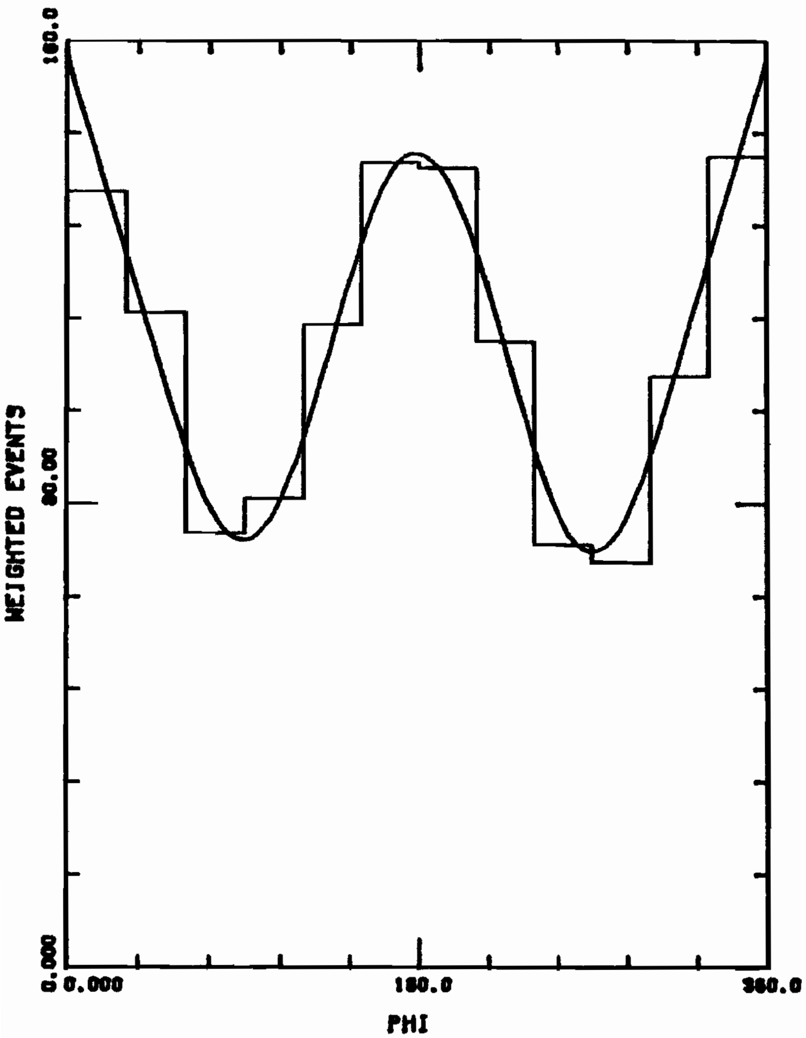

FIGURE 28c Mass Bin Analysis (1.08-1.23)GeV ϕ

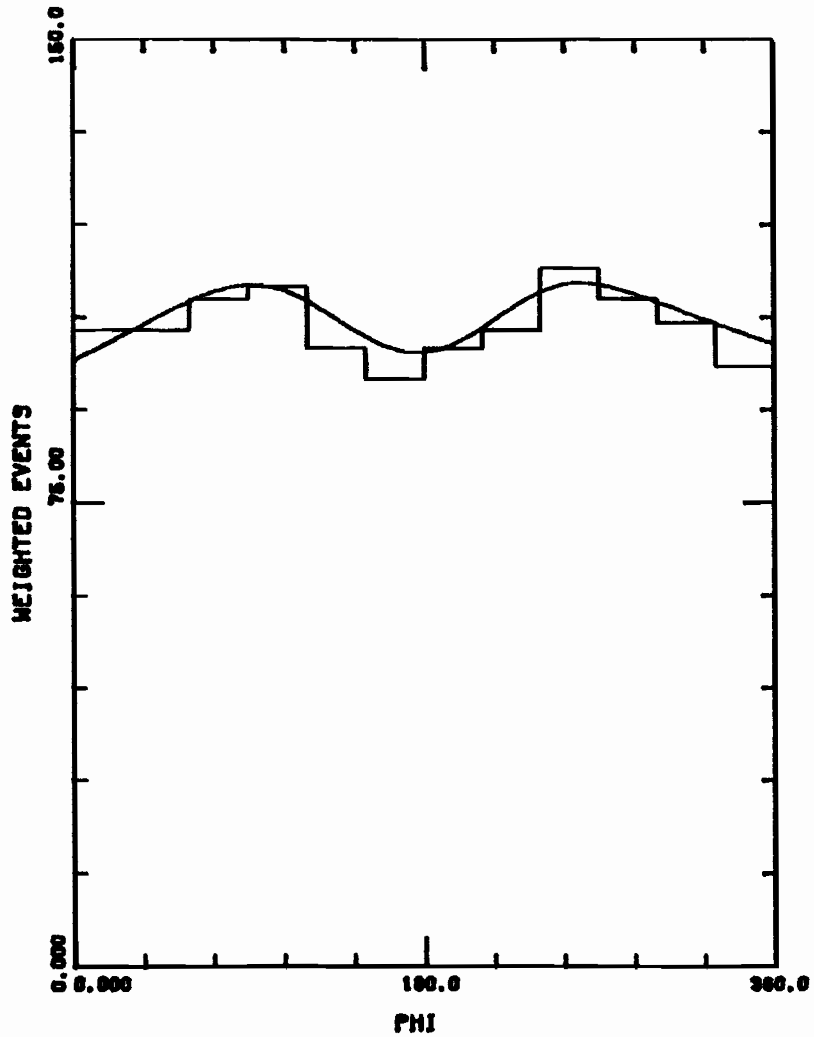

FIGURE 28d Mass Bin Analysis (1.08-1.23)GeV Φ

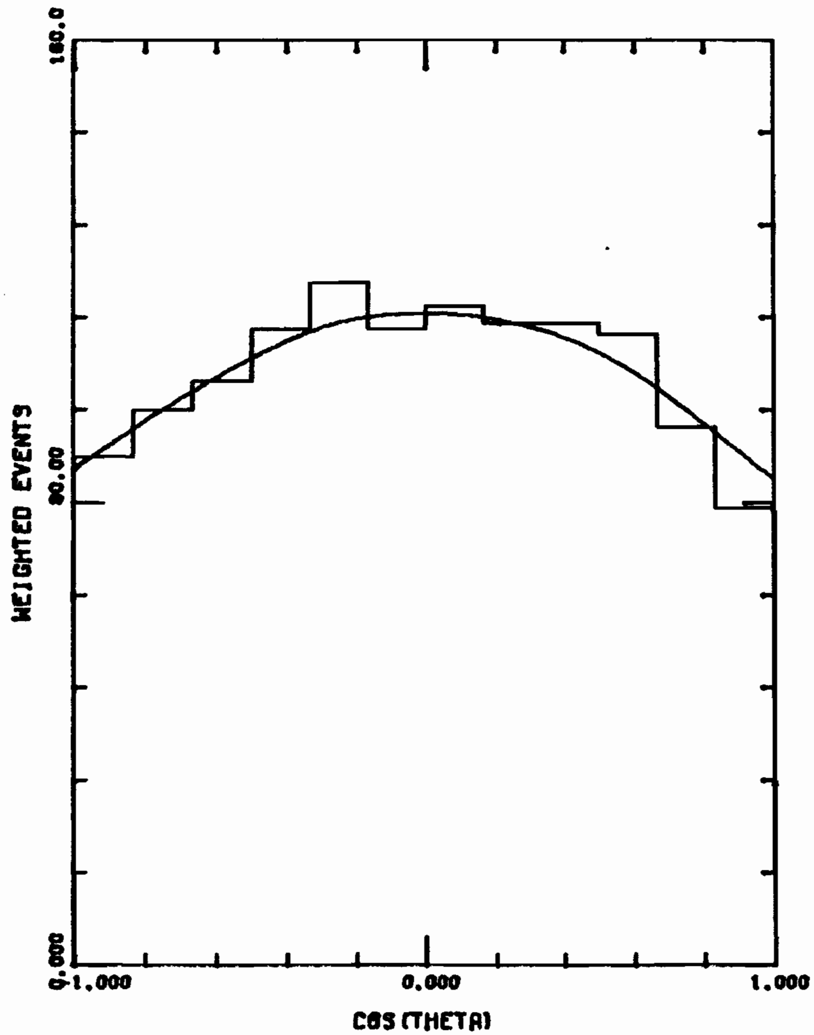

FIGURE 29a Mass Bin Analysis (1.23-1.38)GeV cosθ

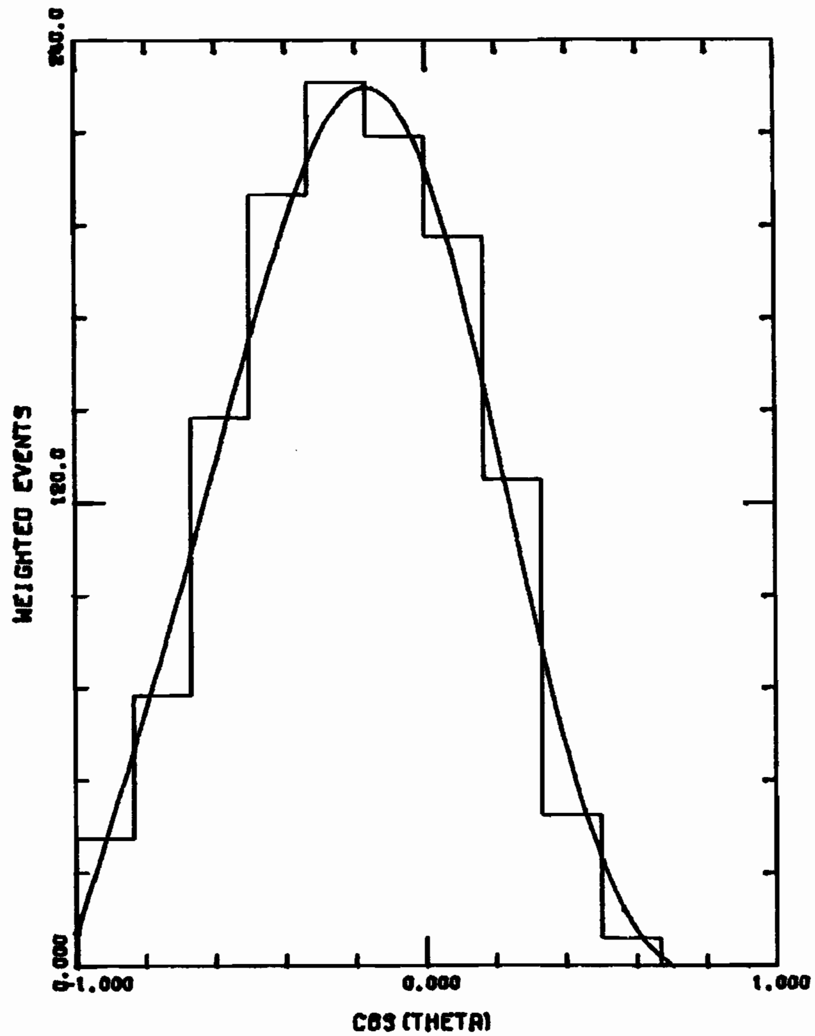

FIGURE 29b Mass Bin Analysis (1.23-1.38)GeV cosθ

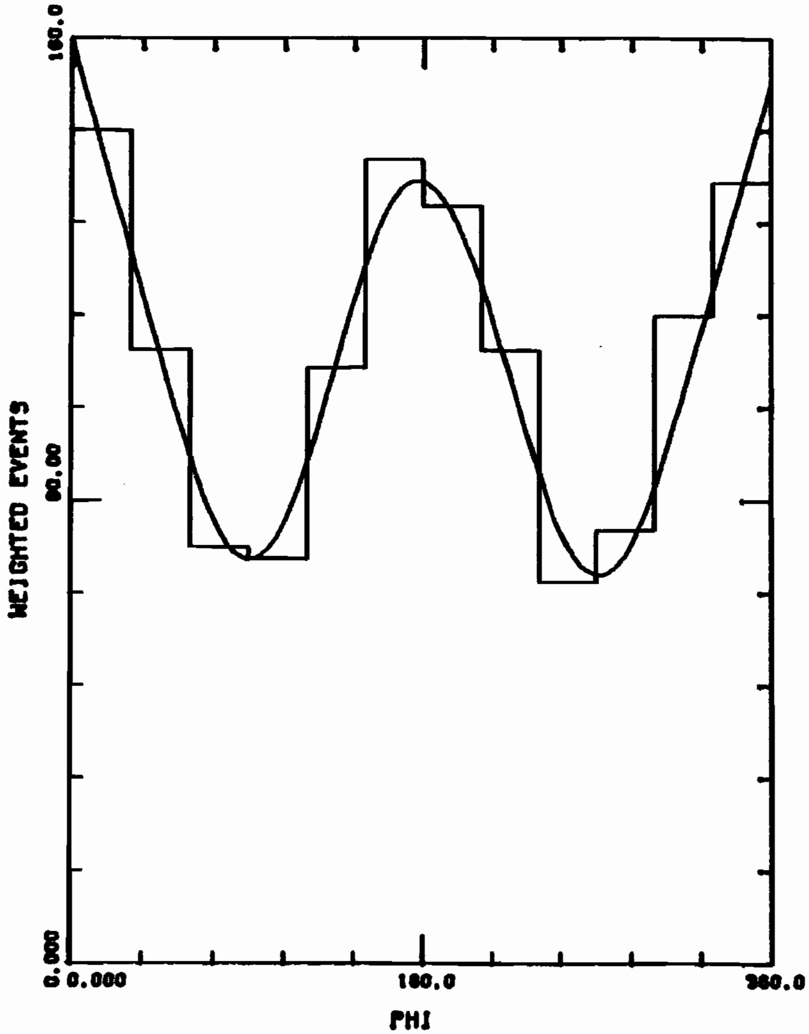

FIGURE 29c Mass Bin Analysis (1.23-1.38)GeV ϕ

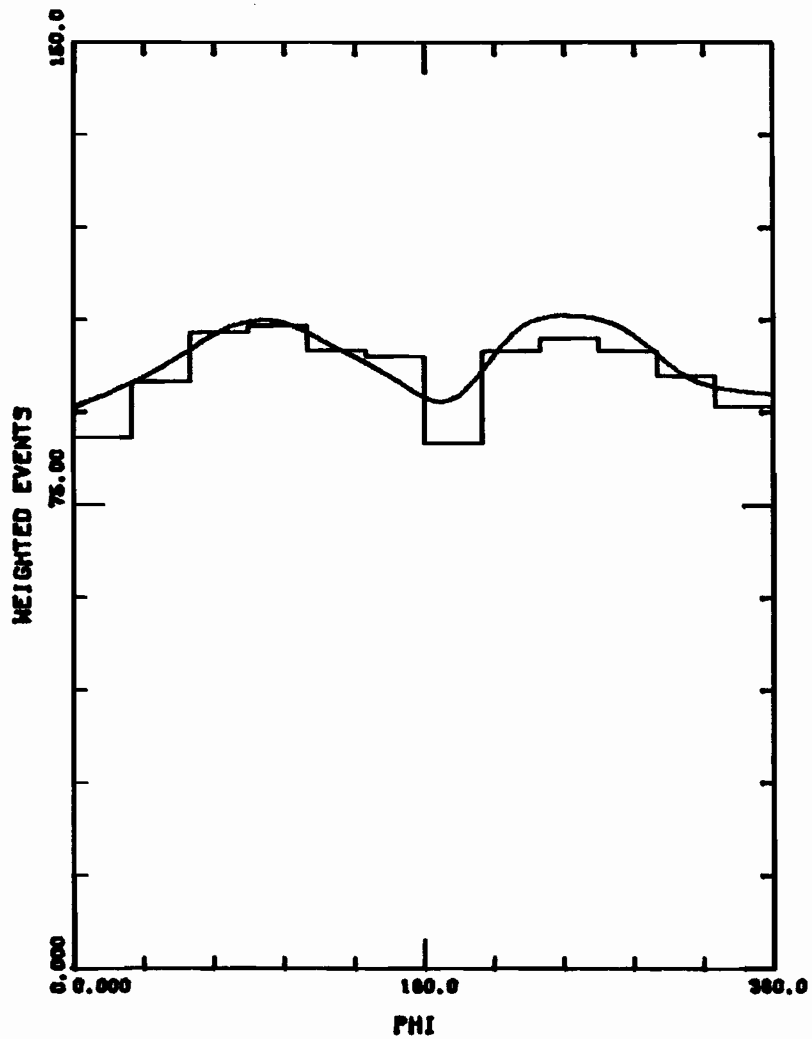

FIGURE 29d Mass Bin Analysis (1.23-1.38)GeV Φ

CHAPTER 10

EXPERIMENTAL RESULTS AND CONCLUSIONS

10.A. Results

The results of the fits detailed in Chapter 9 are presented in Tables 12 and 13.

Charged B results [26, 27] have shown that natural parity (NPE) dominates in 1^+ production. We do not expect any sizeable unnatural-parity contributions, for 1^+ states can only couple in helicity 1 to such an exchange. Our results confirm this as ρ_{00} and ρ^- are significantly nonzero for the 1^+ state. We therefore expect B^o to be predominantly produced by A_2 exchange (A_2 is the only candidate for NPE as ω is forbidden in charge exchange).

In Table 12, we see that for the 1^- wave, ρ_{00} and ρ^- are quite large, implying unnatural parity exchange (UPE). As expected for UPE (mostly π - exchange), $\rho_{00} d\sigma/dt$ is strongly ($t' = 0$) peaked in the forward direction. The t' structure strongly suggests the presence of a $J^P=1^-$ ρ' resonance. Such a resonance has been observed [42] in the reaction $e^+e^- \to \pi^+\pi^-\pi^o\pi^o$ and in photoproduction [43], $\gamma p \to \pi^+\pi^-\pi^o\pi^o p$, at a mass of 1.250 GeV/c.

The results of our mass bin analysis (Table 13) show that the B^o and $\rho'(1250)$ density matrix elements vary little as a function of mass. The values of $|F_0|^2$ (and hence

TABLE 12

t'-BIN ANALYSIS RESULTS

t'-Bin	(.00 - .13) GeV^2	(.13 - .57) GeV^2
1^+:		
$\|F_0\|^2$	.146 ± .040	.085 ± .023
$(D/S)^2$	.052 ± .015	.109 ± .020
ρ_{00}	.175 ± .042	.310 ± .019
ρ^+	.395 ± .051	.367 ± .014
ρ^-	.490 ± .051	.313 ± .014
$Re[\rho_{10}]$	.056 ± .024	.031 ± .005
$N(1^+)$	14078 ± 729 (61.0%)	9840 ± 330 (91.0%)*
$\sigma_N^0=\rho_{00}d\sigma/dt'$	2464 ± 608	3050 ± 211
$\sigma_N^1=\rho^- d\sigma/dt'$	6898 ± 773	3080 ± 183
$\sigma_U^1=\rho^+ d\sigma/dt'$	5561 ± 773	3611 ± 183
$\sigma_{INT}=\sqrt{2}Re[\rho_{10}]d\sigma/dt$	1115 ± 487	431 ± 66
1^-:		
ρ_{00}	.512 ± .041	.412 ± .519
ρ^+	.132 ± .083	.321 ± .308
ρ^-	.498 ± .083	.282 ± .308
$Re[\rho_{10}]$	-.037 ± .101	.008 ± .183
$N(1^-)$	8268 ± 617 (35.5%)	847 ± 318 (8.0%)*
$\sigma_U^0=\rho_{00}d\sigma/dt'$	4232 ± 466	349 ± 459
$\sigma_U^0=\rho^- d\sigma/dt'$	4117 ± 752	239 ± 275
$\sigma_N^1=\rho^+ d\sigma/dt'$	1091 ± 690	272 ± 280
$\sigma_{INT}=\sqrt{2}Re[\rho_{10}]d\sigma/dt$	-433 ± 1181	10 ± 219
N(BKGD)	804 ± 310 (3.5%)	100 ± 182 (1.0%)*

* Values are normalized to the first t'-bin.

TABLE 13

MASS BIN ANALYSIS RESULTS

Mass Bin	(1.08 - 1.23) GeV	(1.23 - 1.38) GeV
1^+:		
$\|F_0\|^2$	.083 ± .007	.107 ± .008
$(D/S)^2$	.112 ± .005	.084 ± .005
ρ_{00}	.391 ± .005	.485 ± .004
ρ^+	.443 ± .015	.319 ± .021
ρ^-	.171 ± .015	.237 ± .021
$Re[\rho_{10}]$	-.003 ± .008	.043 ± .010
1^+ fraction	(74 ± 3)%	(77 ± 3)%
1^-:		
ρ_{00}	.662 ± .240	.617 ± .137
ρ^+	.239 ± .221	.207 ± .092
ρ^-	.140 ± .221	.202 ± .092
$Re[\rho_{10}]$	-.078 ± .130	-.009 ± .493
1^- fraction	(24 ± 3)%	(21 ± 2)%
Background fraction	(2 ± 2)%	(2 ± 1)%

the values of the ratio D/S) are consistent (within error) with those given for the t' bins.

The production mechanisms of the B^{o} and $\rho'(1250)$ are discussed in detail in Section 10.C.

10.B. D/S Ratio

Decay of nonstrange <u>35</u> ($L_{q\bar{q}} = 1$) mesons [44] by pion emission to <u>35</u> ($L_{q\bar{q}} = 0$) mesons are described [37] in an $SU(6)_W$ model of current and constituent quarks in terms of two reduced matrix elements, A and B.

$$F_1(A_1 \to \rho\pi) = \frac{1}{8}\sqrt{3}A + \frac{1}{12}\sqrt{6}B \quad ,$$

$$F_0(A_1 \to \rho\pi) = \frac{1}{\sqrt{6}}B \quad ,$$

$$F_1(B \to \omega\pi) = -\frac{1}{6}\sqrt{3}B$$

and

$$F_0(B \to \omega\pi) = -\frac{1}{8}\sqrt{6}A \quad ,$$

with $|F_0|^2 + 2|F_1|^2 = 1$.

Furthermore, duality [38,39] predicts for the A_1 that

$$\left(\frac{F_1}{F_0}\right)_{A_1 \to \rho\pi} = \frac{3}{4} \quad ,$$

in agreement with experimental results [40]. This implies

$$\left(\frac{F_1}{F_0}\right)_{B \to \omega\pi} = 2 \quad .$$

With the above normalization, we obtain $|F_0|^2 = .11$ and $(D/S)^2 = .08$.

Our values for $(D/S)^2$ range from $.05 \pm .02$ to $.11 \pm .01$, in good agreement with the above prediction.

10.C. Spin Projected Cross Sections

In this section we present the s-channel spin projected differential cross-sections for the processes

$$\pi^- p \rightarrow B^o n \qquad (10\text{-}1)$$

and

$$\pi^- p \rightarrow \rho'(1250) n \qquad (10\text{-}2)$$

and discuss the production mechanisms that may contribute to each of these.

The measured cross-sections for reaction (10-1) shown in Figures 30 to 33 are defined as [41]

$$\sigma_N^0 = \rho_{00} \frac{d\sigma}{dt} = |N_{++}^0|^2 + |N_{+-}^0|^2 \ ,$$

$$\sigma_N^1 = \rho^- \frac{d\sigma}{dt} = |N_{++}^1|^2 + |N_{+-}^1|^2 \ ,$$

$$\sigma_U^1 = \rho^+ \frac{d\sigma}{dt} = |U_{++}^1|^2 + |U_{+-}^1|^2$$

and

$$\sigma_{INT} = \sqrt{2}\,\mathrm{Re}[\rho_{10}]\frac{d\sigma}{dt} = \mathrm{Re}[N_{++}^1 N_{++}^{0*} + N_{+-}^1 N_{+-}^{0*}] \ ,$$

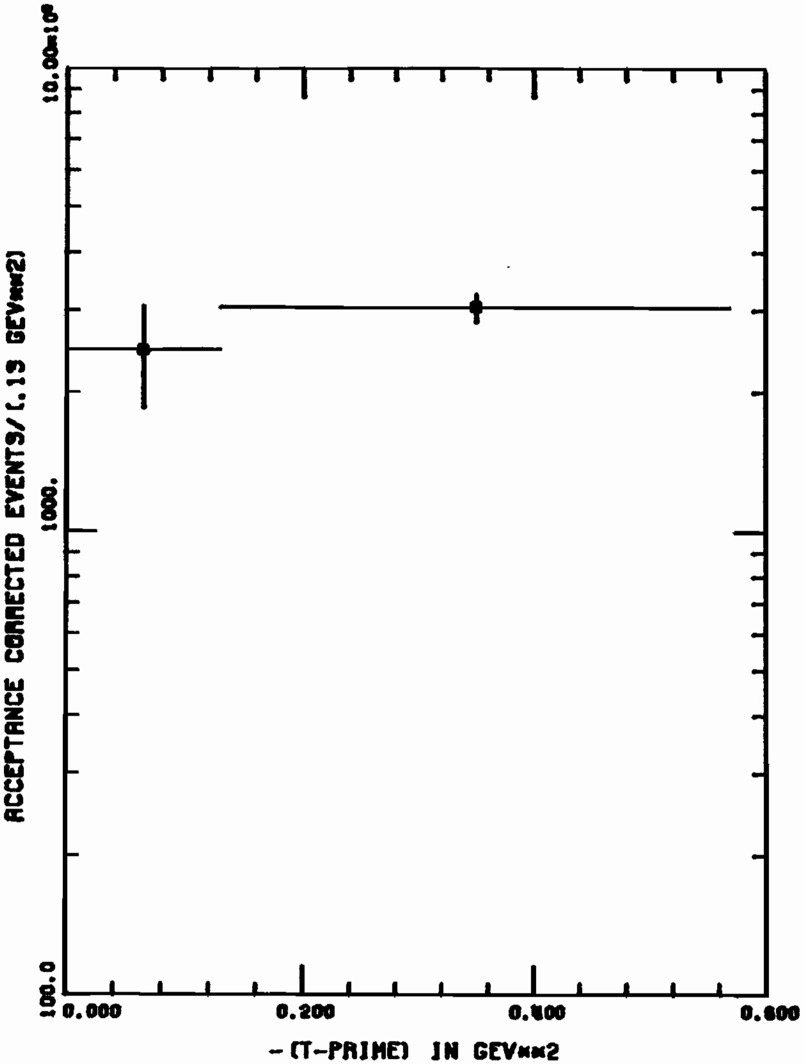

FIGURE 30 σ_N^0: $\pi^- p \rightarrow B(1235)n$

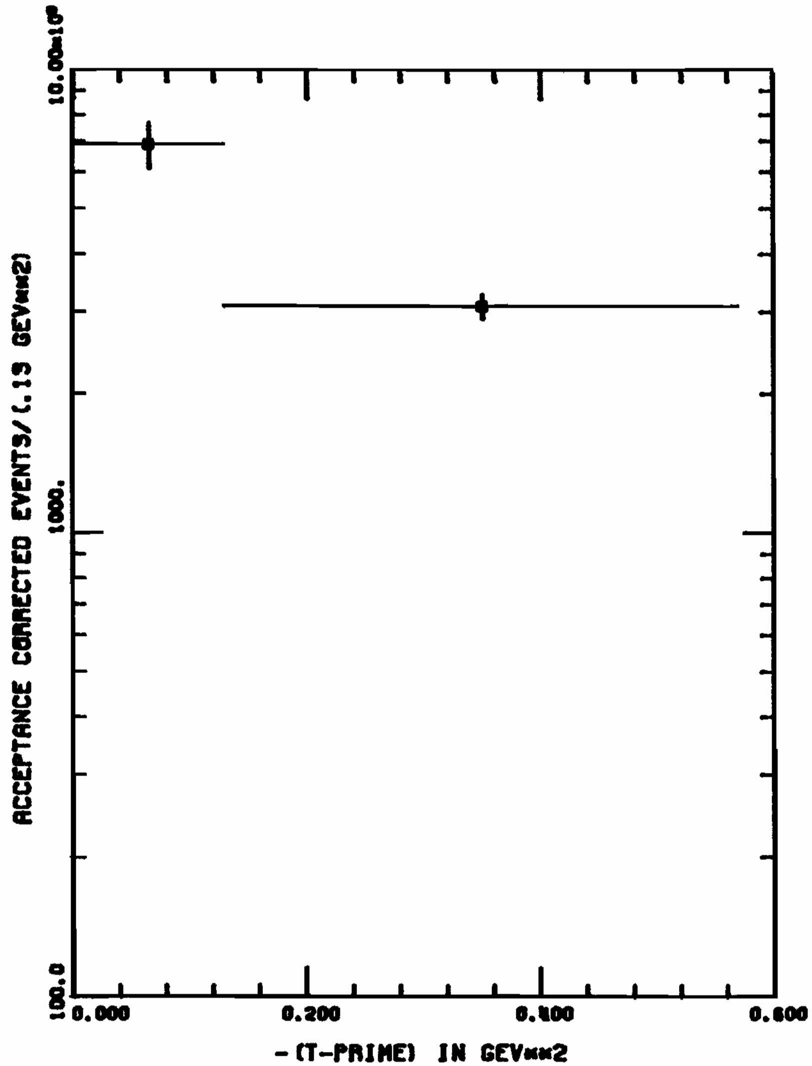

FIGURE 31 σ_N^1: $\pi^- p \rightarrow B(1235)n$

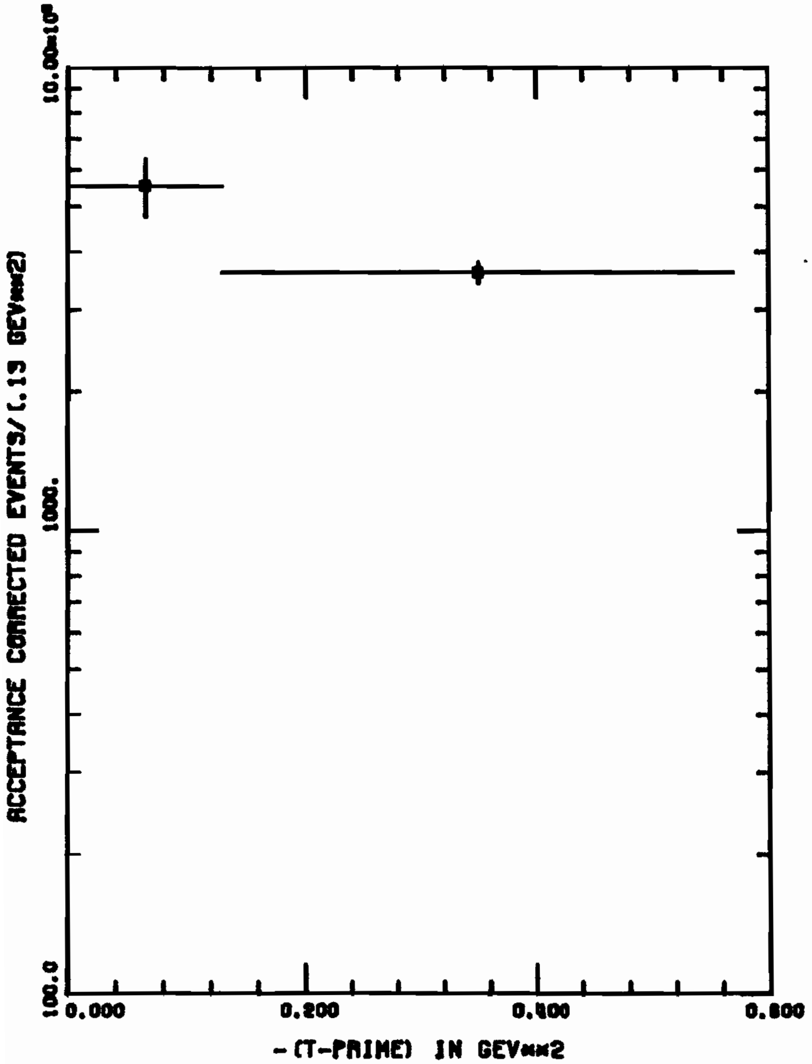

FIGURE 32 σ_U^1: $\pi^- p \rightarrow B(1235)n$

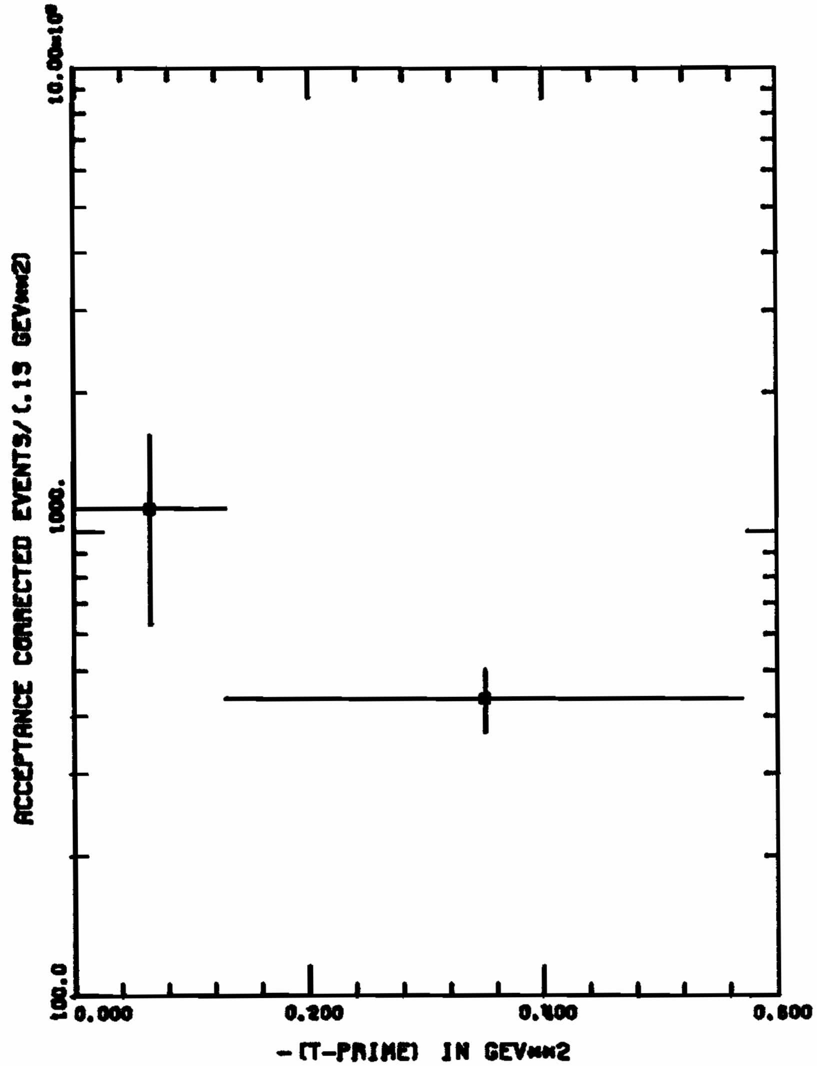

FIGURE 33 σ_{INT}: $\pi^- p \rightarrow B(1235)n$

where $\rho^{\pm} = \rho_{11} \pm \rho_{1-1}$,

N = natural parity exchange in the t-channel

and U = unnatural parity exchange in the t-channel.

The subscripts, ++ and +-, indicate the proton and neutron helicities (λ_p, λ_n). The superscripts are the meson (B^0, ρ') helicities (e.g., N^0_{+-} is the amplitude for nucleon helicity-flip and a helicity zero meson).

For reaction (10-2) the cross sections (Figures 34 to 37) are defined as [33]

$$\sigma^0_U = \rho_{00}\frac{d\sigma}{dt} = |U^0_{++}|^2 + |U^0_{+-}|^2 \quad ,$$

$$\sigma^1_U = \rho^-\frac{d\sigma}{dt} = |U^1_{++}|^2 + |U^1_{+-}|^2 \quad ,$$

$$\sigma^1_N = \rho^+\frac{d\sigma}{dt} = |N^1_{++}|^2 + |N^1_{+-}|^2$$

and

$$\sigma_{INT} = \sqrt{2}\mathrm{Re}[\rho_{10}]\frac{d\sigma}{dt} = \mathrm{Re}[U^1_{++}U^{0*}_{++} + U^1_{+-}U^{0*}_{+-}] \quad .$$

We have chosen the combinations $\rho^{\pm}$ of the density matrix elements in order to isolate natural and unnatural parity exchange to the t-channel. This enables us to interpret the cross-sections in terms of Regge poles [32] (see Figure 38) and Regge cuts (see Figure 39) in the t-channel.

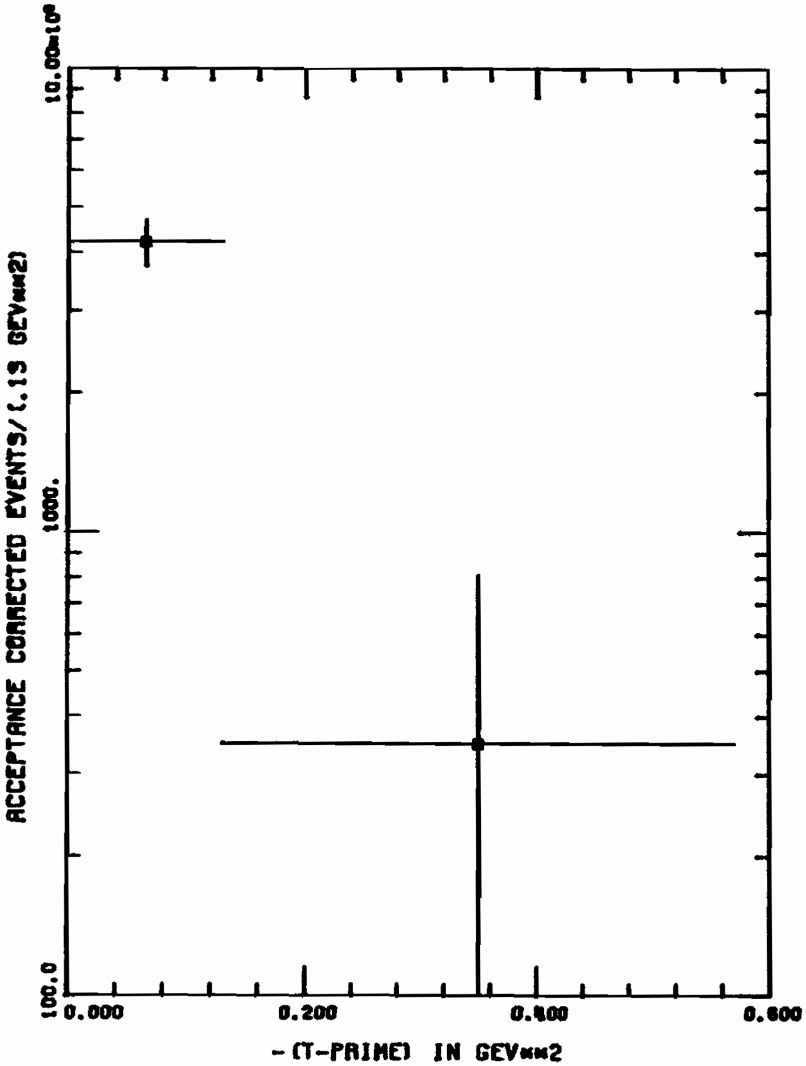

FIGURE 34 σ_U^0: $\pi^- p \to \rho'(1250)n$

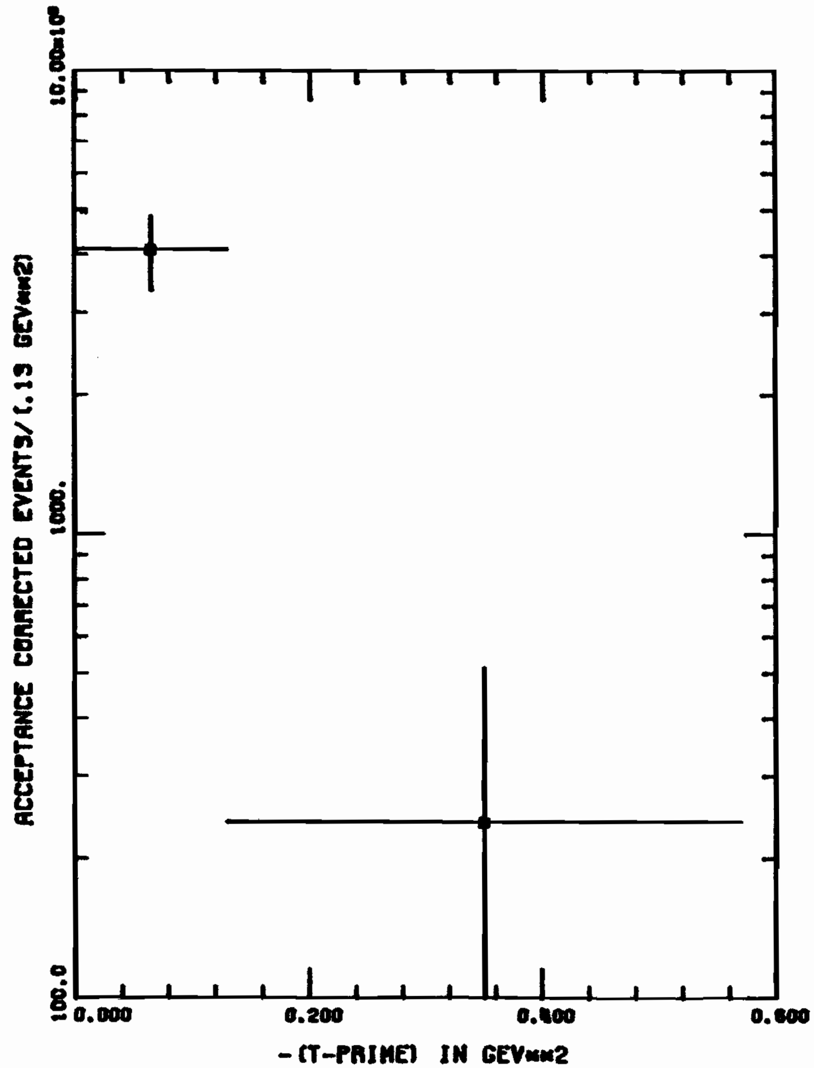

FIGURE 35 σ_U^1: $\pi^- p \to \rho'(1250)n$

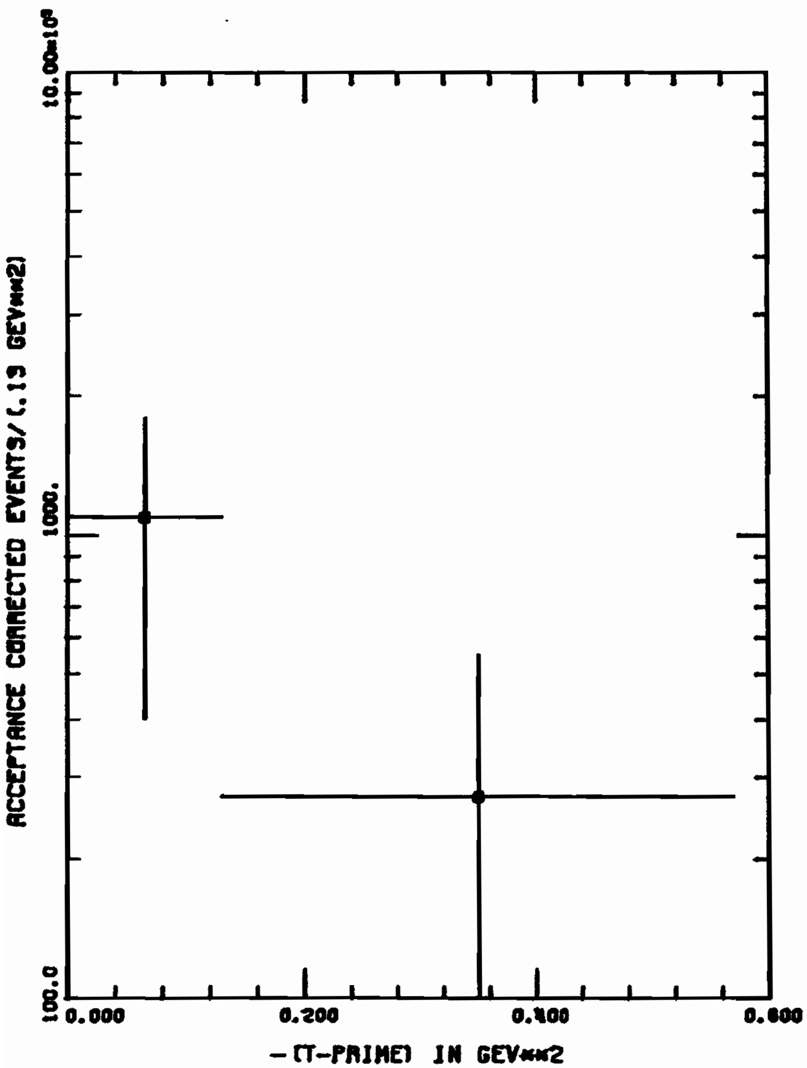

FIGURE 36 σ_N^1: $\pi^- p \to \rho'(1250)n$

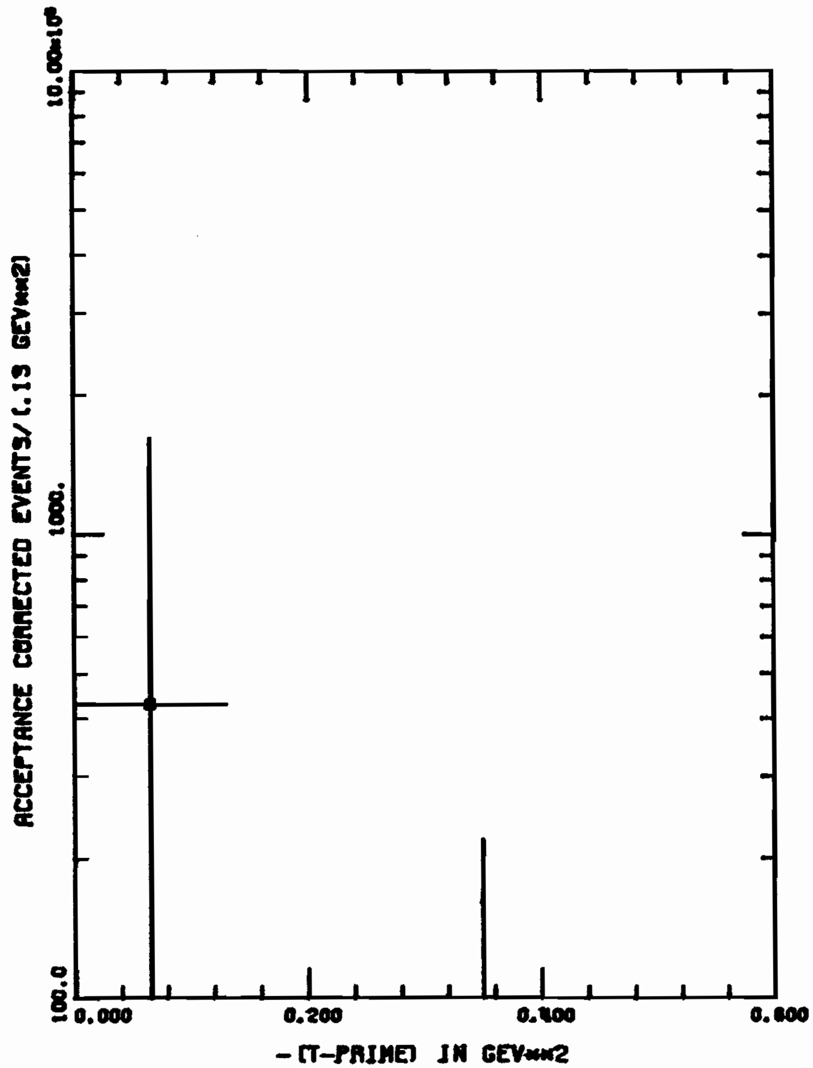

FIGURE 37 σ_{INT}: $\pi^- p \to \rho'(1250)n$

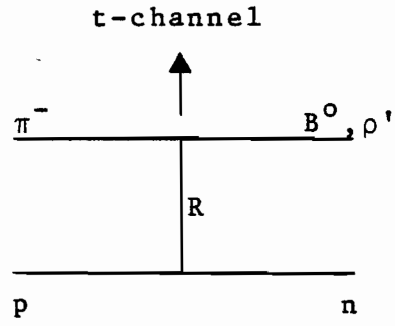

FIGURE 38

Exchange of a Regge pole in the t-channel

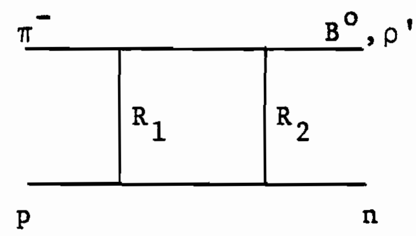

FIGURE 39

A Regge cut may be interpreted as the exchange of two Regge poles

The simplest production models for reactions similar to (10-1) and (10-2) consider only Regge poles, but cuts are often added as a convenient parameterization when the poles provide an incomplete description of the data [33]. We will show that this is the case for reactions (10-1) and (10-2).

The Regge pole amplitudes are written as [33]

$$R^{\Lambda}_{\lambda_p\lambda_n} = \beta^{\Lambda}_{\lambda_p\lambda_n R} f^{\Lambda}_{\lambda_p\lambda_n}(t')_R \ \xi_R \quad .$$

The factor ξ_R includes the Regge pole amplitude s dependence factor, $(\frac{s}{s_0})^{\alpha_R(t)}$, and a signature factor, $(\frac{1 \pm e^{i\pi\alpha_R(t)}}{2})$. For particle exchange, this factor corresponds to $(-1)^{J_{EXCHANGE}}$. $\alpha_R(t) = \alpha_0 + \alpha' t$ is the Regge trajectory or t dependence of the Regge angular momentum. The factor $f^{\Lambda}_{\lambda_p\lambda_n}$ gives the dominant t-dependence of the Regge pole amplitude; it is derived from consideration of angular momentum conservation (see Appendix F). The factor β, the Regge residue, is then the remaining coupling factor of the Regge pole to the meson and nucleon vertices. In our discussion, we will be primarily interested in the t-dependent factor $f^{\Lambda}_{\lambda_p \lambda_n}$.

If we consider conservation of parity and of g-parity at the meson and nucleon verticies and the conservation of angular momentum (Appendix F), then we can parameterize the s-channel helicity amplitudes [34] for reaction (10-1) in terms of A_1, A_2 and A_3 Regge poles as follows:

$$N^0_{++} = A^0_{2++} e^{b_{A_2} t'} \xi_{A_2} \quad , \tag{10-3}$$

$$N^0_{+-} = A^0_{2+-} (-t')^{\frac{1}{2}} e^{b_{A_2} t'} \xi_{A_2} \quad , \tag{10-4}$$

$$N^1_{++} = A^1_{2++} (-t')^{\frac{1}{2}} e^{b_{A_2} t'} \xi_{A_2} \quad , \tag{10-5}$$

$$N^1_{+-} = A^1_{2+-} (-t') e^{b_{A_2} t'} \xi_{A_2} \quad , \tag{10-6}$$

$$U^1_{++} = A^1_{1++} (-t')^{\frac{1}{2}} e^{b_{A_1} t'} \xi_{A_1} + A^1_{3++} (-t')^{\frac{1}{2}} e^{b_{A_3} t'} \xi_{A_3} \tag{10-7}$$

and

$$U^1_{+-} = A^1_{1+-} (-t') e^{b_{A_1} t'} \xi_{A_1} + A^1_{3+-} (-t') e^{b_{A_3} t'} \xi_{A_3} + A^{1*}_{3+-} e^{b_{A_3} t'} \xi_{A_3} \quad . \tag{10-8}$$

Note that δ ($I^G J^{PC} = 1^- 0^{++}$) can also be exchanged. We shall not consider δ exchange, however, since its Regge trajectory lies lower than that of the A_2.

σ_N^0 for reaction (10-1) (Figure 30) shows some evidence for a forward turnover (a dip near t'=0), and suggests that our parameterization of N_{++}^0 and N_{+-}^0 (equations (10-3) and (10-4)) is sufficient. The distribution indicates dominance of A_2 exchange in the nucleon spin flip amplitude over the spin non-flip amplitude. The non-flip amplitude is certainly not negligible as was indicated in the reactions $\pi^- p \to \eta n$ and $\pi^- p \to \eta' n$ [35] .

In Figure 31, we see that σ_N^1 has a clear forward peak. Since our Regge pole parameterization only includes amplitudes (10-5) and (10-6) which vanish in the forward direction, we are obliged to add Regge cuts to our helicity amplitudes. From angular momentum conservation considerations [32], it is expected that Regge cuts with a net helicity flip of zero ($n = |\Lambda+\lambda_n-\lambda_p|$) in the s-channel should dominate over those with $n \neq 0$. Therefore, we consider only the case of $n = 0$. For σ_N^1 we add the appropriate cut (ρ-A_2) to N_{+-}^1 :

$$N_{+-}^1 \to N_{+-}^1 + \rho A_{2+-}^c e^{b_c t'} \xi_c \quad . \tag{10-9}$$

In Figure 32 we see that σ_U^1 also does not vanish in the forward direction. This forward peak could be accounted for by the nonvanishing A_3 exchange term. If, however, the $\pi A_3 B^o$ coupling is small, as may be indicated in $\pi^- p \to A_3 n$ [36] , then this forward peak could be the result of a ρ-A_1

cut added to N^1_{+-} . In fact, one would naively expect these cuts to be present in both $\Lambda = 1$ amplitudes.

Our Regge pole model for reaction (10-2) gives (Appendix F and [34])

$$U^0_{++} = A^0_{1++} e^{b_{A_1} t'} \xi_{A_1} , \tag{10-10}$$

$$U^0_{+-} = \pi^0_{+-} (-t')^{\frac{1}{2}} e^{b_\pi t'} \xi_\pi + A^0_{1+-} (-t')^{\frac{1}{2}} e^{b_{A_1} t'} \xi_{A_1} , \tag{10-11}$$

$$U^1_{++} = A^1_{1++} (-t')^{\frac{1}{2}} e^{b_{A_1} t'} \xi_{A_1} + A^1_{3++} (-t')^{\frac{1}{2}} e^{b_{A_3} t'} \xi_{A_3} , \tag{10-12}$$

$$U^1_{+-} = A^1_{1+-} (-t') e^{b_{A_1} t'} \xi_{A_1} + A^1_{3+-} (-t') e^{b_{A_3} t'} \xi_{A_3} \tag{10-13}$$

$$+ A^{1*}_{3+-} e^{b_{A_3} t'} \xi_{A_3} ,$$

$$N^1_{++} = A^1_{2++} (-t')^{\frac{1}{2}} e^{b_{A_2} t'} \xi_{A_2} \tag{10-14}$$

and

$$N^1_{+-} = A^1_{2+-} (-t') e^{b_{A_2} t'} \xi_{A_2} . \tag{10-15}$$

In Figure 34, we see that σ^0_U for reaction (10-2) has a very steep forward peak. In $\pi^- p \to \rho^o n$ [33,34], where the production mechanisms are expected to be the same as for reaction (10-2), σ^0_U has been shown to be dominated by the π exchange contribution to U^0_{+-}. We suggest that this is also the case for $\pi^- p \to \rho' n$. Two additional amplitudes, A_1 exchange and a ρ-A_1 cut, can contribute in U^0_{++} to a forward-peaked σ^0_U . These, however, are not strictly required.

The only Regge pole exchange which can cause the forward peak in σ^1_U (Figure 35) is A_3 in spin flip. If the

$\rho'\pi A_3$ coupling is small, then we may again add a ρ-A_1 cut to U^1_{+-} (net helicity = 0), so that

$$U^1_{+-} \rightarrow U^1_{+-} + \rho A^c_{1+-} e^{b_c t'} \xi_c \quad .$$

The situation in natural parity exchange (Figure 36) suggests that we cannot avoid invoking a Regge cut to describe the forward peak in σ^1_N. In this case, we must add a ρ-A_2 cut,

$$N^1_{+-} \rightarrow N^1_{+-} + \rho A^c_{2+-} e^{b_c t'} \xi_c \quad .$$

10.D. Conclusions

Our study of the B^o indicates dominance of A_2 exchange in the nucleon spin flip amplitude over the spin non-flip amplitude. We find that we must include a ρ-A_2 cut to explain our σ^1_N distribution. There is also a possibility of A_3 exchange and of a ρ-A_1 cut contribution.

We found the amount of D-wave in the $B^o \rightarrow \omega\pi$ decay to be quite significant (approximately 8%) and in agreement with theory [38, 39].

The production mechanisms for $\rho'(1250)$ are similar to those for ρ^o production, and are dominated by π exchange. A_1 exchange may also contribute.

10.E. Future Analysis

We have, from data taken in a previous experiment (E397 at the ZGS), an additional sample of $\pi^+\pi^-\pi^o\pi^o$ events equal to our present statistics. These events have somewhat different resolution and geometric acceptance than our present sample; nevertheless, the two samples could be combined, and the statistics would then allow us to do a finer bin analysis. This would result in a reduction of the error bars on the production and decay parameters of the B^o and $\rho'(1250)$ resonances.

In particular, a finer mass bin analysis could give definite results on the resonant nature of the 1^- wave. More J^P states could be included in the fit and a coherent model could also be employed. We could search for the $\rho'(1600)\to\omega\pi^o$ ($J^{PC} = 1^{--}$), $Z \to \omega\pi^o(2^{--})$ and $g \to \omega\pi^o(3^{--})$ decays (which are all $L_{q\bar{q}} = 2$ states).

Another member of our collaboration [45] is currently analyzing $\omega\pi^-$ data ($\pi^-p \to \omega\pi^-p$) collected concurrently with the $\omega\pi^o$ sample. Owing to better acceptance, the $\omega\pi^-$ sample is three times larger than our neutrally charged sample. We hope to get a very accurate determination of the ratio D/S for the B^- meson. With the available statistics, we should also be able to observe some of the $L_{q\bar{q}} = 2$ states mentioned above.

Finally, we probably have enough events with the combined neutral samples to perform a partial wave analysis on the data (this is certainly the case with the charged sample). The detection of phase motion would positively confirm the resonant behaviour of the B^o and $\rho'(1250)$ mesons.

APPENDIX A

CONSTRAINED PARAMETER FIT FORMULATION

This appendix deals with the constrained parameter fitting techniques used in the "tuning" part of the analysis. The process is used to determine systematic errors in the parameters that define the trajectories of the charged particles and the measured energies of the gamma rays.

A.A. Charged Particle Trajectories

First, consider a brief description of the charged particle trajectory fit (as we use some of the results obtained in this fit in the overall constrained parameter fit that follows). As derived in Appendix B, we can parameterize the trajectories as follows (see (B-3)):

$$x_i \simeq \alpha_1 + \alpha_2 z_i + \frac{1}{p} X(z_i)$$

$$y_i \simeq \alpha_3 + \alpha_4 z_i + \frac{1}{p} Y(z_i) \quad ,$$

where x_i = measured coordinate for ith x plane,

y_i = measured coordinate for ith y plane,

$i = 1,\ldots,10$,

α_1 = x intercept at z=0,

α_2 = x slope of trajectory,

α_3 = y intercept at z=0,

α_4 = y slope of trajectory

and p = momentum of particle.

Adopting matrix notation, the above system can be rewritten as

$$\bar{y} \simeq A\bar{\alpha} \quad , \tag{A-1}$$

where $\bar{y}^T = (x_1,\ldots,x_{10},y_1,\ldots,y_{10})$,

$\bar{\alpha}^T = (\alpha_1,\alpha_2,1/p,\alpha_3,\alpha_4)$

and A is the appropriate 20x5 matrix.

If $\bar{\eta}$ is a vector of fitted coordinates, then

$$\bar{\eta} = A\bar{\alpha} \tag{A-2}$$

and the Chi-square [18] can be written as

$$\chi^2 = \bar{\Delta}^T G_y \bar{\Delta} = (\bar{\eta} - \bar{y})^T G_y (\bar{\eta} - \bar{y})$$

$$= (A\bar{\alpha} - \bar{y})^T G_y (A\bar{\alpha} - \bar{y}) \quad , \tag{A-3}$$

where G_y is the covariance matrix for position measurements. To solve for the optimal orbital parameters, $\bar{\alpha}$, we minimize the χ^2 with respect to $\bar{\alpha}$. Using

$$\frac{d[A^T cA]}{dA} = 2A^T c \tag{A-4}$$

and setting $\partial\chi^2/\partial\bar{\alpha} = 0$, we obtain

$$\tfrac{1}{2}\frac{\partial\chi^2}{\partial\bar{\alpha}} = A^T G_y (A\bar{\alpha} - \bar{y}) = 0 \quad .$$

The solution is

$$\bar{\alpha} = (A^T G_y A)^{-1} A^T G_y \bar{y} \quad . \qquad \text{(A-5)}$$

Now the error in position for the ith chamber plane, Δ_i , can be expressed as

$$\Delta_i = \sum_j p_{ij} f_{ij}(y_i) \ , \quad i = 1,\ldots,20, \quad j = 1,\ldots,k,$$

where k is the number of parameters. Therefore, once the parameters p_{ij} are determined, a new $\bar{y}_N$ can be calculated as follows:

$$\bar{y}_N = \bar{y} + \sum_j p_{ij} f_{ij}(y_i) \quad . \qquad \text{(A-6)}$$

To find the optimal parameters and thus reduce systematic errors, we must minimize the χ^2 with respect to the p_{ij}.

Performing a Taylor series expansion about χ^2_{min} , we obtain

$$\chi^2(p_{1,1}=0,\ldots,p_{20,k}=0) = \chi^2_{min} + \{\frac{\partial\chi^2}{\partial p_{1,1}}(p_{1,1} - p^0_{1,1})$$

$$+ \frac{\partial\chi^2}{\partial p_{1,2}}(p_{1,2} - p^0_{1,2}) + \cdots + \frac{\partial\chi^2}{\partial p_{20,k}}(p_{20,k} - p^0_{20,k}) \}$$

$$+ .5 \left\{ \frac{\partial^2\chi^2}{\partial p_{1,1}^2}(p_{1,1} - p_{1,1}^0)^2 + \right.$$

$$+ 2\frac{\partial^2\chi^2}{\partial p_{1,1}\partial p_{1,2}}(p_{1,1} - p_{1,1}^0)(p_{1,2} - p_{1,2}^0) + \ldots$$

$$+ 2\frac{\partial^2\chi^2}{\partial p_{20,k-1}\partial p_{20,k}}(p_{20,k-1} - p_{20,k-1}^0)(p_{20,k} - p_{20,k}^0)$$

$$\left. + \frac{\partial^2\chi^2}{\partial p_{20,k}^2}(p_{20,k} - p_{20,k}^0)^2 \right\} + \ldots \tag{A-7}$$

where p_{ij}^0 is the value of p_{ij} at $\chi^2{}_{min}$. Since no p_{ij} have yet been added to the $\bar{y}$, we have χ^2 evaluated at $p_{1,1} = 0, \ldots, p_{20,k} = 0$. Reverting to vector notation, (A-7) can be expressed as

$$\chi^2 = \chi^2{}_{min} + \frac{\partial\chi^2\bar{\rho}}{\partial\bar{\rho}} + \frac{\partial\chi^2\bar{\rho}^T\bar{\rho}}{\partial\bar{\rho}^T\partial\bar{\rho}} + \ldots, \tag{A-8}$$

where $\rho_{ij} = -p_{ij}^0$. Demanding that $\chi^2 = \chi^2{}_{min}$ gives

$$\frac{\partial^2\chi^2\bar{\rho}}{\partial\bar{\rho}^T\partial\bar{\rho}} + \frac{\partial\chi^2}{\partial\bar{\rho}} = 0 \quad , \tag{A-9}$$

where third and higher order terms in (A-7) have been neglected.

The χ^2 expression actually minimized (for the charged particle spectrometer) is

$$\chi^2 = \bar{\Delta}^T G_y \bar{\Delta} + \frac{(\Delta P)^2}{\sigma_P^2} + \bar{\rho}^T G_\rho \bar{\rho} \ , \tag{A-10}$$

where $\bar{\Delta} = A\bar{\alpha} - \bar{y}$,

ΔP = fitted momentum - unfitted momentum,

G_y = covariance matrix for position measurements

and G_ρ = covariance matrix for parameters.

The first term is the standard χ^2 from the trajectory fit (see (A-3)), while the next term takes some physics into account. ΔP is the difference between the momentum of a charged particle before and after a missing mass constraining fit (i.e., the missing mass is constrained to equal the neutron mass). This second term prevents solutions where the χ^2 is at a good minimum but known particle masses have slipped away from correct values.

The last term in the expression is the so-called "non-slip" term which prevents parameter runaway [20] . It allows each parameter to be individually weighted through the covariance matrix, G_ρ . One of the problems to be guarded against is that a solution in which all the offsets (p_{i1} are the offsets; see (A-17)) are 2", say, is perfectly viable as far as the physics is concerned. This problem is eliminated by adding the "non-slip" term to the χ^2 and weighting all offsets very heavily against running away.

Using (A-4) and separating the "non-slip" term out of (A-8), we can write

$$\frac{\partial^2 \chi^2 \bar{\rho}}{\partial \bar{\rho}^T \partial \bar{\rho}} + \frac{\partial \chi^2}{\partial \bar{\rho}} + G_\rho \bar{\rho} = 0 \quad . \qquad \text{(A-11)}$$

To get a statistically valid fit, solve for $\bar{\rho}$, not from one track, but from thousands of events. Thus, (A-11) becomes

$$\sum_{\text{events}} \frac{\partial^2 \chi^2 \bar{\rho}}{\partial \bar{\rho}^T \partial \bar{\rho}} + G_\rho \bar{\rho} + \sum_{\text{events}} \frac{\partial \chi^2}{\partial \bar{\rho}} = 0 \quad , \qquad \text{(A-12)}$$

where we have pulled $G_\rho \bar{\rho}$ out of the sum since its value does not vary event by event. Finally, the solution is given by

$$\bar{\rho} = \left[\sum_{\text{events}} - \frac{\partial^2 \chi^2}{\partial \bar{\rho}^T \partial \bar{\rho}} + G_\rho \right]^{-1} \left[\sum_{\text{events}} \frac{\partial \chi^2}{\partial \bar{\rho}} \right] . \qquad \text{(A-13)}$$

Now, we need only evaluate the above derivatives to determine the p_{ij} , which, with the use of (A-6), gives a new estimate for $\bar{y}$.

The derivatives can be calculated from measured quantities as follows (using (A-4)):

$$\frac{\partial \chi^2}{\partial \bar{\rho}} = 2\bar{\Delta}^T G_y \frac{\partial(\bar{\Delta})}{\partial \bar{\rho}} + \frac{2\Delta P}{\sigma_P^2} \frac{\partial(\Delta P)}{\partial \bar{\rho}}$$

and
$$\frac{\partial \Delta P}{\partial \bar{\rho}} = \frac{\partial P}{\partial \bar{\alpha}} \frac{\partial \bar{\alpha}}{\partial \bar{y}} \frac{\partial \bar{y}}{\partial \bar{\rho}} \quad .$$

Therefore,

$$\frac{\partial \chi^2}{\partial \bar{\rho}} = 2\bar{\Delta}^T G_y \frac{\partial(\bar{\Delta})}{\partial \bar{\rho}} + \frac{2\Delta P}{\sigma_P^2} \frac{\partial P}{\partial \bar{\alpha}} \frac{\partial \bar{\alpha}}{\partial \bar{y}} \frac{\partial \bar{y}}{\partial \bar{\rho}} \quad ,$$

with

$$\frac{\partial(\bar{\Delta})}{\partial \bar{\rho}} = \frac{\partial(A\bar{\alpha} - \bar{y})}{\partial \bar{\rho}} = \frac{\partial(A\bar{\alpha})}{\partial \bar{\rho}} - \frac{\partial \bar{y}}{\partial \bar{\rho}} = A\frac{\partial \bar{\alpha}}{\partial \bar{y}} \frac{\partial \bar{y}}{\partial \bar{\rho}} - \frac{\partial \bar{y}}{\partial \bar{\rho}} \quad . \qquad \text{(A-14)}$$

Next, $\partial P/\partial \bar{\alpha}$ can be determined by writing

$$P \propto Kq/\theta_B \quad ,$$

where K = constant,

q = charge on particle

and θ_B = bend in trajectory due to field $\bar{B}$

= downstream slope - upstream slope.

Also, from (A-1), recall that

$$\bar{\alpha} = \begin{bmatrix} \alpha_1 = \text{x intercept at } z = 0 \\ \alpha_2 = \text{x slope of trajectory} \\ 1/p \\ \alpha_3 = \text{y intercept at } z = 0 \\ \alpha_4 = \text{y slope of trajectory} \end{bmatrix} .$$

Given that the magnetic field $\bar{B} = |\bar{B}|\hat{y}$, then

$$\frac{\partial P}{\partial \bar{\alpha}} = \begin{bmatrix} 0 \\ P/\theta_B \\ -1/P^2 \\ 0 \\ 0 \end{bmatrix} .$$

So finally, the first derivative equals

$$\frac{\partial \chi^2}{\partial \bar{\rho}} = 2\bar{\Delta}^T G_y \left(A \frac{\partial \bar{\alpha}}{\partial \bar{y}} \frac{\partial \bar{y}}{\partial \bar{\rho}} - \frac{\partial \bar{y}}{\partial \bar{\rho}}\right)$$

$$+ \frac{2\Delta P}{\sigma_P^2} \frac{\partial P}{\partial \bar{\alpha}} \frac{\partial \bar{\alpha}}{\partial \bar{y}} \frac{\partial \bar{y}}{\partial \bar{\rho}} , \qquad \text{(A-15)}$$

where $\bar{\Delta}$ is given by our trajectory fit (A-3),

$\partial\bar{\alpha}/\partial\bar{y}$ can be obtained from (A-5)

and $\partial\bar{y}/\partial\bar{\rho}$ can be predetermined from (A-6), and is the same for every event depending only on the choice of $f_{ij}(y_i)$.

Using (A-14), the second derivative gives

$$\frac{\partial \chi^2}{\partial \bar{\rho}^T \partial \bar{\rho}} = 2\left(A\frac{\partial \bar{\alpha}}{\partial \bar{y}}\frac{\partial \bar{y}}{\partial \bar{\rho}} - \frac{\partial \bar{y}}{\partial \bar{\rho}}\right) G_y \left(A\frac{\partial \bar{\alpha}}{\partial \bar{y}}\frac{\partial \bar{y}}{\partial \bar{\rho}} - \frac{\partial \bar{y}}{\partial \bar{\rho}}\right)$$

$$+ 2\left(\frac{\partial P}{\partial \bar{\alpha}}\frac{\partial \bar{\alpha}}{\partial \bar{y}}\frac{\partial \bar{y}}{\partial \bar{\rho}}\right)\frac{1}{\sigma_P^2}\left(\frac{\partial P}{\partial \bar{\alpha}}\frac{\partial \bar{\alpha}}{\partial \bar{y}}\frac{\partial \bar{y}}{\partial \bar{\rho}}\right) \quad . \qquad \text{(A-16)}$$

Equation (A-13) can now be solved for the parameters p_{ij} and, using (A-6), a corrected measurement vector, $\bar{y}_N$, can be calculated. Then set $\bar{y} = \bar{y}_N$ and repeat the fit until a stable solution is found.

In actual practice, the spectrometer chamber errors were parameterized as follows:

$$\begin{aligned} y_{Ni} = {} & y_i + p_{i1} + p_{i2}\frac{y_i}{z_i} + p_{i3}y_i \\ & + p_{i4}y_i^c + p_{i5}y_iy_i^c + p_{i6}y_i^2 \qquad \text{(A-17)} \\ & + p_{i7}y_i^2y_i^c + p_{i8}y_i^3 + p_{i9}y_i(y_i^c)^2 \ , \end{aligned}$$

where y_i = coordinate being fitted (plane i),

y_i^c = conjugate coordinate of that being fitted (plane i)

and z_i = z-position of plane i, i = 1,...,20.

p_{i1} is the offset or "surveyor" error for chamber i, p_{i2} is the error in the z coordinate for chamber i, p_{i3} is the scaling error for chamber i (to take into account variation in the propagation velocities of the magnetostrictive wires), etc.

Generally, only one or two parameters (never more than four) per chamber were fitted at once (for a maximum of eighty). Usually, the offset and the scale parameters were determined first, then fixed at those values; higher order parameters were then determined. Once all parameters were minimized, the procedure was repeated until an iteratively stable solution was found. The whole process was repeated many times as many solutions were found to be nonsensical.

A.B. Gamma Ray Energies

To determine the gamma ray detector systematics, the errors are parameterized as follows:

$$E_{Nk} = E_k + p_{k1} + p_{k2}E_k + p_{k3}E_k^{\frac{1}{2}} + p_{k4}E_k^{\frac{3}{2}} ,$$

where E_k = energy measured (in Pb glass block k)

and E_{Nk} = corrected energy (in Pb glass block k),

$k = 1,\ldots,56$.

p_{k1} are the offsets, p_{k2} are the scale errors and p_{k3} and p_{k4} correct for errors in the use of [21] $\Delta E = 1.8L^{\frac{3}{2}}(E-150)^{\frac{1}{2}}$ for determination of energy loss in lead by gamma rays.

In minimizing the χ^2 for p_{kj}, (A-10) cannot be used as it depends on $\bar{\Delta}^T$ obtained from the charged particle trajectory fit. Instead, use

$$\chi^2 = \Delta_E^T G_E \Delta_E + \bar{\rho}^T G_\rho \bar{\rho} \quad ,$$

where $\Delta_E = E_F - E_U$,

E_U = unfitted energy,

E_F = fitted energy

and G_E = covariance matrix for energy measurements.

The E_F's are determined by performing a constraining fit on the gamma ray energies. The two gamma rays forming the π^o have their energies and positions varied in such a way as to force the π^o effective mass to be 135 MeV. Equations (A-10) to (A-16) hold when the terms due to $(\Delta P)^2/\sigma_P^2$ in (A-10) are removed.

The scale parameters were determined individually for each block. It was found that there was no need to do this for the other parameters.

APPENDIX B

MOMENTUM DETERMINATION USING A QUINTIC SPLINE MODEL

In the "tuning" stage of the analysis, the quintic spline technique of H. Wind [22] was used to determine the momentum of the charged particles. The method used in the "offline" analysis required a trajectory fit first, as the momentum could then be determined by using this trajectory and comparing it to a table of Monte Carlo-generated trajectories. The "tuning"-stage method described here fits each individual track, taking into account the magnetic field at each measured coordinate. The momentum of the charged particle is a parameter in the fit for the trajectory.

The equations of motion of a charged particle in a magnetic field $\bar{B} = (B_x, B_y, B_z)$ are

$$\ddot{x} = (\dot{y}B_z - \dot{z}B_y)/m$$

and

$$\ddot{z} = (\dot{x}B_y - \dot{y}B_x)/m ,$$

where m is the mass, and

$$\ddot{x} = d^2x/dt^2 \text{ , etc.}$$

Using

$$\frac{dx}{dz} \equiv x' = \dot{x}/\dot{z} \quad ,$$

$$\frac{d^2x}{dz^2} \equiv x'' = (\ddot{x}\dot{z} - \dot{x}\ddot{z})/\dot{z}^3$$

and $$|\bar{p}| = m|\bar{v}| = m\dot{z}(1 + x'^2 + y'^2)^{\frac{1}{2}} \quad ,$$

we find that

$$px'' = (1+x'^2+y'^2)^{\frac{1}{2}}[B_z y'+B_x x'y'-B_y(1+x'^2)] \qquad \text{(B-1)}$$

and, similarly,

$$py'' = (1+x'^2+y'^2)^{\frac{1}{2}}[-B_z x'-B_y x'y'+B_x(1+y'^2)] \quad . \qquad \text{(B-2)}$$

Given an initial estimate of x' and y' and a map of the field $\bar{B}$, we can calculate the right-hand-side of equations (B-1) and (B-2) at the N chamber planes (z_i, i=1,N). It is therefore possible to derive cubic spline interpolants A(z) for px" and C(z) for py" [22,23]. A cubic spline is twice continuously differentiable; thus, its graph approximates the position which a draftsman's spline (i.e., a thin flexible rod) would occupy if it were constrained to pass through the points $\{A_i, z_i\}$.

With the interpolations

$$px'' = A(z) \quad \text{and} \quad py'' = C(z) \quad ,$$

we can calculate (see the appendix of [22]) the double integrals

$$X(z_i) \equiv \int_{u=z_1}^{u=z_i} \left[\int_{v=z_1}^{v=u} A(v)dv \right] du \quad ,$$

and, similarly, $Y(z_i)$. These functions are now expected to be a good representation of the track as far as the second derivative is concerned. The momentum p and the two integration constants must still be determined. Note that since a cubic spline is discontinuous in the third derivative, $X(z_i)$ and $Y(z_i)$ are only discontinuous in the fifth derivative.

We can now write the quintic splines

$$x_i \simeq a_1 + a_2 z_i + \frac{1}{p} X(z_i) \tag{B-3}$$

and

$$y_i \simeq b_1 + b_2 z_i + \frac{1}{p} Y(z_i) \quad . \tag{B-4}$$

This makes it apparent that the momentum p and the integration constants a_1, a_2, b_1 and b_2 can be determined from a straightforward least squares fit.

The trajectories determined by the "offline"-stage of the analysis sequence were used for initial estimates of x' and y'. If these first estimates were not acceptable, new estimates of x' (and similarly y') can now be formed as follows:

$$x' = a_2 + \frac{1}{p}\int_{z_1}^{z_i} A(v)dv \quad .$$

We then iterate by reapplying equations (B-1)-(B-4) to get new trajectories. We found that 80% of the trajectories converged after two iterations, and all converged within four iterations.

Notice that for the cubic spline fit to A(z), we can call for the magnetic field at more points than have actually been measured in the spark chambers. These extra "imaginary" points are, of course, excluded in the least squares fit to equations (B-3) and (B-4). The extra points can be very useful for extrapolating the track (e.g., to the vertex position) and also in accounting for a field region where no detectors are present.

APPENDIX C

ACCEPTANCE CALCULATION

The cross section had to be corrected for losses due to:

a) the geometry of the detection and triggering apparatus,

b) the triggering constraints, and

c) the geometric and kinematic constraints of Table 6.

These corrections were done using a Monte Carlo simulation program producing events of the form

$$
\begin{array}{lllll}
\pi^- p \to Pn & & & & \\
 & \to V\pi^o & & & \\
 & & \to \gamma\gamma & & \\
 & \to \pi^+\pi^-\pi^o & & & \\
 & & & \to \gamma\gamma & .
\end{array}
$$

Each event was described by four kinematic quantities: the beam momentum, the four-momentum transfer squared, the $(V\pi^o)$ effective mass, and the $(\pi^+\pi^-\pi^o)$ effective mass. We applied the program to our particular decay, $P \to B^o$ and $V \to \omega$, and calculated the acceptance as a function of t.

The B^o and ω masses were generated randomly with Breit-Wigner distributions of widths and masses as given in [4].

The generation of events went as follows: the B^o was made to decay to $\omega\pi^o$ in the B^o rest frame. A right-handed coordinate system was chosen (Figure 25a) such that the z-axis was along the B^o direction in the overall C.M. system, i.e., Helicity frame; y was chosen normal to the production plane, $\bar{y} = (\bar{\pi}_{in} \times \bar{B})$. The B^o mass uniquely determines $|\bar{P}_\omega| = |\bar{P}_{\pi o}|$ and a choice of Φ_ω and $(\cos\Theta)_\omega$ completely specify the four momenta of the ω and π^o .

For the purpose of the Monte Carlo studies we assumed that the $B^o(J^P = 1^+) \rightarrow \omega\pi^o$ decay is uniquely S-wave in generating the appropriate angular distributions in $\cos\Theta$ and Φ . For the case of $J^P = 1^-$, the decay is all P-wave. The distributions for both cases are (Appendix E)

a) 1^+

$$\frac{dW}{d\cos\Theta} = k_1\left[\frac{1 - 3|F_0|^2}{4}(1 - 3\rho_{00})\cos^2\Theta + \tfrac{1}{4}(1 + |F_0|^2 + \rho_{00}(1 - 3|F_0|^2))\right]$$

$$\frac{dW}{d\Phi} = k_2\left[1 + (1 - 3|F_0|^2)\,\rho_{1-1}\cos 2\Phi\right],$$

where $\rho_{\Lambda\Lambda'}$ are density matrix elements and the F_λ are ω "helicity decay amplitudes".

However, 100% S-wave implies $|F_0|^2 = 1/3$ (see (9-5) of Chapter 9) and, therefore,

$$\frac{dW}{d\cos\Theta} = k_1/3 \qquad \text{and} \qquad \frac{dW}{d\Phi} = k_2 \quad .$$

b) 1^-

$$\frac{dW}{d\cos\Theta} = k_3\left[\ |F_1|^2 + \tfrac{3}{2}|F_1|^2\left\{ \frac{P_2(\Theta)}{6} - \rho_{00}\frac{P_2(\Theta)}{2} \right\}\right]$$

$$\frac{dW}{d\Phi} = k_4[\ |F_1|^2 + |F_1|^2\{\ \rho_{1-1}\ \sin 2\Phi\ \}\ ] \ ,$$

where $|F_1|^2 = 1/2$ and $P_2(\Theta) = 3\cos^2\Theta - 1$.

In the case of the B^o , the assumption of 100% S-wave is not completely accurate as we and others [5,6] have found that the intensity of the D-wave is 4-9% that of the S-wave. This error was found to be approximately 5% and was taken into account in the overall error calculation.

Next we considered the ω decay. There are five independent kinematic variables (neglecting spin) needed to describe the 3π decay of the ω . Three variables are needed to describe the orientation of the decay plane (ω rest frame) in space. The kinematics in the decay plane are then parameterized by two more variables. We chose the dipion effective mass, $M_{\pi^+\pi^-}$, and $\hat{p}\cdot\hat{q} = \cos\alpha = \mu$:

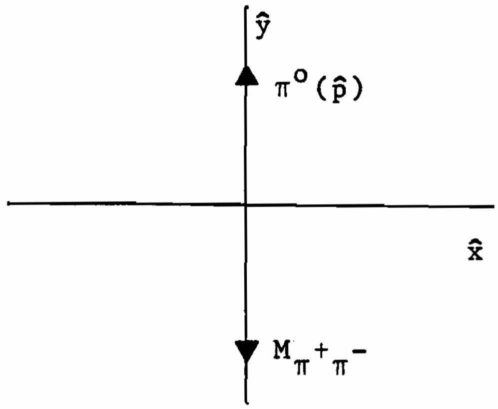

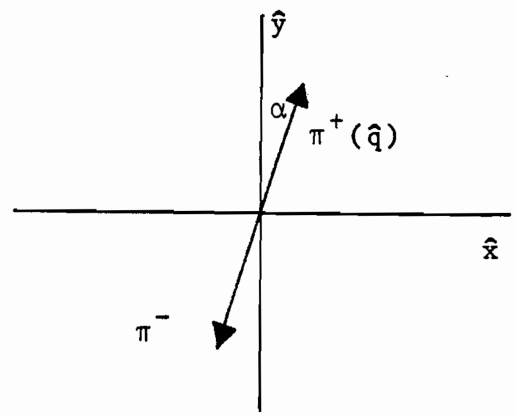

The distribution for these two variables in the decay of a $J^P = 1^-$ particle is given by [7,8]

$$\frac{dN}{dM_{\pi^+\pi^-}} = (F(M_\omega, M_{\pi^+\pi^-}, M_{\pi^0})^3 \times F(M_{\pi^+\pi^-}, M_{\pi^+}, M_{\pi^-})^3)$$

$$= p^3 q^3$$

and

$$\frac{dN}{d\mu} = (1 - \mu^2) \quad ,$$

where

$$F(x,y,z) = \frac{(x^2 - (y+z)^2)^{\frac{1}{2}} (x^2 - (y-z)^2)^{\frac{1}{2}}}{2x} \quad .$$

We now consider the orientation of the 3π decay plane. The ω was made to decay in the ω helicity rest-frame (Figure 25b); i.e., the ω direction was chosen as the z-axis, and the y-axis was chosen along $\bar{z}'\times\bar{z}$ in the B^o rest frame (z' refers to the B^o helicity frame described earlier). The necessary distributions in polar angle $\cos\theta$ and azimuthal angle ϕ are (see Appendix E)

a) 1^+

$$\frac{dW}{d\cos\theta} = k_5[\ 1 + \tfrac{1}{2}(3|F_0|^2 - 1)(3\cos^2\theta - 1)\ ]$$

$$\frac{dW}{d\phi} = k_6[\ 1 + |F_1|^2(3\rho_{00} - 1)\ \cos2\phi\ ]\quad .$$

Since we have $|F_0|^2 = 1/3 = |F_1|^2$,

$$\frac{dW}{d\cos\theta} = k_5$$

$$\frac{dW}{d\phi} = k_6[\ 1 + \tfrac{1}{3}(3\rho_{00} - 1)\ \cos2\phi\ ]\quad .$$

b) 1^-

$$\frac{dW}{d\cos\theta} = k_7\sin^2\theta$$

$$\frac{dW}{d\phi} = k_8\ |F_1|^2[1 + \tfrac{1}{2}(3\rho_{00} - 1)\ \cos2\phi\ ]\quad .$$

After a complete event was generated, it was rotated to an arbitrarily chosen production plane and transformed to the laboratory frame. The production plane was then randomly rotated about z (the beam direction) and the π^0's allowed to decay uniformly in their respective rest frames. The geometric and kinematic constraints of Table 6 were applied, and events failing the cuts were deleted. Then the two following trigger constraints were checked:

a) a unique PWC strip was set for each charged particle;

b) a unique H2 hodoscope element was set for each charged particle.

Events were also rejected statistically to account for decays of the charged pions in flight, and interactions and conversions of the particles in the hydrogen target:

a) <u>Charged Pion Decay in Flight</u>

The probability of decay is

$$\frac{\text{(distance in inches from target to last chamber)}}{\beta\times(307.2)} .$$

b) π^+, π^- Interactions in Target

The probability of interaction is

(path length in hydrogen target in inches)×.00325 ,

assuming an interaction cross-section of 30 mb.

c) Conversion of Gammas in Target

The probability of conversion is

(path length in hydrogen in inches)×.00198 ,

assuming a scaling of the thickness by .69 radiation lengths.

The final acceptance was the fraction surviving all the cuts and deletions. As a check on our understanding of the acceptance, we plotted the magnitude of the momentum of various particles; first, as predicted by Monte Carlo simulation, and then as obtained from our data (see Figure 40). We have good agreement in all cases.

Our acceptance is tabulated as a function of t', in Table 7, and plotted in Figure 20.

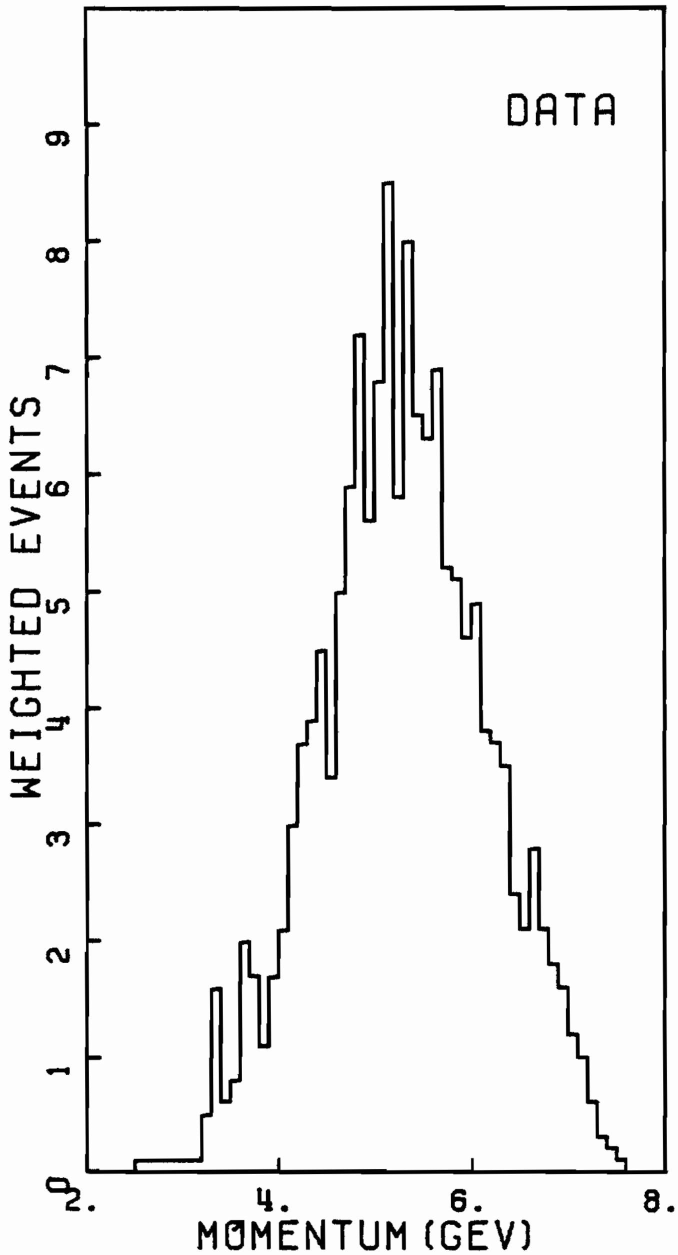

FIGURE 40a P_{ω} Data

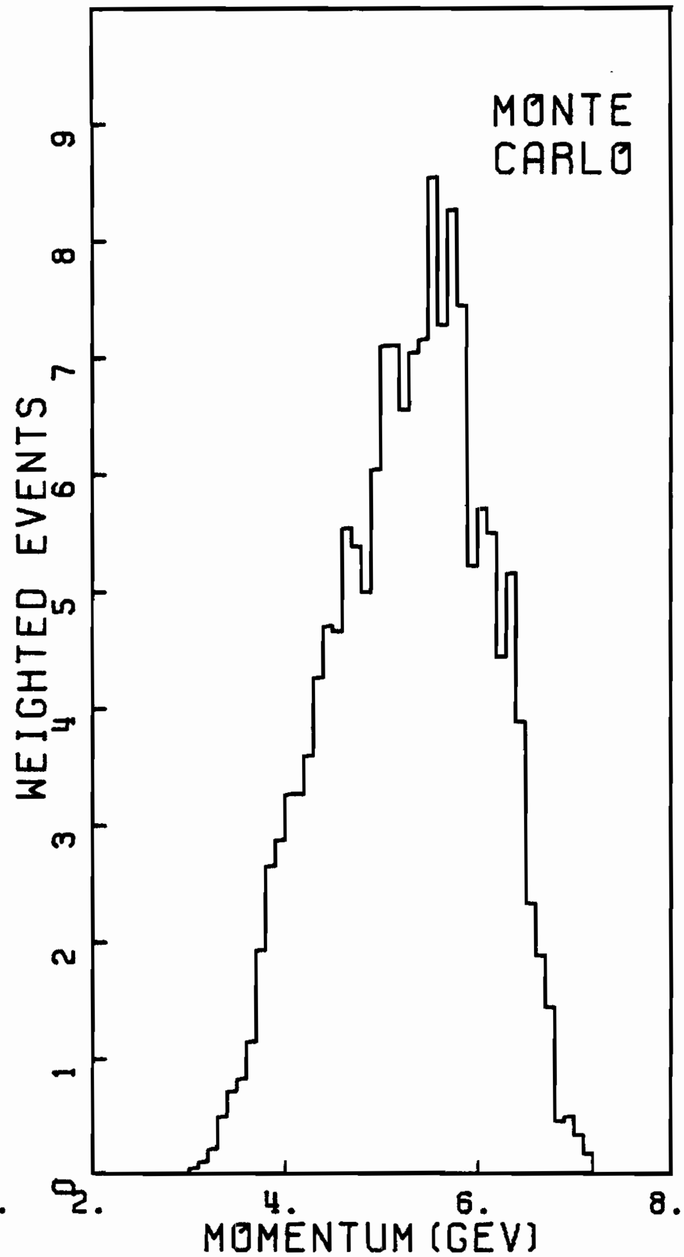

FIGURE 40b P_{ω} Monte Carlo

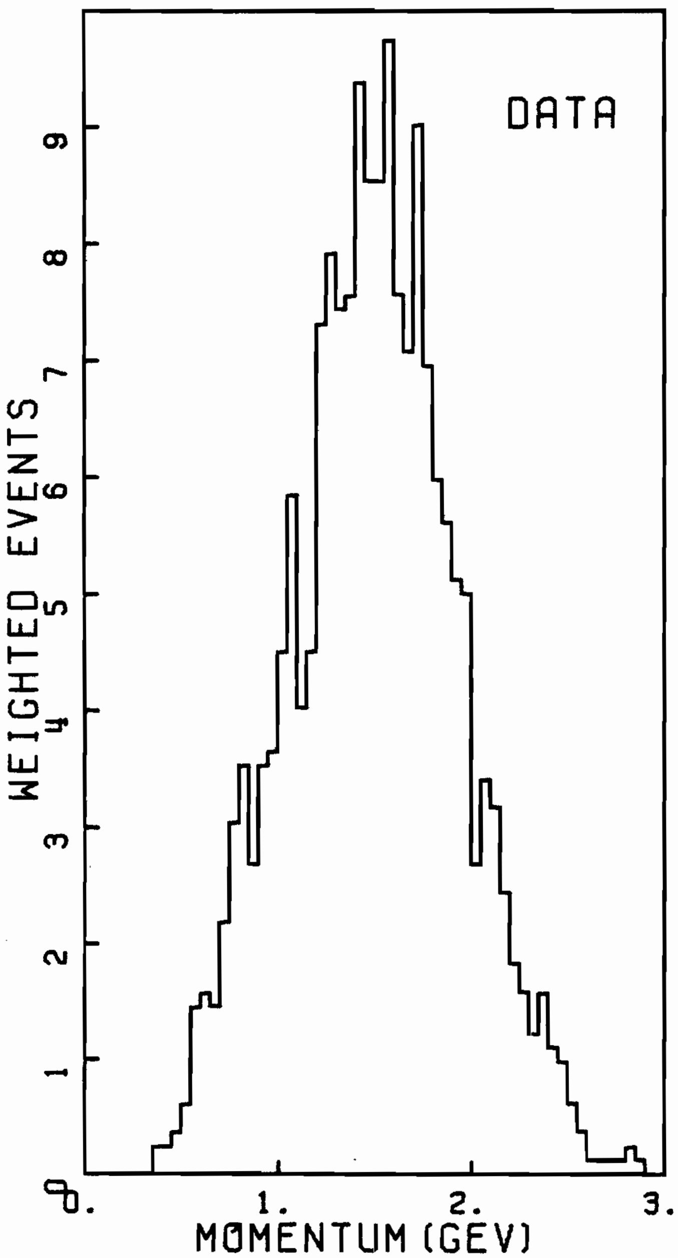

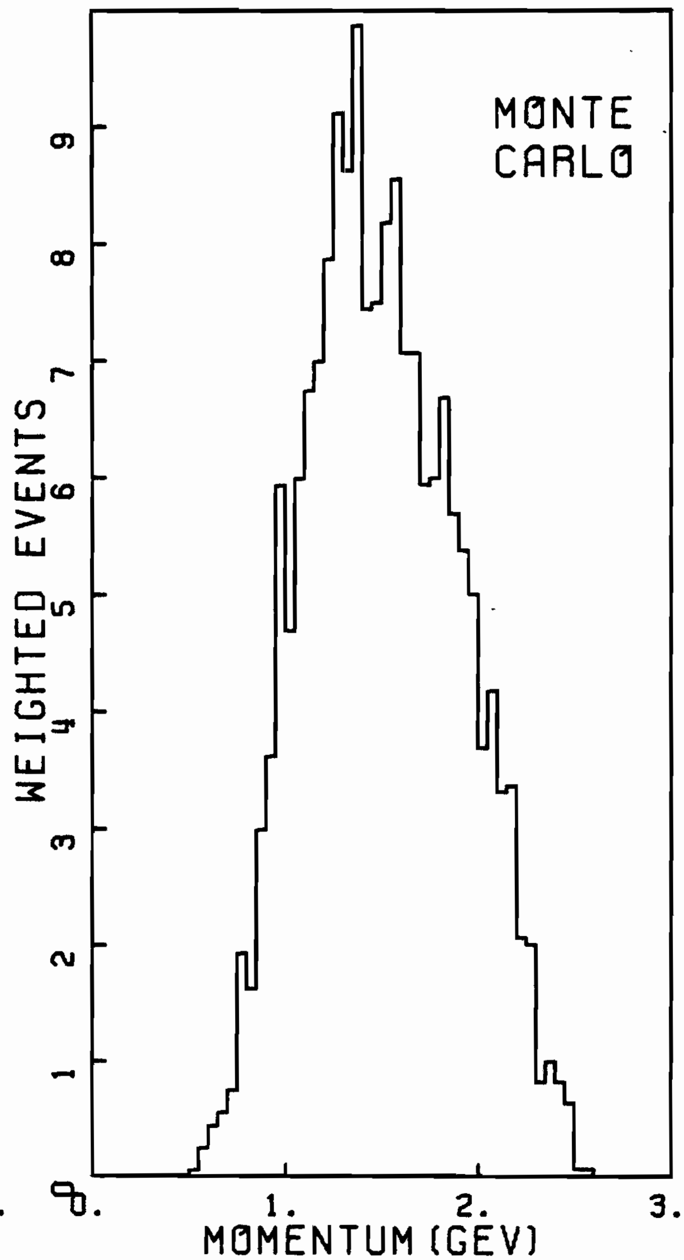

FIGURE 40c $P_{\pi^0(2)}$ Data

FIGURE 40d $P_{\pi^0(2)}$ Monte Carlo

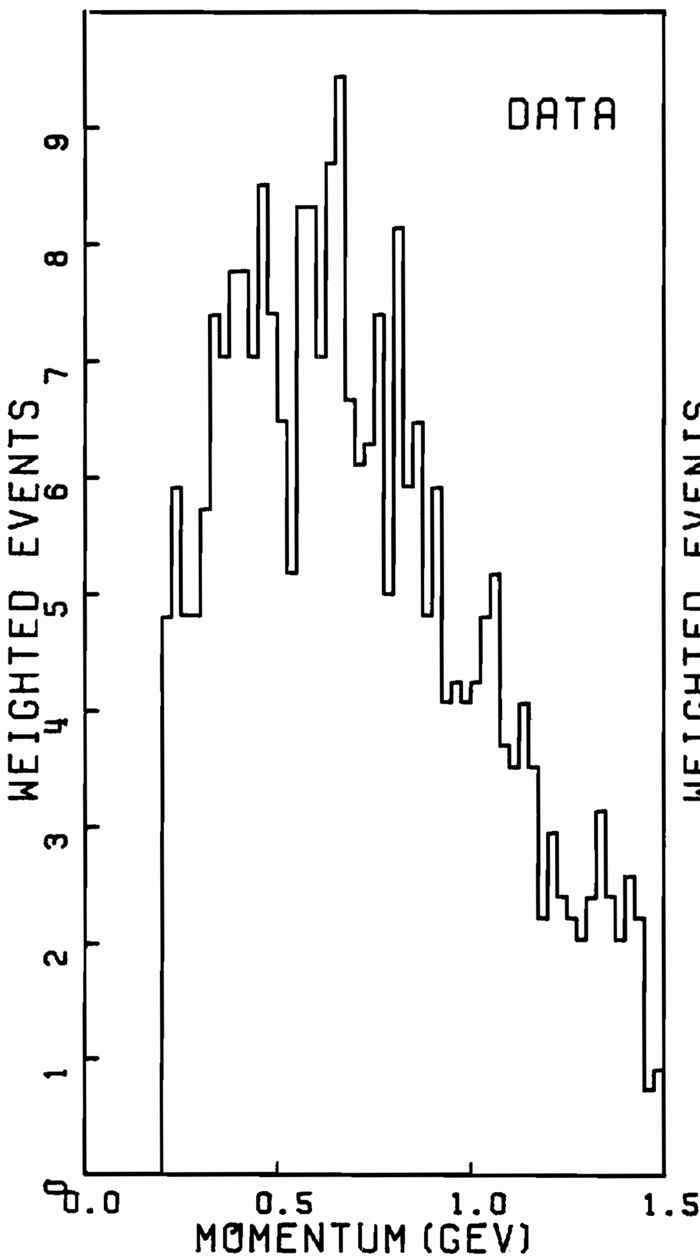

FIGURE 40e P_{π^+} Data

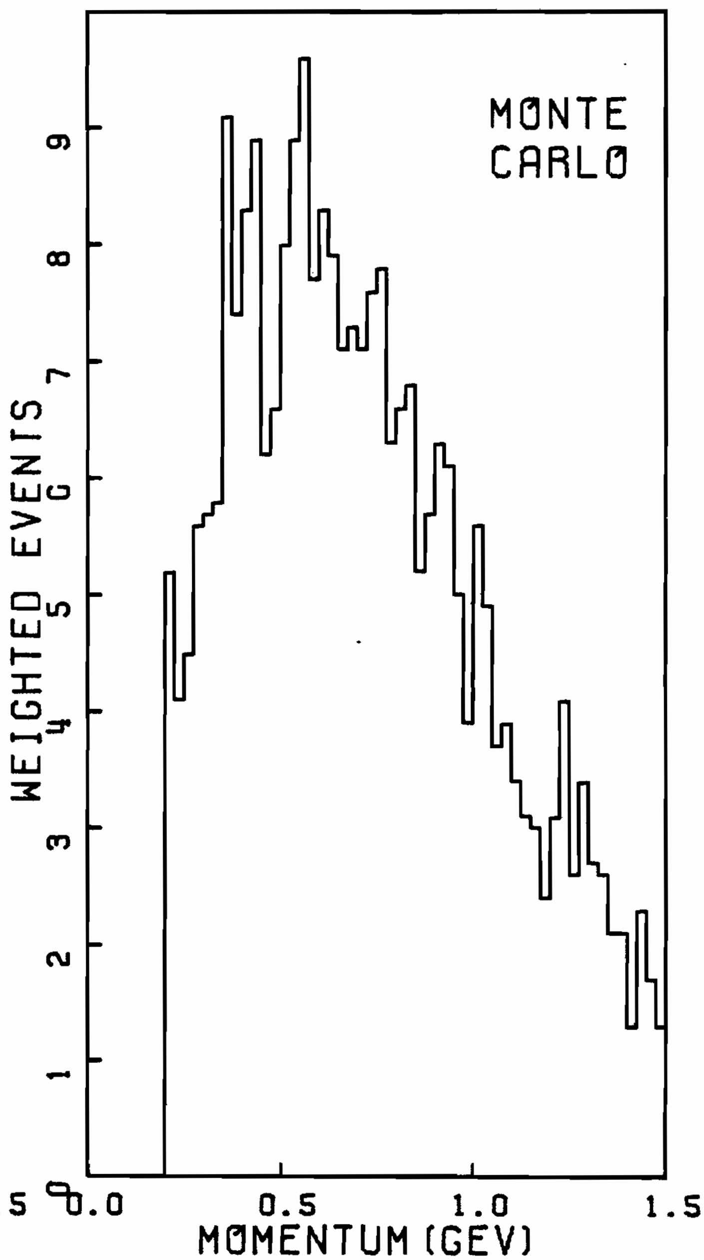

FIGURE 40f P_{π^+} Monte Carlo

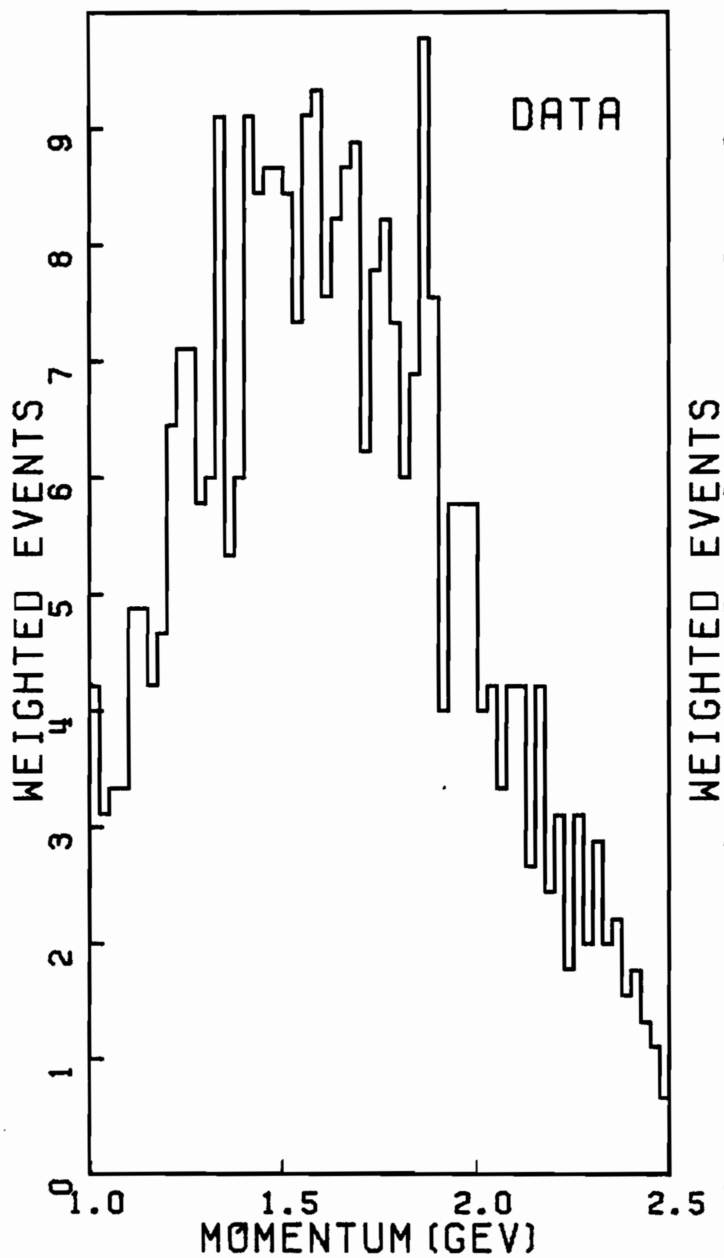

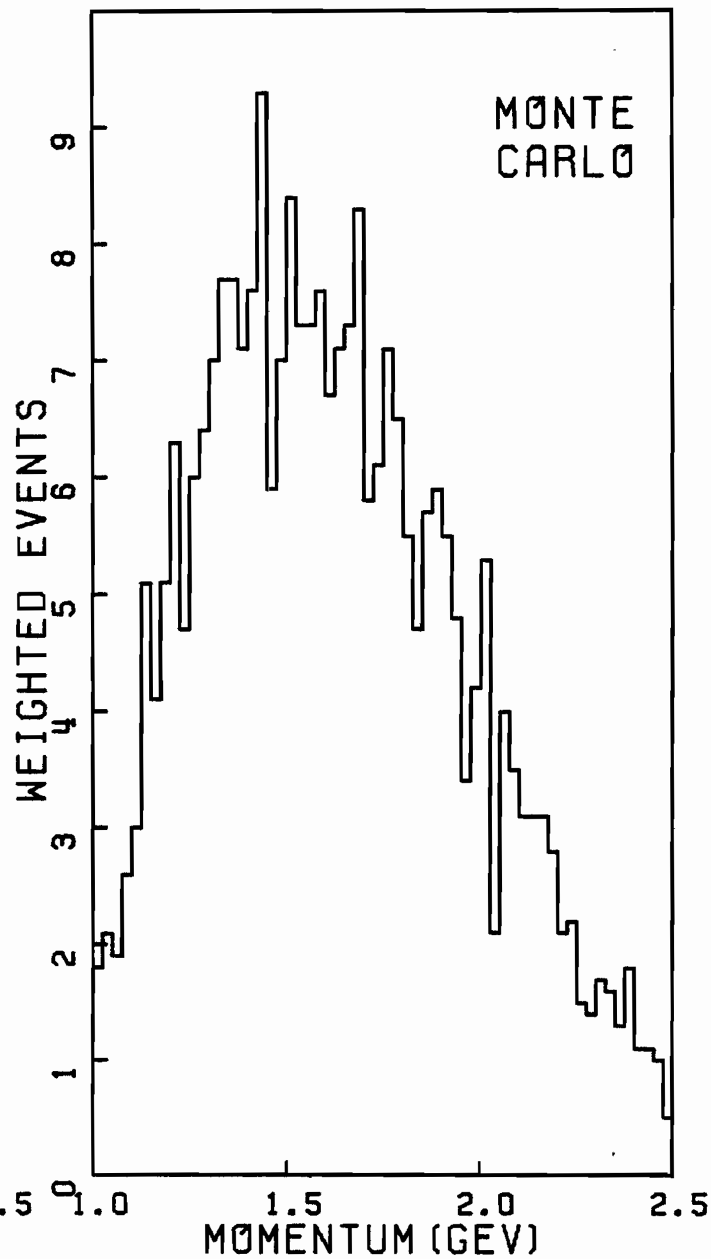

FIGURE 40g $P_{\pi^0\omega}$ Data

FIGURE 40h $P_{\pi^0\omega}$ Monte Carlo

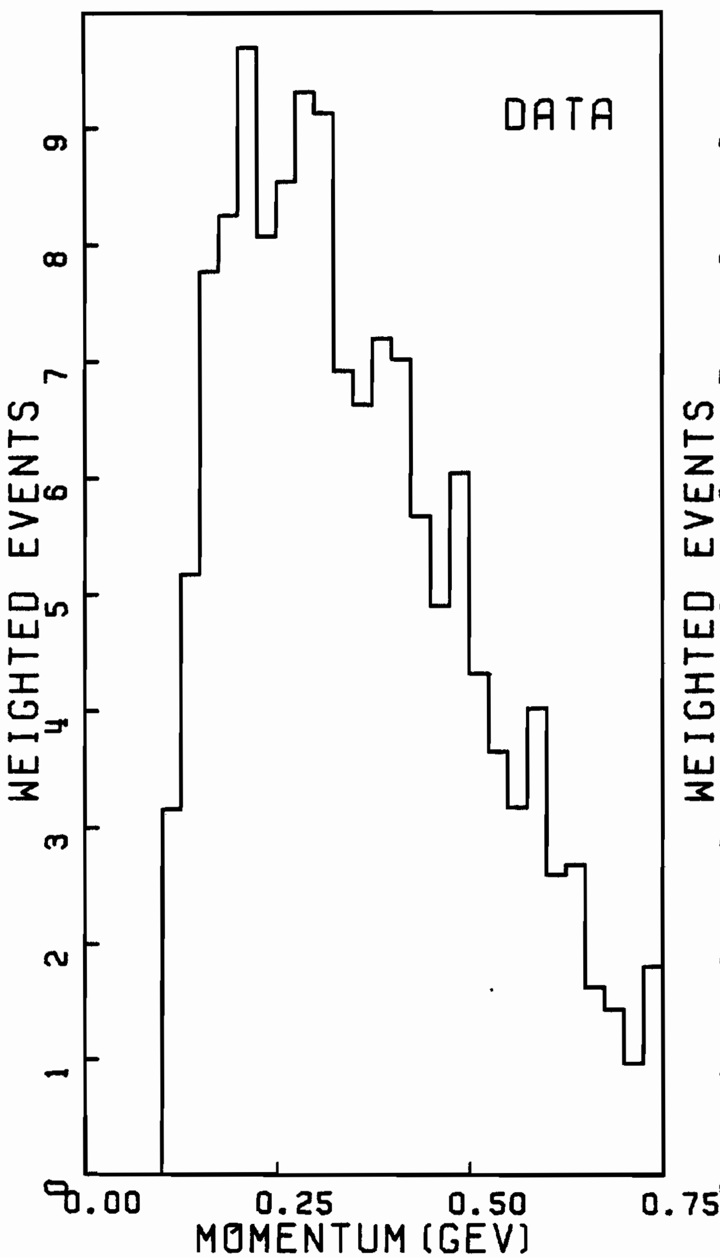

FIGURE 40i P_{γ_2} Data

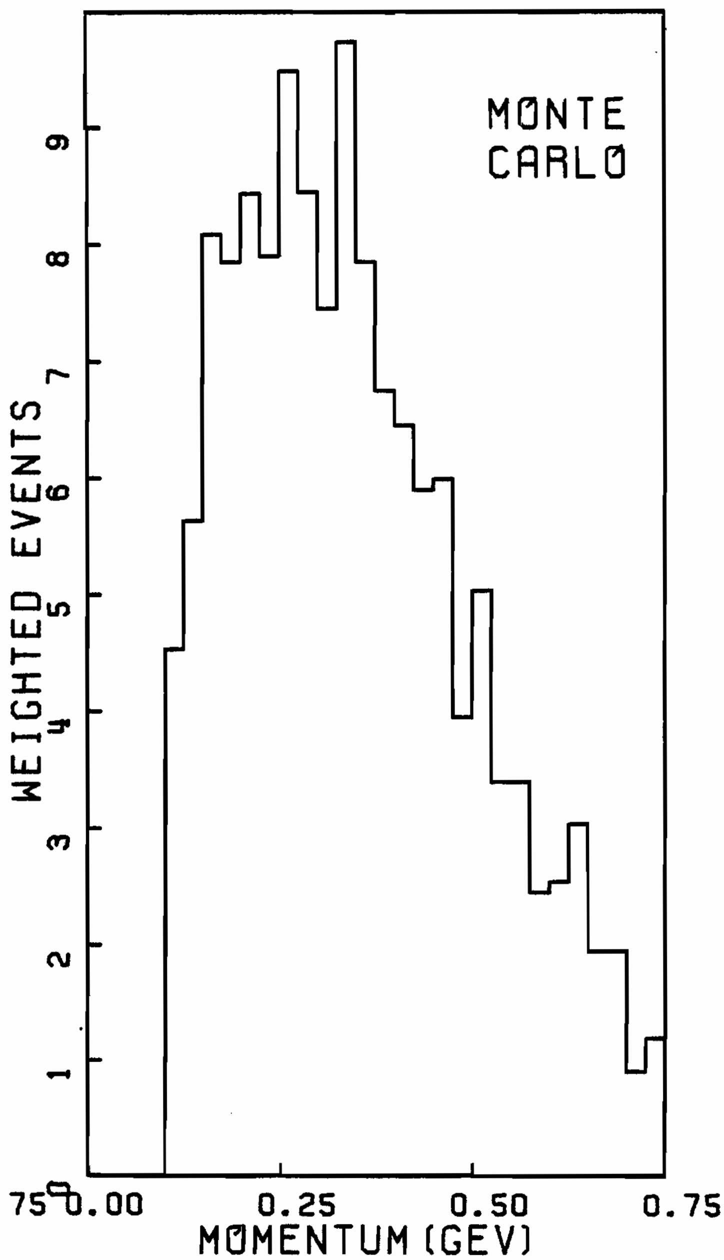

FIGURE 40j P_{γ_2} Monte Carlo

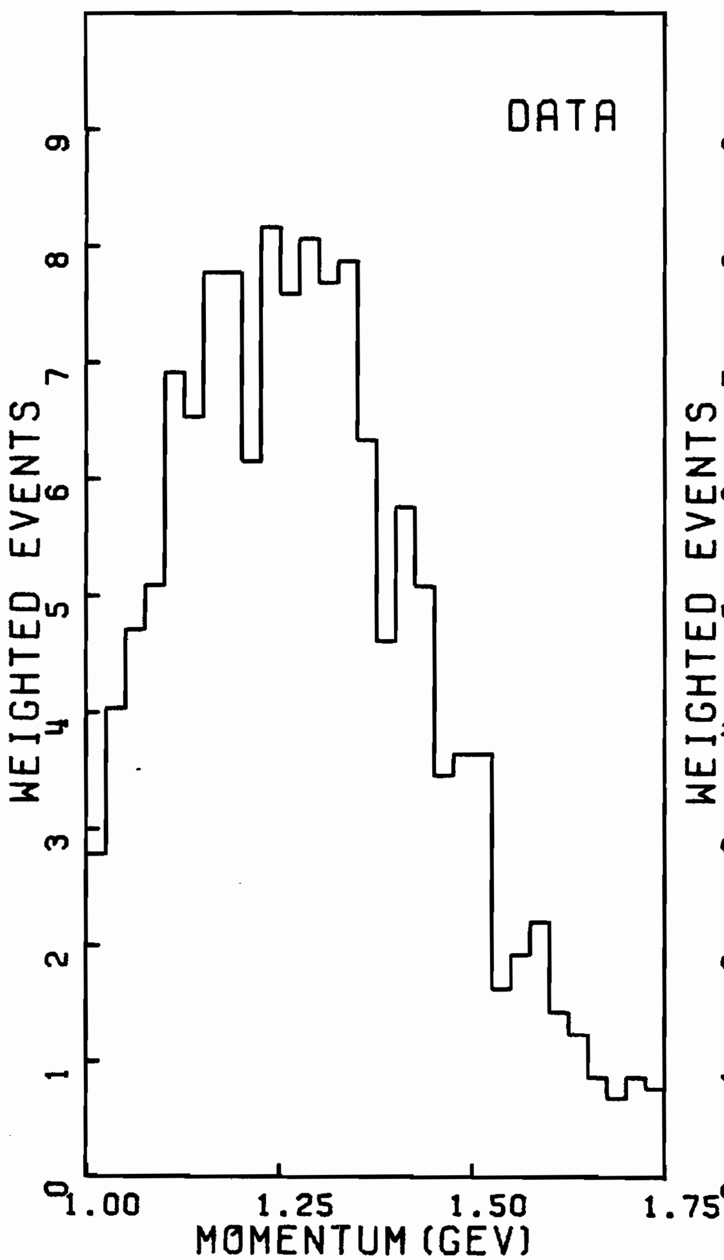

FIGURE 40k P_{γ_3} Data

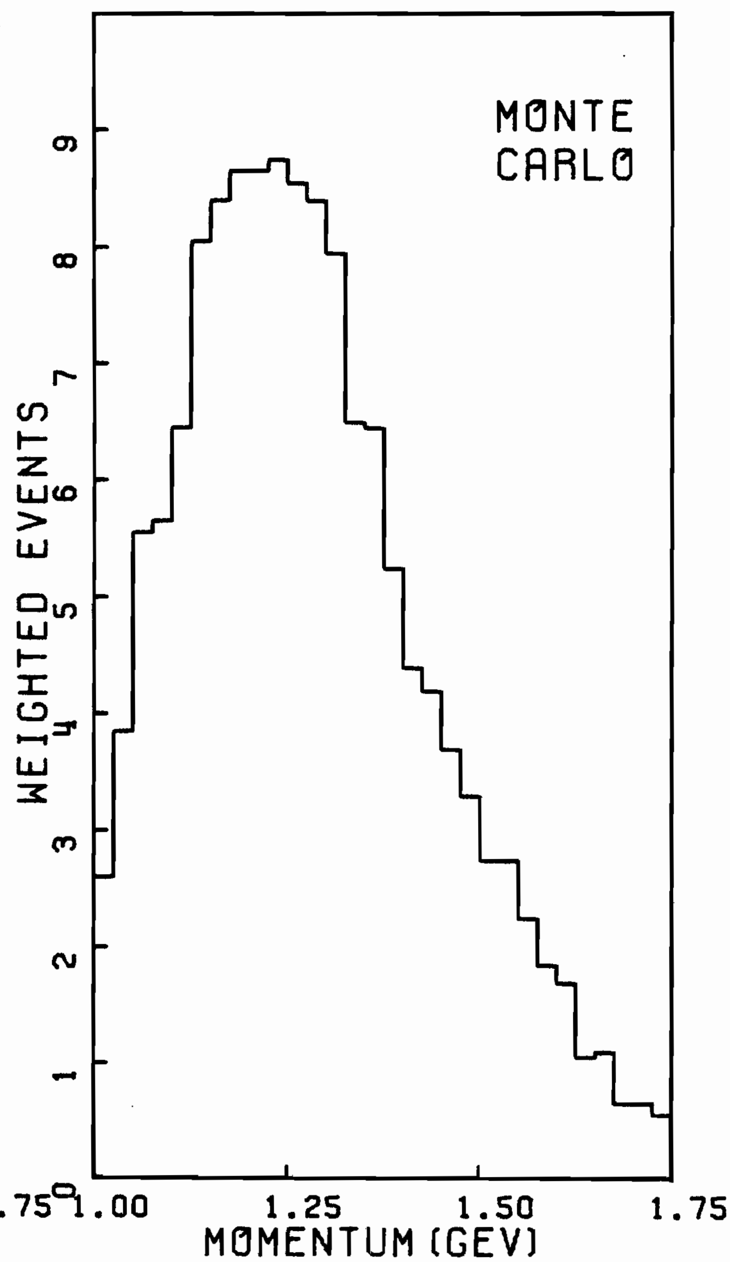

FIGURE 40l P_{γ_3} Monte Carlo

APPENDIX D

GAMMA SHOWER CHAMBER EFFICIENCY CALCULATION

In the gamma system there were two views - plan X and elevation Y - each having three planes. We label the three X planes 1, 2 and 3, and the three Y planes 4, 5 and 6. A shower was accepted if one view had at least two planes firing, and the other view had at least one plane firing.

We make the following definitions:

$$\varepsilon_i = \text{efficiency of chamber plane } i$$

$$= \frac{\text{number of times the plane contained a spark}}{\text{number of tracks through the chamber}} \; ,$$

$$P_i = \text{participation ratio of plane } i \text{ for a found event}$$

$$= \frac{\text{number of times the plane fired in a found event}}{\text{number of found events}} \; .$$

Then the probability $P(\geq 2)$ of at least two of the three planes in one view firing is given by

$$P(\geq 2) = \varepsilon_i\varepsilon_j(1-\varepsilon_k) + \varepsilon_i(1-\varepsilon_j)\varepsilon_k + (1-\varepsilon_i)\varepsilon_j\varepsilon_k + \varepsilon_i\varepsilon_j\varepsilon_k$$

$$= \varepsilon_i\varepsilon_j + \varepsilon_i\varepsilon_k + \varepsilon_j\varepsilon_k - 2\varepsilon_i\varepsilon_j\varepsilon_k \; , \qquad \text{(D-1)}$$

$$(i,j,k) = (1,2,3) \text{ or } (4,5,6) \; .$$

Therefore the probability P_γ of finding a shower, when one is present, can easily be found to be

$$P_\gamma = P_x(\geq 2) \times P_y(\geq 2) \tag{D-2}$$

$$+ P_x(\geq 2) \times (\varepsilon_4(1-\varepsilon_5)(1-\varepsilon_6) + \varepsilon_5(1-\varepsilon_4)(1-\varepsilon_6))$$

$$+ P_y(\geq 2) \times (\varepsilon_1(1-\varepsilon_2)(1-\varepsilon_3) + \varepsilon_2(1-\varepsilon_1)(1-\varepsilon_3)) \ .$$

We can now write expressions for the participation ratios, using the definition for P_i and the expressions (D-1) and (D-2). For the X view,

$$\frac{P_1}{\varepsilon_1} = \frac{P_y(\geq 2) + (\varepsilon_2+\varepsilon_3-\varepsilon_2\varepsilon_3) \times (\varepsilon_4(1-\varepsilon_5)(1-\varepsilon_6) + \varepsilon_5(1-\varepsilon_4)(1-\varepsilon_6))}{P_\gamma} \tag{D-3}$$

$$\frac{P_2}{\varepsilon_2} = \frac{P_y(\geq 2) + (\varepsilon_1+\varepsilon_3-\varepsilon_1\varepsilon_3) \times (\varepsilon_4(1-\varepsilon_5)(1-\varepsilon_6) + \varepsilon_5(1-\varepsilon_4)(1-\varepsilon_6))}{P_\gamma} \tag{D-4}$$

$$\frac{P_3}{\varepsilon_3} = \frac{P_y(\geq 2) \times (\varepsilon_1+\varepsilon_2-\varepsilon_1\varepsilon_2)}{P_\gamma} \ . \tag{D-5}$$

Identical expressions hold for the planes of the second view under the exchange $(1,2,3) \longleftrightarrow (4,5,6)$.

To calculate the single shower efficiency P_γ, we needed the efficiencies ε_i, given the P_i from the recorded data. This was done by solving for ε_i in (D-2) - (D-5) using an iterative procedure. The starting values for ε_i on the right-hand-sides of (D-3) - (D-5) were taken as the P_i . A new set of ε_i were found and the process was repeated until stable results were reached, usually after only a few iterations. The single shower efficiency was obtained by substituting these final chamber efficiencies into (D-2), and the four gamma shower efficiencies easily followed.

APPENDIX E

SEQUENTIAL DECAY ANALYSIS

The purpose of this appendix is to describe the production and the sequential decay of the $\omega\pi^o$ system, and to derive the expression for the angular distribution of its decay products. We adopt the helicity formalism used by Chung [24] and others [5,26,27].

We wish to describe the following chain of processes:

$a + b \rightarrow c + J$		$\pi^- + p \rightarrow n + B^o$	
$J \rightarrow s + \pi_1$	or, more specifically,	$B^o \rightarrow \omega + \pi^o$	(E-1)
$s \rightarrow s_1 + \pi_2$		$\omega \rightarrow \pi^+ + \pi^- + \pi^o$.	

Note that $\omega \rightarrow \pi^+\pi^-\pi^o$ can be treated in the same way as the case of $\rho^o \rightarrow \pi^+\pi^-$ [24] by simply using the normal to the decay plane of the $\omega(\cos\theta_N,\phi_N)$ as the analyser instead of the relative momentum of the $s \rightarrow s_1 + \pi_2$ decay. The following notation will be used:

J	spin of resonance J
η	parity of resonance J
Λ	helicity of resonance J
w	mass of resonance J
s	spin of resonance s

η_s	parity of resonance s
λ	helicity of resonance s
w_s	mass of resonance s
s_1	spin of resonance s_1
η_1	parity of resonance s_1
λ_1	helicity of resonance s_1
w_1	mass of resonance s_1
JRF	rest frame of resonance J
SRF	rest frame of resonance s
p_s	momentum of s in the JRF
$\Omega(\cos\Theta,\Phi)$	direction of s in the JRF
p_1	momentum of s_1 in the SRF
$\Omega_1(\cos\theta,\phi)$	direction of s_1 in the SRF

Since helicity frames of reference are used throughout the analysis, we have the following convention: Θ and Φ are the polar and azimuthal angles, respectively, of the ω (or s) resonance in the B^o (or J) rest frame. A right-handed coordinate system is chosen so that the z-axis is along the B^o direction in the overall C.M. system; i.e., B^o helicity frame. y is normal to the production plane, $\bar{y} = (\bar{a}_{in} \times \bar{J})$; θ and ϕ are the polar and azimuthal angles, respectively, of the normal to the ω decay plane in the ω(or s) rest frame, measured in a system x', y', z', where $\bar{z}' = \bar{p}_\omega$ (or $\bar{p}_s$) and $\bar{y}' = \bar{z} \times \bar{z}'$ (in the JRF). This is the ω helicity frame (see Figure 25). Simply put, the ω helicity frame can be obtained from the B^o helicity frame by means of an Euler transformation with angles $\alpha = \Theta$, $\beta = \Phi$ and $\gamma = 0$.

The overall invariant amplitude for the process (E-1) can now be written as

$$M_{fi} \sim \langle \Omega_1 s_1 \lambda_1 | M_s | s\lambda \rangle \langle \Omega s \lambda | M_J | J\Lambda \rangle \langle \bar{p}_f \lambda_c \Lambda | T(w_0) | \bar{p}_i \lambda_a \lambda_b \rangle \ , \tag{E-2}$$

where $\bar{p}_i$ = C.M. momentum of particle a,

$\bar{p}_f$ = C.M. momentum of particle c,

w_0 = C.M. energy

and λ_a = helicity of particle a, etc.

The first and second factors describe the s and J decay, respectively, and the third factor is the production amplitude for the J.

The differential cross-section in the decay angles $\Omega = (\Theta,\Phi)$ and $\Omega_1 = (\theta,\phi)$ may be expressed, after summing over all other variables except Ω and Ω_1 as

$$\frac{d\sigma}{d\Omega d\Omega_1} \sim \int k(w,w_s) \sum |M_{fi}|^2 \, d\Omega^o d\Omega_1^o dw dw_s \ , \tag{E-3}$$

where M_{fi} is given by (E-2) and $k(w,w_s)$ is a factor which includes all quantities dependent on w and w_s, such as the phase space factors and the Breit-Wigner functions of the resonances J and s.

The amplitude describing the decay of spin J with helicity Λ can be rewritten as

$$4\pi\left(\frac{w}{p}\right)^{\frac{1}{2}} \langle \Omega s\lambda | J\Lambda\lambda' \rangle \langle J\Lambda\lambda' | M_J | J\Lambda \rangle$$

$$= N_J F^J_\lambda D^{J*}_{\Lambda\lambda}(\Omega) \quad . \tag{E-4}$$

The "helicity decay amplitude" F is given by

$$F^J_\lambda = 4\pi\left(\frac{w}{p}\right)^{\frac{1}{2}} \langle J\Lambda\lambda | M_J | J\Lambda \rangle$$

and is normalized so that $\sum_\lambda |F^J_\lambda|^2 = 1$. $D^J(\Omega)$ is the standard rotation matrix as given by Rose [28] . We adopt the notation $D^J(\Omega) = D^J(\phi,\theta,0)$. Similarly, the amplitude of the decay of the s resonance is given by

$$N_s F^s_{\lambda_1} D^{s*}_{\lambda\lambda_1}(\Omega_1) \quad . \tag{E-5}$$

We now introduce the spin density matrix corresponding to the resonance J:

$$\rho^J_{\Lambda\Lambda'} \sim \int \sum \langle \bar{p}_f \lambda_c \Lambda | T(w_0) | \bar{p}_i \lambda_a \lambda_b \rangle \tag{E-6}$$

$$\langle \bar{p}_f \lambda_c \Lambda' | T(w_0) | \bar{p}_i \lambda_a \lambda_b \rangle^* \, d\Omega^o d\Omega^o_1 \quad ,$$

where the summation sign denotes the sum over λ_a, λ_b and λ_c. The $\rho_{\Lambda\Lambda}$ are normalized so that $\sum_\Lambda \rho_{\Lambda\Lambda} = 1$.

Inserting (E-4), (E-5) and (E-6) into (E-3), we obtain

$$\frac{d\sigma}{d\Omega d\Omega_1} \sim N_J^2 N_s^2 \int \sum_{\substack{\Lambda'\Lambda \\ \lambda\lambda'\lambda_1}} F_\lambda^J \; F_{\lambda'}^{J*} \; D_{\Lambda'\lambda'}^{J*}(\Omega) \; D_{\Lambda\lambda}^{J}(\Omega) \; F_{\lambda_1}^{s*} \; F_{\lambda_1}^{s}$$

$$D_{\lambda'\lambda_1}^{s*}(\Omega_1) \; D_{\lambda\lambda_1}^{s}(\Omega_1) \; \rho_{\Lambda\Lambda'}^{J} \; k(w,w_s) \; dw dw_s \quad .$$

At this point, we introduce some simplifying assumptions. First, demand that $\rho_{\Lambda\Lambda'}^{J}$ be independent of w over the width of the resonance J (or over the width of the mass bin being considered). This assumption makes the resulting formalism much simpler. It can be shown that a more general formalism, without this simplifying assumption, leads to identical results for the case of the $B^o(1235)$ meson (see Chung [29]). Next, neglect the width of the s (or ω) resonance; then, $F_{\lambda_1}^{s}$ can be considered constant and F_λ^J can be factored out of the dw integral. Hence, we can write

$$I(\Omega,\Omega_1) = \left(\frac{2J+1}{4\pi}\right) \left(\frac{2s+1}{4\pi}\right) \sum_{\substack{\Lambda\Lambda' \\ \lambda\lambda'\lambda_1}} \rho_{\Lambda\Lambda'}^{J} \; |F_\lambda^J|^2 \tag{E-7}$$

$$D_{\Lambda'\lambda'}^{J*}(\Omega) \; D_{\Lambda\lambda}^{J}(\Omega) \; D_{\Lambda'\lambda_1}^{s*}(\Omega_1) \; D_{\lambda\lambda_1}^{s}(\Omega_1) \quad ,$$

where $I(\Omega,\Omega_1)$ denotes the normalized angular distribution; i.e.,

$$\int I(\Omega,\Omega_1)\; d\Omega d\Omega_1 = 1 \quad .$$

For the particular case of the process (E-1), we have $s = 1$, $\lambda_1 = 0$. Therefore, (E-7) becomes

$$I(\Omega,\Omega_1) = \frac{3(2J+1)}{16\pi^2} \sum_{\substack{\Lambda\Lambda' \\ \lambda\lambda'}} \rho^J_{\Lambda\Lambda'} |F^J_\lambda|^2 \; D^{J*}_{\Lambda'\lambda'}(\Phi,\Theta,0)$$

$$D^J_{\Lambda\lambda}(\Phi,\Theta,0)\; D^{1*}_{\lambda'0}(\phi,\theta,0)\; D^1_{\lambda 0}(\phi,\theta,0) \quad .$$

Since the angle ϕ is the same in both systems, its dependence can be shifted to the first D-function. This can be seen from the definition of the D-functions given by Rose [28] i.e.,

$$D^j_{m'm}(\alpha,\beta,\gamma) = e^{-im'\alpha}\; d^j_{m'm}(\beta)\; e^{-im\gamma} \quad .$$

Using this and the relation [28]

$$D^{j*}_{m'm}(\alpha,\beta,\gamma) = (-1)^{m'-m}\; D^j_{-m',-m}(\alpha,\beta,\gamma) \quad ,$$

we obtain

$$I(\Omega,\Omega_1) = \frac{3(2J+1)}{16\pi^2} \sum_{\substack{\Lambda\Lambda' \\ \lambda\lambda'}} \rho^J_{\Lambda\Lambda'} \, |F^J_\lambda|^2 \, (-1)^{\Lambda-\lambda} \, (-1)^\lambda$$

$$D^J_{-\Lambda,-\lambda}(\Phi,\Theta,\phi) \, D^J_{\Lambda',\lambda'}(\Phi,\Theta,\phi) \, d^1_{-\lambda,0}(\theta) \, d^1_{\lambda',0}(\theta) \quad .$$

Finally, the coupling rule for D-functions,

$$D^{j_1}_{\mu_1 m_1} \, D^{j_2}_{\mu_2 m_2} = \sum_{j_3\mu_3 m_3} (j_1\mu_1 j_2\mu_2|j_3\mu_3)$$

$$(j_1 m_1 j_2 m_2|j_3 m_3) \, D^{j_3}_{\mu_3 m_3} \quad ,$$

gives our angular distribution

$$I(\Omega,\Omega_1) = \frac{d^4N}{d\cos\Theta d\cos\theta d\Phi d\phi} \tag{E-8}$$

$$= \frac{3(2J+1)}{16\pi^2} \sum_{\substack{L\Lambda\Lambda' \\ \lambda\lambda'}} (-1)^\Lambda \rho^J_{\Lambda\Lambda'} \, F^J_\lambda \, F^{J*}_{\lambda'}$$

$$(J,-\Lambda,J,\Lambda'|L,\Lambda'-\Lambda) \, (J,-\lambda,J,\lambda'|L,\lambda'-\lambda)$$

$$D^L_{\Lambda'-\Lambda,\lambda'-\lambda}(\Phi,\Theta,\phi) \, d^1_{-\lambda 0}(\theta) \, d^1_{\lambda' 0}(\theta) \quad ,$$

where $L = 0,\ldots,2J,$

$\Lambda = \pm J, \pm(J-1),\ldots,0$

and $\lambda = \pm 1, 0.$

Out of a possible 81 terms, only 9 have nonzero Clebsch-Gordan coefficients for L=0. The L=1 factor has 36 nonzero terms and the L=2 factor consists of all 81 possible terms. It is also possible to make use of symmetry relations to reduce the complexity of the expansion of (E-8). Parity conservation in the decay of the $\omega\pi$ system leads to

$$F_{\lambda} = \varepsilon F_{-\lambda} \qquad \text{and} \qquad \varepsilon = \eta(-1)^{J-1} \quad , \tag{E-9}$$

where η = parity of resonance J.

The density matrix is hermitian by definition (see (E-6)). This implies that $\rho_{m,k} = \rho^{*}_{k,m}$ and $\rho_{m,m}$ is real-valued. The trace condition $\sum_{m}\rho_{m,m} = 1$ also holds. Parity conservation in the process $\pi^{-}p \rightarrow B^{o}N$, together with our choice of coordinate system (i.e., the helicity frame), implies [30] that $\rho_{m,m'} = (-1)^{m-m'}\rho_{-m,-m'}$. The above three conditions (hermiticity, unit trace and parity conservation) reduce the number of free parameters in the density matrix to four; they are ρ_{00}, ρ_{1-1}, Re[ρ_{10}] and Im[ρ_{10}]. Note that Im[ρ_{10}] is related to the vector polarization of the particle along the production normal and cannot be determined in parity-conserving decays [30].

We can now expand (E-8). For J = 1 and η = (+1), (E-9) gives $F_{1} = +F_{-1}$. Therefore,

$$I(\Omega,\Omega_1) = \frac{9}{16\pi^2}\left[\frac{1}{3}F_0^2\cos^2\theta + \frac{1}{3}F_1^2\sin^2\theta\right]$$

(L = 0 contribution)

$$+ \frac{9}{8\sqrt{2}\pi^2}\,\mathrm{Re}[F_0F_1^*]\,\sin\theta\cos\theta$$

$$\left[\frac{1}{\sqrt{2}}\sin\Theta\cos\Theta\cos\phi - \frac{3}{\sqrt{2}}\rho_{00}\sin\Theta\cos\Theta\cos\phi\right.$$

$$- \frac{1}{\sqrt{2}}\rho_{1-1}\left\{\cos(2\Phi + \phi)(1 + \cos\Theta)\sin\Theta\right.$$

$$\left. - \cos(2\Phi - \phi)(1 - \cos\Theta)\sin\Theta\right\}$$

$$+ \mathrm{Re}[\rho_{10}]\left\{(1 - \cos\Theta)(2\cos\Theta + 1)\cos(\Phi - \phi)\right.$$

$$\left.\left. - (1 + \cos\Theta)(2\cos\Theta - 1)\cos(\Phi + \phi)\right\}\right]$$

(E-10)

$$+ \frac{9}{32\pi^2}|F_1|^2\sin^2\theta$$

$$\left[\frac{1}{6}(3\cos^2\Theta - 1) - \frac{1}{2}\cos2\phi\sin^2\Theta\right.$$

$$+ \rho_{00}\left\{\frac{3}{2}\cos2\phi\sin^2\Theta - \frac{1}{2}(3\cos^2\Theta - 1)\right\}$$

$$+ \rho_{1-1}\left\{\cos2\Phi\sin^2\Theta - \frac{1}{2}\cos(2\Phi + 2\phi)(1 + \cos\Theta)^2\right.$$

$$- \frac{1}{2} \cos(2\Phi - 2\phi)(1 - \cos\Theta)^2 \Big\}$$

$$+ \mathrm{Re}[\rho_{10}] \Big\{ 2\sqrt{2} \cos\Phi \sin\Theta \cos\Theta$$

$$+ \sqrt{2} \cos(\Phi + 2\phi)(1 + \cos\Theta)\sin\Theta$$

$$- \sqrt{2} \cos(\Phi - 2\phi)(1 - \cos\Theta)\sin\Theta \Big\} \Big]$$

$$+ \frac{9}{16\pi^2} |F_0|^2 \cos^2\theta$$

$$\Big[- \frac{1}{6} (3\cos^2\Theta - 1) + \frac{\rho_{00}}{2} (3\cos^2\Theta - 1)$$

$$- \rho_{1-1} (\sin^2\Theta \cos 2\Phi) - 2\sqrt{2}\, \mathrm{Re}[\rho_{10}] (\sin\Theta\cos\Theta\cos\Phi) \Big].$$

(L = 2 contribution)

We can integrate the above result to get the following angular distributions:

$$\frac{dN}{d\cos\Theta} = k_1 \Big\{ \frac{1 - 3|F_0|^2}{4} (1 - 3\rho_{00}) \cos^2\Theta$$

$$+ \frac{1}{4} [1 + |F_0|^2 + \rho_{00} (1 - 3|F_0|^2)] \Big\}$$

$$\frac{dN}{d\Phi} = k_2\{ 1 + (1 - 3|F_0|^2)\ \rho_{1-1} \cos 2\Phi \}$$

$$\frac{dN}{d\cos\theta} = k_3\{ 1 + \frac{1}{2} (3|F_0|^2 - 1)(3\cos^2\theta - 1) \} \quad \text{(E-11)}$$

$$\frac{dN}{d\phi} = k_4\{ 1 + |F_1|^2 (3\rho_{00} - 1) \cos 2\phi \}.$$

For $J = 1$ and $\eta = (-1)$, we have $F_1 = -F_1$ and $F_0 = 0$. Since $\sum_\lambda |F_\lambda|^2 = 1$, this implies $F^2_{\pm 1} = \frac{1}{2}$. Therefore,

$$I(\Omega,\Omega_1) = \frac{9}{16\pi^2} \left[\frac{1}{3} |F_1|^2 \sin^2\theta \right]$$

(L = 0 contribution)

$$+ \frac{9}{32\pi^2} |F_1|^2 \sin^2\theta$$

$$\left[\frac{1}{6} (3\cos^2\Theta - 1) + \frac{1}{2} \cos 2\phi \sin^2\Theta \right.$$

(E-12)

$$- \frac{\rho_{00}}{2} \{ (3\cos^2\Theta - 1) + 3\cos 2\phi \sin^2\Theta \}$$

$$+ \rho_{1-1} \{ \cos 2\Phi \sin^2\Theta + \frac{1}{2} \cos(2\Phi - 2\phi)(1 - \cos\Theta)^2$$

$$+ \frac{1}{2} \cos(2\Phi + 2\phi)(1 + \cos\Theta)^2 \}$$

$$+ \sqrt{2}\, \mathrm{Re}[\rho_{10}] \Big\{ 2\cos\Phi\sin\Theta\cos\Theta$$

$$+ \cos(\Phi - 2\phi)(1 - \cos\Theta)\sin\Theta$$

$$- \cos(\Phi + 2\phi)(1 + \cos\Theta)\sin\Theta \Big\} \Big] .$$

(L = 2 contribution)

Again, we can integrate to get specific angular distributions

$$\frac{dN}{d\cos\Theta} = k_5 \Big\{ |F_1|^2 + \frac{3}{2} |F_1|^2$$

$$\Big[\frac{1}{6} (3\cos^2\Theta - 1) - \frac{1}{2} \rho_{00}(3\cos^2\Theta - 1) \Big] \Big\}$$

$$\frac{dN}{d\Phi} = k_6 \Big\{ |F_1|^2 + |F_1|^2(\rho_{1-1}\sin 2\Phi) \Big\}$$

$$\text{(E-13)}$$

$$\frac{dN}{d\cos\theta} = k_7 \sin^2\theta$$

$$\frac{dN}{d\phi} = k_8 |F_1|^2 \Big\{ 1 + \frac{1}{2} (3\rho_{00} - 1) \cos 2\phi \Big\}.$$

APPENDIX F

ALLOWED EXCHANGES FOR $\pi^- p \rightarrow \pi^+\pi^-\pi^o\pi^o n$

It can be shown from parity (η_{EX}) and G-parity (g_{EX}) considerations at the meson and nucleon vertices [36], that s-channel helicity amplitudes contributing to the production of $(4\pi)^o$ resonances are constrained in the following way:

a) for unnatural parity exchange (UPE) in the t-channel and spin non-flip at the nucleon vertex (++),

$$g_{EX}\eta_{EX} = -1 \quad ; \qquad \text{(F-1)}$$

b) for UPE spin flip (+-),

$$g_{EX}\eta_{EX} = +1 \quad ; \qquad \text{(F-2)}$$

c) for natural parity exchange (NPE) non-flip (++),

$$g_{EX}\eta_{EX} = -1 \quad ; \qquad \text{(F-3)}$$

d) for NPE spin flip (+-),

$$g_{EX}\eta_{EX} = +1 \quad . \qquad \text{(F-4)}$$

It can also be shown [36] that exchanges with

$\eta_{EX}\xi_{EX} = +1$, where $\xi = (-1)^{J_{EX}}$ is the signature, cannot contribute to $\Lambda_{meson} = 0$ for mesons with $\eta_{meson}\xi_{meson} = +1$. Likewise, exchanges with $\eta_{EX}\xi_{EX} = -1$ cannot contribute to $\Lambda_{meson} = 0$ for mesons with $\eta_{meson}\xi_{meson} = -1$ ($\Lambda \equiv$ helicity).

Now since the reaction $\pi^- p \rightarrow \pi^+\pi^-\pi^o\pi^o n$ proceeds via charge exchange (CEX), this implies that $I_{EX} = 1$. Conservation of G-parity at the meson vertex implies that, for $g_{meson} = +1$ (i.e., ρ', B^o,...,etc.), $g_{EX} = -1$ and $C_{EX} = +1$ (since $g = C(-1)^I$).

Therefore, for NPE with $\eta_{EX} = +1$, we are allowed the exchange of states with $g_{EX}\eta_{EX} = (-1)(+1) = -1$ (i.e., δ, A_2). There are no natural parity states with $\eta = -1$ and $I^G = 1^-$ allowed in the quark model and no such states have been observed. For UPE we are allowed exchanges with $g_{EX}\eta_{EX} = (-1)(-1) = +1$ (π, A_3) and $g_{EX}\eta_{EX} = (-1)(+1) = -1$ (A_1).

We shall assume in our discussion that spin zero exchanges such as δ and π contribute very little to $\Lambda_{meson} \neq 0$. A minimal t' dependence can be derived for helicity amplitudes based on conservation of angular momentum [36]. These t' dependencies are summarized in Table 14.

The fact that no $g_{EX}\eta_{EX} = +1$ exchanges are allowed implies that NPE will not contribute to nucleon spin flip amplitudes at low t' (see (F-4)). This means that in NPE spin flip, only $\sqrt{-t}^2$ terms will be allowed for $\Lambda_{meson} = 1$ amplitudes, since these vanish a priori from conservation of momentum and need not obey equation (10-5).

We have combined the above considerations in arriving at the model discussed in Chapter 10. The allowed exchanges are summarized in Table 15.

TABLE 14

t' DEPENDENCIES FROM CONSERVATION OF ANGULAR MOMENTUM

λ_p	λ_n	$f^{\Lambda_{meson}}_{\lambda_p \lambda_n}(t')$
+	+	$\sqrt{-t'}^{\Lambda}\ e^{bt'}$
+	-	$\sqrt{-t'}^{\vert\Lambda-1\vert} e^{bt'}$
-	-	$\sqrt{-t'}^{\Lambda}\ e^{bt'}$
-	+	$\sqrt{-t'}^{\vert\Lambda+1\vert} e^{bt'}$

TABLE 15

ALLOWED EXCHANGES FROM PARITY, G-PARITY AND ANGULAR MOMENTUM CONSERVATION (continued)

AMPLITUDE $M^{\Lambda}_{\lambda_P\lambda_N}$	4π MESON			T-DEPENDENCE FROM ANG. MOM. CONSERVATION	$g_{EX}\eta_{EX}$ G-PARITY CONSERV.	REGGE EXCHANGES									
	$\eta\xi$	J^P	Λ			$\eta\xi$	π: $g\eta = +1$			A_1: $g\eta = -1$			A_3: $g\eta = +1$		
							η	J	T-DEPEN.	η	J	T-DEPEN.	η	J	T-DEPEN.
U^0_{++}	+1	$1^-,2^+$	0	t^0 *	-1	-1	-			+	1	t^0	-	2	
U^1_{++}	+1	$1^-,2^+$	1	t^1	-1	-1	-			+	1	t^1	-	2	t^1 ****
U^0_{++}	-1	$1^+,2^-$	0	t^0	-1	-1	-			+	1	**	-	2	**
U^1_{++}	-1	$1^+,2^-$	1	t^1	-1	-1	-			+	1	t^1	-	2	t^1 ****
U^0_{+-}	+1	$1^-,2^+$	0	t^1	+1	-1	-	0	t^1	+	1	t^1 ****	-	2	t^1
U^1_{+-}	+1	$1^-,2^+$	1	t^0,t^2	+1	-1	-			+	1	t^2 ****	-	2	t^0,t^2
U^0_{+-}	-1	$1^+,2^-$	0	t^1	+1	-1	-	0	**	+	1	**	-	2	**
U^1_{+-}	-1	$1^+,2^-$	1	t^0,t^2	+1	-1	-			+	1	t^2 ****	-	2	t^0,t^2

* A $\sqrt{\ }$ is to be understood over every coefficient.

** Forbidden by parity conservation at meson vertex.

**** Amplitude allowed because it vanishes at t = 0 for angular momentum conservation.

TABLE 15

ALLOWED EXCHANGES FROM PARITY, G-PARITY AND ANGULAR MOMENTUM CONSERVATION

AMPLITUDE Λ $M_{\lambda_P \lambda_N}$	4π MESON			T-DEPENDENCE FROM ANG. MOM. CONSERVATION	$g_{EX}\eta_{EX}$ G-PARITY CONSERV.	$\eta\xi$	REGGE EXCHANGES δ, A_2: $g\eta = -1$		
	$\eta\xi$	J^P	Λ				η	J	T-DEPEN.
N^0_{++}	+1	$1^-,2^+$	0	t^0 *	−1	+1	+1	0,2	**
N^1_{++}	+1	$1^-,2^+$	1	t^1	−1	+1	+1	2	t^1
N^0_{++}	−1	$1^+,2^-$	0	t^0	−1	+1	+1	0,2	t^0
N^1_{++}	−1	$1^+,2^-$	1	t^1	−1	+1	+1	2	t^1
N^0_{+-}	+1	$1^-,2^+$	0	t^1	+1	+1	+1	0,2	**
N^1_{+-}	+1	$1^-,2^+$	1	t^0,t^2	+1	+1	+1	2	t^2 ****
N^0_{+-}	−1	$1^+,2^-$	0	t^1	+1	+1	+1	0,2	t^1 ****
N^1_{+-}	−1	$1^+,2^-$	1	t^0,t^2	+1	+1	+1	2	t^2 ****

* A $\sqrt{\ }$ is to be understood over every coefficient.

** Forbidden by parity conservation at meson vertex.

**** Amplitude allowed because it vanishes at t = 0 for angular momentum conservation.

continued...

REFERENCES

[1] ZGS Experiments No. 420 and 428, Argonne National Laboratory (January, March and June 1977).

[2] M.H. Shaevitz, "A high statistics study of ω^{o} production at 6.0 GeV/c", Ph.D. Thesis, The Ohio State University (1975).

[3] M. Stearns, *Phys. Rev.* 76 (1949) 836.

[4] Particle Data Group, "Review of particle properties", *Rev. of Modern Physics* 48 N.2 (1976) Part II.

[5] S.U. Chung et al., *Phys. Rev.* 11D N.9 (1975) 2426.

[6] V. Chaloupka et al., *Phys. Lett.* 51B N.4 (1974) 407.

[7] M.L. Stevenson et al., *Phys. Rev.* 125 N.2 (1962) 687.

[8] R. Hagedorn, *Relativistic Kinematics*, Benjamin (1964) 112.

[9] CERN/MINUIT, version 5.75 was used for all fitting.

[10] G. Goldhaber et al., *Phys. Rev. Lett.* 15 (1965) 118; S.U. Chung et al., *Phys. Rev.* 165 (1968) 1491.

[11] L. Montanet, *Proceedings of the 1980 International Conference on High Energy Physics*, Madison, Wisconsin (1980) 1209.

[12] ZGS Experiment No. 397, Argonne National Laboratory (October 1975, December 1975 and April 1976).

[13] B. Rossi, *High Energy Particles*, Prentice-Hall (1952) 81-83.

[14] H. Messel and D.F. Crawford, *Electron-Photon Shower Distribution Function Tables for Lead, Copper, and Air Absorber*, Pergamon Press (1970).

continued...

REFERENCES (continued)

[15] C.J. Zanfino, "Experimental investigation of the radiative decay $\eta' \to \omega\gamma$", M.Sc. Thesis, McGill University (1976).

[16] *ZGS User Handbook*, Argonne National Laboratory (1974).

[17] N.R. Stanton, private communication, The Ohio State University.

[18] S. Brandt, *Statistical and Computational Methods in Data Analysis*, North-Holland (1970).

[19] W. Kaplan, *Advanced Calculus*, Addison-Wesley (1952).

[20] A.B. Wicklund, private communication, Argonne National Laboratory.

[21] M. Holder et al., *Nucl. Inst. Methods* 108 (1973) 541.

[22] H. Wind, *Nucl. Inst. Methods* 115 (1974) 431.

[23] S.D. Conte and C. de Boor, *Elementary Numerical Analysis*, McGraw-Hill (1965).

[24] S.U. Chung, *CERN Report* 71-8 (1971).

[25] P.J. Davis and P. Rabinowitz, *Methods of Numerical Integration*, Academic Press (1975).

[26] U. Karshon et al., *Phys. Rev.* D10 (1974) 3608.

[27] R. Gessaroli et al., *Nucl. Phys.* B126 (1977) 382.

[28] M.E. Rose, *Elementary Theory of Angular Momentum*, John Wiley & Sons (1957).

[29] S.U. Chung, *Phys. Rev.* 169 (1968) 1342.

[30] W. Koch, "Some methods of spin analysis in elementary particle physics" in *Analysis of Scattering and Decay* (M. Nikolic, editor), Gorden and Breach (1968).

continued...

REFERENCES (continued)

[31] A. Ralston and H. Wilf, *Mathematical Methods for Digital Computers*, John Wiley & Sons, New York (1960).

[32] J.K. Storrow, *Regge Theory for Experimentalists, Daresbury Lecture Note Series*, No. 6, DNPL/R17.

[33] A.C. Irving and C. Michael, *Nucl. Phys.* B82 (1974) 282.

[34] J.D. Kimel and J.F. Owens, *Nucl. Phys.* B122 (1977) 464.

[35] N.R. Stanton et al., *Phys. Lett.* 92B (1980) 353.

[36] J.A. Dankowych, "A partial wave analysis of the reaction $\pi^- p \rightarrow \pi^+\pi^-\pi^o n$ at 8.45 GeV/c", Ph.D. Thesis, University of Toronto (1980).

[37] F.J. Gilman et al., *Phys. Rev.* D9 N.3 (1974) 715.

[38] H. Haut, *Phys. Rev.* D10 N.9 (1974) 3097.

[39] H. Haut, *Ann. Soc. Sci. Brux.* 87 (1973) 237.

[40] J.A. Dankowych, private communication, McGill University.

[41] A.C. Irving and V. Chaloupka, *Nucl. Phys.* B89 (1975) 345.

[42] V. Sidorov, *Proceedings of the 1979 International Symposium on Lepton and Photon Interactions at High Energies*, Batavia (1979).

[43] F. Richard, *Proceedings of the 1979 International Symposium on Lepton and Photon Interactions at High Energies*, Batavia (1979).

continued...

REFERENCES (continued)

[44] If the quark is taken to be a 6-dimensional representation of SU(6), then the allowed $(q\bar{q})$ meson representations are given by $6 \otimes \bar{6} = \underline{35} \oplus \underline{1}$.

[45] D. Legacy, private communication, Carleton University.

[46] R.T. Deck, *Phys. Rev. Lett.* 13 (1964) 169.